

# **Control of Crystalline Structures and Electrical Properties of Metal Germanide/Ge Contact**

**Yunsheng DENG**

**Ph. D THESIS**

**Control of Crystalline Structures and Electrical Properties  
of Metal Germanide/Ge Contact**

**Yunsheng DENG**

**2014**

**Department of Crystalline Materials Science,  
Graduate School of Engineering, Nagoya University  
Japan**

博士学位論文

金属ジャーマナイド/Ge 接合における  
結晶学的構造および電気的特性の制御

邓 云生

2014年  
名古屋大学大学院  
工学研究科 結晶材料工学専攻

# Contents

1 Introduction.....	1
1.1 Introduction of CMOS technology .....	1
1.2 Challenges of future high performance MOSFETs.....	3
1.2.1 Challenges of scaling gate stack .....	4
1.2.2 Challenges of scaling channel length.....	5
1.2.3 Challenges of scaling source and drain.....	6
1.3 Schottky barrier height.....	8
1.3.1 Formation of Schottky barrier .....	8
1.3.2 Fermi level pinning .....	10
1.3.3 The origin of Fermi level pinning.....	13
1.3.4 The ways to alleviate Fermi level pinning .....	18
1.4 Introduction of contact materials .....	20
1.5 Purpose and contents of this study .....	21
References .....	24
2 Sample fabrication process and characterization method.....	28
2.1 Sample preparation .....	28
2.1.1 Surface cleaning process .....	28
2.1.2 Ni deposition and germanidation .....	28
2.1.3 Fabrication process of Schottky diodes .....	32
2.2 Characterization of the crystalline structure .....	32
2.2.1 X-ray diffraction.....	32
2.2.2 Transmission electron microscopy.....	35
2.2.3 Reflection high energy electron diffraction .....	38
2.2.4 Atomic force microscopy .....	39
2.3 Characterization of the electrical property.....	41
2.3.1 Current-Voltage measurement.....	44
2.3.2 Capacitance-Voltage measurement .....	45
References .....	47
3 Epitaxial formation of Ni Germanide on Ge(110) substrate.....	48
3.1 Background .....	48
3.2 Experiment .....	49
3.3 Results and discussion .....	50
3.3.1 Effect of surface cleaning on crystalline structure of NiGe.....	50
3.3.2 The effect of annealing temperature on the epitaxial and polycrystalline growth of Ni germanide on Ge(110) substrate .....	55
3.3.3 Morphology stability of Ni germanide layers.....	60

3.3.4 Crystalline quality of epitaxial NiGe(100)/Ge(110) .....	63
3.4 Conclusions .....	68
References .....	69
4 Epitaxial formation of Ni germanide on Ge(001) substrate by reactive deposition .....	70
4.1 Background .....	70
4.2 Experiment .....	71
4.3 Results and discussion .....	72
4.3.1 Epitaxial formation of Ni germanide by reactive deposition .....	72
4.3.2 Thickness dependence of epitaxial formation .....	76
4.3.3 Improvement of epitaxial formation by 2-steps deposition .....	78
4.3.4 Discussion about the epitaxial formation mechanism .....	78
4.4 Conclusions .....	80
References .....	82
5 Electrical properties of NiGe/Ge contacts .....	83
5.1 Background .....	83
5.2 Experiment .....	84
5.3 Results and discussion .....	85
5.3.1 Evaluation of the edge leakage current .....	85
5.3.2 Uniformity of SBH distribution in the whole contact area .....	89
5.3.3 The effect of defects in the depletion region on the electrical properties of NiGe/n-type Ge contacts .....	89
5.3.4 The effect of crystalline structure of NiGe layer on the electrical properties of NiGe/n-type Ge contacts .....	97
5.3.5 Capacitance-Voltage characteristics of NiGe/Ge contacts .....	100
5.4 Conclusions .....	107
References .....	108
6 Conclusion and future work .....	109
Acknowledgement .....	112
List of Publications (Oct. 2011 - ) .....	113

# 1 Introduction

## 1.1 Introduction of CMOS technology

The metal-oxide-semiconductor field-effect transistor (MOSFET) is the most important device for ultra-large scale integrated circuit (ULSI) such as microprocessors, memory chips and telecommunications microcircuits [1]. A basic schematic diagram [2] of a MOSFET is shown in Figure 1.1. This device is composed of gate, source and drain regions. The gate is a stack structure of a metal electrode on an insulator layer. The source and drain regions, separated by a channel region of p-type semiconductor, are implanted into n-type semiconductor for the case of n-channel MOSFET. As for the p-channel MOSFET, the type of doping is opposite to that of n-channel MOSFET, namely, the source/drain region and channel region have been doped as p- and n-type semiconductor, respectively. The basic device parameters are the channel length  $L$ , which is the distance between the metallurgical n-p junctions; the channel width  $Z$ ; the insulator thickness  $d$ ; the junction depth  $r_j$ ; and the substrate doping concentration  $N_A$ .

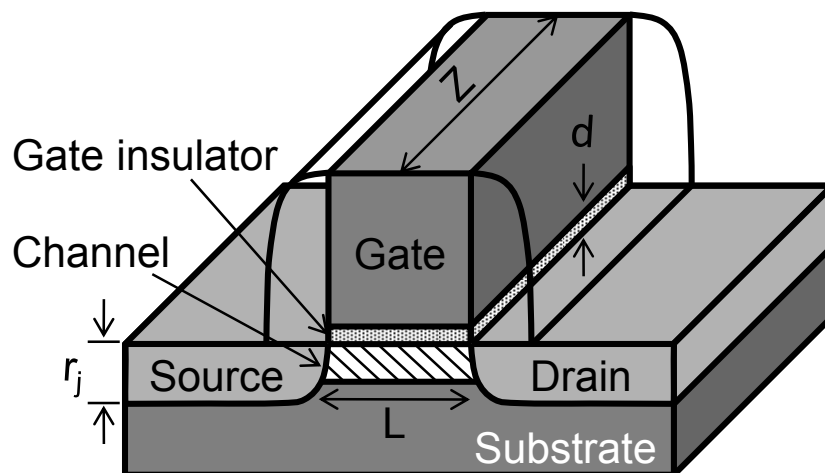


Figure 1.1 Schematic diagram of a MOSFET.

Considering the n-channel MOSFET, there is no current flowing from source to drain except small leakage current when no voltage is applied to the gate, because of the n-p-n junction structure, and the transistor is turned off. In this state, the gate operates as an open switch. When a large enough positive bias is applied to the gate, the p-type channel region is inverted as n-type semiconductor,

which connects the source and drain region. Hence, there is a large current flowing from source to drain, and the transistor is turned on, so the gate behaves as a closed switch in this condition. Note that the critical gate bias driving the channel region start to turn on is called the *threshold voltage*  $V_{TH}$ , which is also an important device parameter for circuit design.

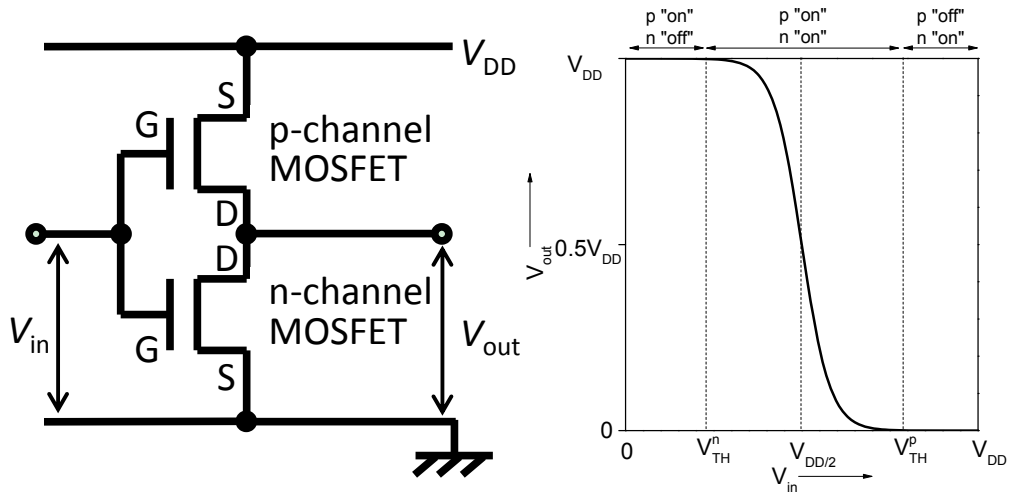


Figure 1.2 (left figure) Schematic diagrams of a CMOS inverter.

Figure 1.3 (right figure) Voltage transfer characteristics of the CMOS inverter.

To demonstrate how MOSFET operates in practical integrated circuit (IC), a complementary metal oxide semiconductor (CMOS) inverter logic circuit [3] is taken for an example, where the typical CMOS is often composed by complementary and symmetrical pairs of p- and n-channel MOSFETs. Figure 1.2 shows the schematic diagram of the CMOS inverter. A p-channel MOSFET is connected with another n-channel MOSFET in series, both gates are connected to the input line  $V_{in}$ , while both of the drains are connected by output line  $V_{out}$ . Figure 1.3 shows the voltage transfer characteristics of the CMOS inverter. When  $V_{in}$  is in high state,  $V_{in} \approx V_{DD}$ , the voltage between gate and substrate of the p-channel MOSFET is nearly zero, and the transistor is turned off. As for the n-channel MOSFET, the gate-substrate voltage is  $V_{DD}$ , so the transistor is turned on. That means, the output terminal is connected to ground, thus,  $V_{out}$  is zero. Analogically, when  $V_{in}$  is in low state, the output terminal is in a high state,  $V_{out} \approx V_{DD}$ , since the p-channel MOSFET is turned on while n-channel MOSFET is turned off.

## 1.2 Challenges of future high performance MOSFETs

As the information and communication technology rapidly develops, the personal computer (PC)-centric system integration has shifted to the multifunctional integration in a limited space [4], e.g., the computational and global position system functions have been combined into cell phone. This multifunction integration in a limited space drives the IC designer to consider the performance, cost of microelectronic products, and power consumption, which are associated with the switching speed, integration density, and supply voltage, respectively. The conventional and effective way to achieve high speed, low power consumption, and high integration, is shrinking the size of MOSFET by reducing the gate dielectric thickness, reducing the gate length, and increasing the channel doping concentration. Dennard *et al.* [5] summarize the benefits from scaling, it is demonstrated that scaling the device by a factor  $\kappa$  increases the switching speed by  $\kappa$ , increases the density of device by  $\kappa^2$ , reduces the power dissipation by  $\kappa^2$  and improves the power-delay product by  $\kappa^3$ , which implies a reduction in supply voltage by  $\kappa$ , as well as a reduction in the threshold voltage by the same factor  $\kappa$  [1].

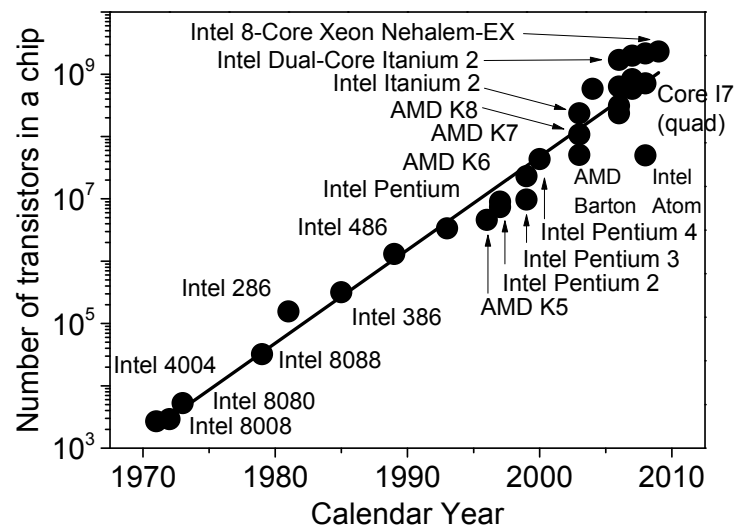


Figure 1.4 The evolution of the density of transistor in microprocessors [7].

Thanks to these conventional ways, the scaling of MOSFET has been achieved to sub-nanometer technology, and successfully sustains Moore's law [6]

in the past 48 years, which predicts the density of transistor on an integrated circuit doubles in every 18 – 24 months, as shown in Figure 1.4 [7]. However, as the scaling proceeds deeper and deeper, e.g., the gate length approaches to approximately 10 nm in 2020 predicted by international technology roadmap for semiconductors (ITRS) [8], the Dennard's law becomes invalid, and the conventional scaling ways is no longer effective to improve the performance of device, to increase the density of integration, and to reduce the power consumption, because scaling technology faces numerous significant challenges, such as the gate leakage current, short-channel effect, and high parasitic resistance, etc.

### 1.2.1 Challenges of scaling gate stack

Generally, the saturation drain current  $I_{Dsat}$  of MOSFET is approximately expressed by the Equation (1.1) [9, 10]

$$I_{Dsat} \propto \frac{Z}{L} \frac{\epsilon}{d} \mu (V_g - V_{TH})^2 \quad (1.1)$$

where the  $\epsilon$  is the permittivity of the insulator,  $\mu$  is the carrier mobility,  $V_g$  is the gate voltage,  $V_{TH}$  is the threshold voltage, and the other parameters are shown in Figure 1.1. By inspection of this equation, one of the effective ways to obtain a large drain current is by using an insulator material with a high permittivity, or reducing the equivalent gate oxide thickness (EOT).

The reduction of EOT has been accomplished by introduction of the high permittivity (high- $\kappa$ ) dielectric material, and the high- $\kappa$  dielectric insulator, like HfSiO<sub>x</sub>, HfSiON<sub>x</sub>, has been used in semiconductor industry since 2008 [11]. However, further reduction of the EOT still needs further investigation or study. One challenge is about controlling the crystalline structure and orientation of ultra-thin high- $\kappa$  insulator to increase its permittivity. Another issue is the gate tunneling current, a by-product of scaling the gate stack. The tunneling current density  $J_T$  is described by the equation (1.2),

$$J_T \propto \exp(-\alpha \sqrt{m^* \cdot \Delta E} \cdot d) \quad (1.2)$$

where  $\alpha$  is the polarizability of crystal of high- $\kappa$  materials in per unit volume,  $m^*$  is the effective mass of carrier in high- $\kappa$  material, and  $\Delta E$  is the energy band offset of the conduction or valence band between the insulator layer and the substrate ( $\Delta E_c$  or  $\Delta E_v$ ), respectively. This equation presents some rules for the selection of

proper high- $\kappa$  material with small leakage current: First one is to find a high- $\kappa$  material with small band offsets of  $\Delta E_c$  and  $\Delta E_v$  between the high- $\kappa$  material insulator and substrate. Second one is to adopt the high- $\kappa$  material with small effective masses of carrier.

### 1.2.2 Challenges of scaling channel length

For a given channel doping concentration, as the channel length is reduced to certain magnitude, the depletion regions of source and drain junctions located at both sides of the gate could not be ignored like we treat the case of long-channel MOSFET, since the widths of depletion regions of source and drain junctions become comparable to channel length. As a result, the potential in the channel region is not controlled solely by gate voltage any more, but also additionally influenced by the drain voltage. To some extent, the gate loss the switch-like function. This departure from the case of long-channel MOSFET induced by short-channel is called *short-channel effect* [10, 12].

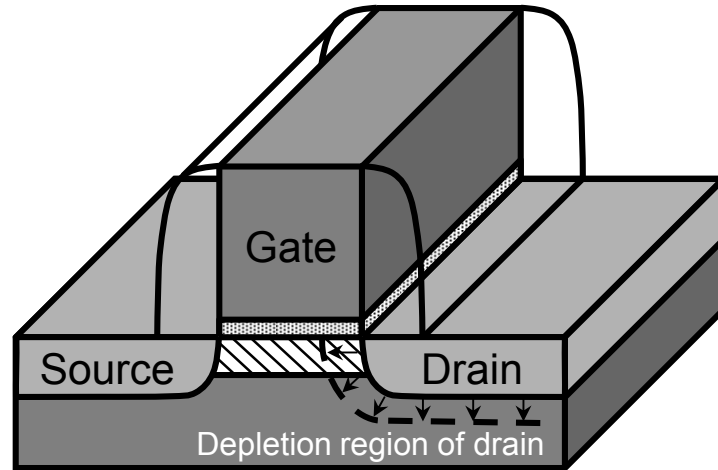


Figure 1.5 Schematic diagram of DIBL.

As mentioned previously, it is expected that the gate length will approach to approximately 10 nm in 2020. In other words, the distance between source and drain will be of the order of several nanometers, equivalent to the length of tens of series unit cells of silicon. In this case, the issue of short-channel effect will become even more prominent, and this effect is embodied by the drain-induced barrier lowering (DIBL), a degradation of subthreshold slope, and increasing of

leakage current. The schematic diagram of DIBL is shown in Figure 1.5, when the drain voltage increases, the depletion region of drain or source (not shown in the schematic diagram) extends laterally in carrier transport direction, namely, the effective channel length becomes shorter compared with the physical channel length, which gives rise on the decrease of the threshold voltage. In the term of leakage current, when the electrical field is increased to certain value, the carrier multiplication near the drain will occur, thus, a leakage current will flow through the substrate.

### 1.2.3 Challenges of scaling source and drain

Source and drain, often connecting to other devices through a metal wire, play a great role of transmitting the signal, e.g., the output voltage  $V_{DD}$  in Figure 1.2. To guarantee the success of signal transmission, the parasitic resistance of MOSFET is required to be small, because the output signal would be degraded, or distorted in extreme case if the parasitic resistance is over the tolerable limit.

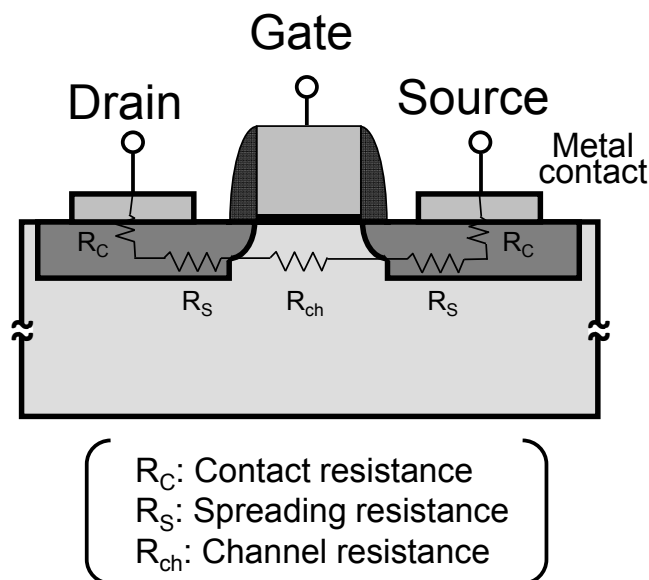


Figure 1.6 Equivalent circuit of parasitic resistance in CMOS.

The detail equivalent circuit is illustrated in Figure 1.6. The main components of parasitic resistance  $R_{SD}$  include contact resistance  $R_C$  at the metal/heavily doped source or drain interface and spreading resistance  $R_S$ . Another resistance is channel resistance  $R_{ch}$ . With the scaling of technology node,

the channel resistance  $R_{ch}$  decreases due to the continuous scaling of channel length. Whereas, the parasitic resistance  $R_{SD}$  (except the channel resistance  $R_{ch}$ ) increases accompanied with shrink of contact area. Since the technology approaches to 32 nm, the major contributor to the total resistance of CMOS has been changed from  $R_{ch}$  to  $R_{SD}$ , as shown in Figure 1.7. Among the parasitic resistances, one of the main components is contact resistance  $R_C$ . Therefore, in order to guarantee the total  $R_{SD}$  within a tolerable limit, it is imperative to reduce  $R_C$ . Taking the 16-nm technology node for example, the maximum value of  $R_C$  is required to be approximately  $2.2 \times 10^{-8} \Omega \cdot \text{cm}^2$  [13].

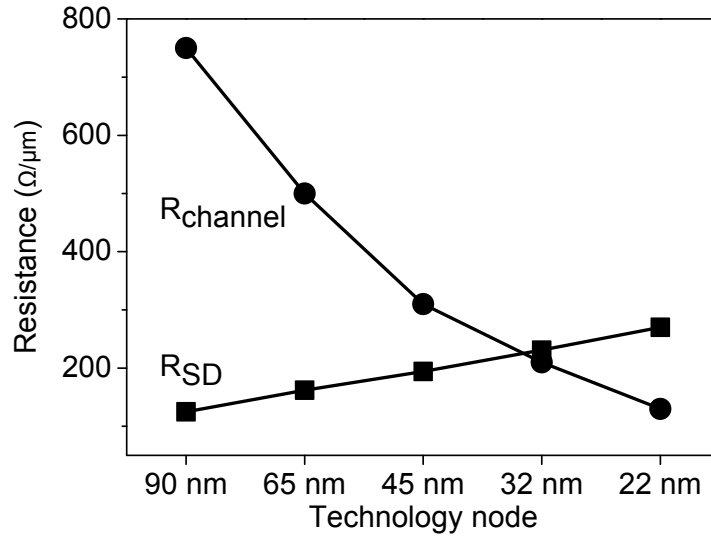


Figure 1.7 The evolution of channel resistance and parasitic external resistance with the scaling of device dimension [14].

The specific contact resistance is generally given by the derivative of current density with respect to voltage:

$$R_C = \left( \frac{\partial J}{\partial V} \right)_{V=0}^{-1} \quad (1.3)$$

where  $J$  is the current density,  $V$  is the applied voltage. Considering the metal/semiconductor contacts with moderately doping concentrations, the thermionic emission current dominates in this case. Therefore, the contact resistance could be described by equation (1.4)

$$R_C = \frac{k}{qA^*T} \exp\left(\frac{q\Phi_{Bn}}{kT}\right) \quad (1.4)$$

where  $k$  is the Boltzmann constant,  $q$  is the elementary charge,  $A^*$  is the effective

Richardson constant,  $T$  is the temperature, and  $\Phi_{\text{Bn}}$  is the Schottky barrier height (SBH). This equation reveals that the contact resistance  $R_C$  is an exponential function of SBH  $\Phi_{\text{Bn}}$ . Thus, one of the ways to reduce the contact resistance  $R_C$  is to reduce the SBH  $\Phi_{\text{Bn}}$ , which will be discussed in the next section in detail.

Considering the metal-semiconductor with heavily doped source/drain, the tunneling current, instead of thermionic emission current, will dominate the current flow, and the contact resistance  $R_C$  has the form:

$$R_C \sim \exp\left(\frac{q\Phi_{\text{Bn}}}{E_{00}}\right) = \exp\left[\frac{2\sqrt{\epsilon_s m^*}}{\hbar} \left(\frac{\Phi_{\text{Bn}}}{\sqrt{N_D}}\right)\right] \quad (1.5)$$

where  $E_{00} \equiv \frac{q\hbar}{2} \sqrt{\frac{N_D}{\epsilon_s m^*}}$ ,  $\epsilon_s$  is the permittivity of the semiconductor,  $m^*$  is the effective mass of semiconductor,  $\hbar$  is Planck's constant, and the  $N_D$  is doping concentration. This equation indicates that the contact resistance  $R_C$  quite depends on the doping concentration  $N_D$ , besides the SBH  $\Phi_{\text{Bn}}$ . Therefore, another way to control the contact resistance  $R_C$  within a tolerable limit is heavy doping of Source/Drain. However, this method faces some challenges, like the difficulty in forming very shallow and heavily doped source/drain junction.

### 1.3 Schottky barrier height

As mentioned in the last section, SBH is one of the key factors determining the contact resistance. In physics, a Schottky barrier is a potential energy barrier at a metal/semiconductor interface, only those carriers with the energy above this potential energy barrier could transport across this interface, hence contribute to the current flow. In this section, we discuss about the formation of SBH in ideal condition by considering the energy band diagram alignment of metal and semiconductor. And the deviation from this ideal Schottky model in practical experiment, named as *Fermi level pinning* (FLP), is also introduced. Finally, various methods proposed for alleviating FLP are reviewed.

#### 1.3.1 Formation of Schottky barrier

Figure 1.8 (a) shows the energy band diagram of a metal and an n-type semiconductor when they are isolated from each other. The metal is defined by its work function  $\Phi_M$ . Semiconductor is specified by its electron affinity  $\chi_s$ , work

function  $\Phi_S$ , and energy band gap  $E_g = E_c - E_v$ . All of these parameters are referenced to a same vacuum level  $E_{VAC}$ .

When metal and semiconductor are brought intimately, or connected by a wire, electron will diffuse from semiconductor to metal due to the higher Fermi level ( $E_{FS}$ ) of semiconductor than that ( $E_{FM}$ ) of metal, as denoted by the solid left-going arrow in Figure 1.8(a). Meanwhile, the positive charges will become obvious in the semiconductor side due to the leaving away of electrons from the ionized donor. In turn, those ionized donor will creates a negative field, which will lower the Fermi level of semiconductor at the depletion region and drift the electrons back to semiconductor. In the beginning, there is a net transport of electron from semiconductor to metal because the diffusion amount is larger than the drift amount. Gradually, the diffusion amount will decrease and drift amount will increase due to the lowering of Fermi level of semiconductor and increase of the negative field, respectively. Finally, the diffusion amount will equal to drift amount, and the net transport of electron from semiconductor to metal becomes zero, namely, the thermal equilibrium is established.

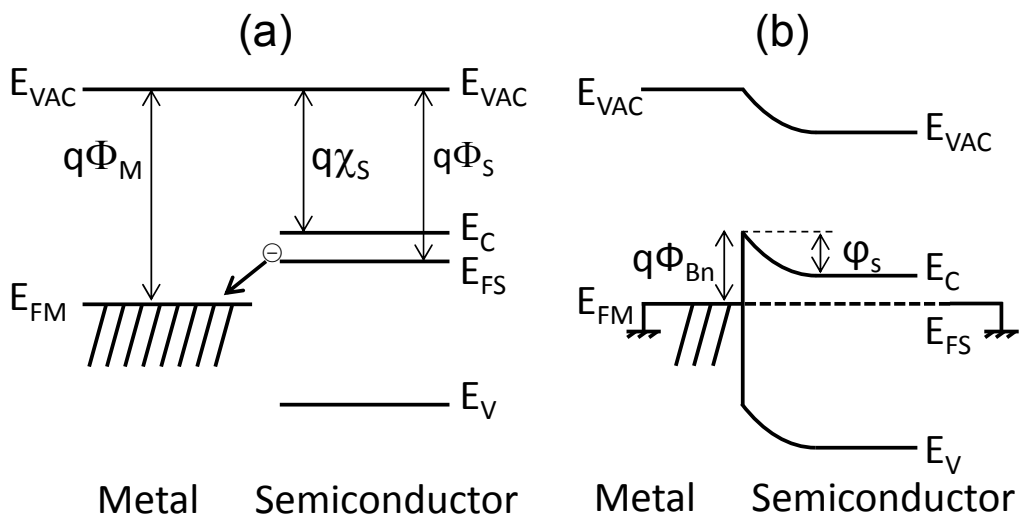


Figure 1.8 Energy band diagram of a metal and an n-type semiconductor: (a) metal and semiconductor is isolated; (b) metal is made intimate contact with semiconductor.

In this equilibrium state, the Fermi level of semiconductor and metal aligns up, which implies that the Fermi level of semiconductor is lowered by an amount

equal to the difference between the Fermi level of semiconductor and metal. The corresponding band diagram is shown in Figure 1.8 (b). Based on this band diagram, the built-in potential  $\phi_s$  of semiconductor and the SBH  $\Phi_{Bn}$  at the interface of metal/semiconductor could be derived,

$$q\phi_s = q(\Phi_M - \phi_s) \quad (1.6)$$

$$q\Phi_{Bn} = q(\Phi_M - \chi_s) \quad (1.7)$$

The SBH is simply determined by the difference between the work function of metal and electron affinity of semiconductor, which was proposed and devised by Schottky and Mott [15, 16]. This Schottky-Mott theory implies that it is possible to obtain a low resistivity contact by choosing an appropriate metal with a comparably low work function to the electron affinity of semiconductor. For the ideal metal/p-type semiconductor, the SBH  $\Phi_{Bp}$  could be derived similarly with the metal/n-type semiconductor case,

$$q\Phi_{Bp} = E_g - q(\Phi_M - \chi_s) \quad (1.8)$$

Combining equation (1.7) and (1.8), it is easy to find that the sum of  $\Phi_{Bn}$  and  $\Phi_{Bp}$  is equal to the band gap of semiconductor for any metals on a given semiconductor, as given by Equation (1.9).

$$q(\Phi_{Bp} + \Phi_{Bn}) = E_g \quad (1.9)$$

### 1.3.2 Fermi level pinning

As discussed in the last section for ideal Schottky-Mott theory, the SBH has a linear relationship with the work function of metal. However, in practical experiment, the SBH exhibits a weaker dependence on the work function of metal than that is described in Schottky-Mott theory. Figure 1.9 is the summary of the SBHs of various metal/n-type Ge contacts as a function of the work function of those metals [17-31], those SBHs deviate from the Schottky-Mott theory, as indicated by the deviation of fitted solid line from the dash line (Schottky-Mott limit, Equation (1.6)), although by and large metals with larger work functions show systematically higher SBH than those with lower work functions. This phenomenon is often described by FLP: the Fermi level at the interface of metal and semiconductor is actually pinned at the charge neutrality level (CNL), which is close to the valence band of semiconductor. Thus, the SBH is determined by the energy level of CNL, and becomes little dependent on the work function of metal.

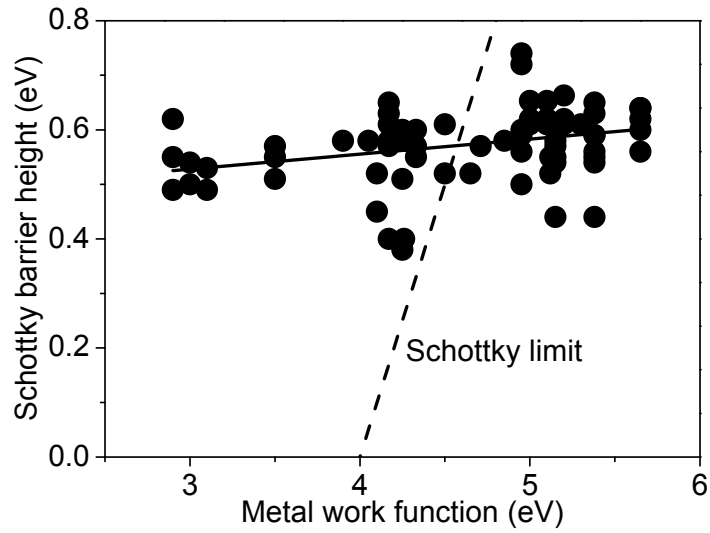


Figure 1.9 Summary of SBHs of various metal/n-type Ge contacts as a function of the metal work functions [17-31].

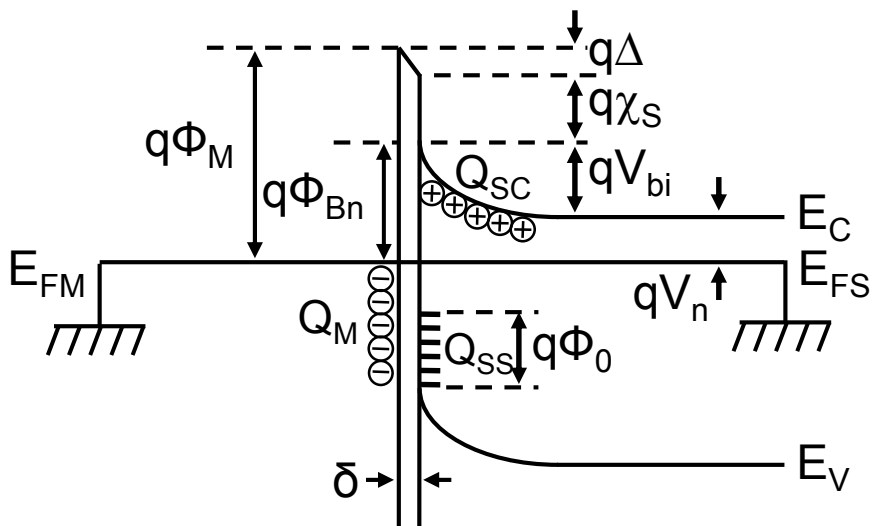


Figure 1.10 Energy band diagram of a metal/n-type semiconductor contact considering the interface states with the energy level in the forbidden band gap of the semiconductor.

Next, we demonstrate the weak dependence of SBH on the work function by the FLP in detail [32, 33]. Figure 1.10 shows the energy band diagram of a metal/semiconductor contact considering the interface states with the energy level at the forbidden bandgap of the semiconductor (the detail of those interface states will be discussed later). Those interface states are assumed to be acceptor surface states, have a constant density of states  $D_s$ , and the CNL is at  $q\Phi_0$  referenced to the valence band  $E_v$ . The net charge  $Q_{ss}$  in the continuum of interface states is given by

$$Q_{ss} = -qD_s(E_g - q\Phi_0 - q\Phi_{Bn}) \quad (1.10)$$

The space charge  $Q_{sc}$  that forms in the depletion layer of the semiconductor is given by

$$Q_{sc} = \sqrt{2q\epsilon_s N_D V_{bi}} \quad (1.11)$$

where  $V_{bi}$  is the energy band bending of semiconductor. The charge neutrality in the system of metal/semiconductor contact requires that the charge  $Q_M$  in the metal side is balanced by sum of  $Q_{ss} + Q_{sc}$  in the interface states and a space charge layer in the semiconductor side, thus  $Q_M$  can be written as

$$Q_M = -(Q_{ss} + Q_{sc}) \quad (1.12)$$

The net charge in the interface states can be treated as an electric double layer, this double layer has a thickness of a few angstroms and will therefore be transparent to electrons. It has to note that the width of the double layer and that of depletion layer in the semiconductor side are not drawn to scale in Figure 1.10. The potential  $\Delta$  across the double layer can be obtained by the application of Gauss's law to the charge residing on the metal side,

$$\Delta = -\delta \frac{Q_M}{\epsilon_i} \quad (1.13)$$

where  $\epsilon_i$  is the permittivity of the double layer, and  $\delta$  is its width. On the other hand, the Fermi level is constant through the system of metal/semiconductor in thermal equilibrium state, thus, inspecting the energy band diagram of Figure 1.10, the potential  $\Delta$  could be obtained in other form

$$\Delta = \Phi_M - (\chi_s + \Phi_{Bn}) \quad (1.14)$$

Combining Equation (1.10) - (1.14), we obtain

$$(\Phi_M - \chi_s) - \Phi_{Bn} = \sqrt{\frac{2q\epsilon_s N_D \delta^2}{\epsilon_i^2}} (\Phi_{Bn} - \Phi_s + \chi_s) - \frac{qD_s \delta}{\epsilon_i} (E_g - q\Phi_0 - q\Phi_{Bn}) \quad (1.15)$$

To simplify the solution of Equation (1.15), we define

$$c_1 \equiv \frac{2q\epsilon_s N_D \delta^2}{\epsilon_i^2} \quad (1.16a)$$

$$c_2 \equiv \frac{\epsilon_i}{\epsilon_i + q^2 \delta D_s} \quad (1.16b)$$

The solution of Equation (1.15) could be written as

$$\begin{aligned} \phi_{Bn} = & \left[ c_2(\phi_M - \chi_s) + (1 - c_2) \left( \frac{E_g}{q} - \phi_0 \right) \right] \\ & + \left\{ \frac{c_2^2 c_1}{2} - c_2^{\frac{3}{2}} \left[ c_1(\phi_M - \chi_s) + (1 - c_2) \left( \frac{E_g}{q} - \phi_0 \right) \frac{c_1}{c_2} - \frac{c_1}{c_2} (\phi_s - \chi_s) + \frac{c_1^2 c_2}{4} \right]^{\frac{1}{2}} \right\} \end{aligned} \quad (1.17)$$

Since the  $\{\}$  term in Equation (1.17) is as small as 0.04 V, we could neglect the  $\{\}$  term, and the solution (1.17) is simplified as

$$\phi_{Bn} = c_2(\phi_M - \chi_s) + (1 - c_2) \left( \frac{E_g}{q} - \phi_0 \right) \quad (1.18)$$

Considering two limiting condition, the physical mean of Equation (1.18) is easily understood:

- (a) When  $D_s \rightarrow \infty$ , from Equation (1.16b), we have  $c_2 \rightarrow 0$ , then Equation (1.18) is transformed as

$$q\phi_{Bn} = E_g - q\phi_0 \quad (1.19a)$$

In this condition, the SBH is entirely determined by the CNL of interface states at the surface of semiconductor, and independent on the work function of metal. In other words, the Fermi level at the interface is completely pinned at the CNL with the energy level  $q\phi_0$  above the valence band  $E_v$  of semiconductor.

- (b) When  $D_s \rightarrow 0$ , from Equation (1.16b), we have  $c_2 \rightarrow 1$ , then Equation (1.18) is transformed as

$$\phi_{Bn} = \phi_M - \chi_s \quad (1.19b)$$

In this case, Equation (1.18) is transformed back to the ideal Schottky-Mott law, namely, the SBH is determined by the work function of metal, and the FLP does not occur in this limit condition.

### 1.3.3 The origin of Fermi level pinning

Although the origin of FLP has been investigated for many decades, it has not yet been understood in detail, and still remains a debate. Many researchers attributed this FLP to the defects existing at the interface of metal/semiconductor

[34, 35], however, the detail about the defects, including the type of defects (e.g., point defect, dislocation), the amount of the defects, needs to be further investigated. There is also another viewpoint that the polarized chemical bonds at the metal/semiconductor interface, as well as the inhomogeneity of polycrystalline contacts have the responsibility of FLP [36]. Note that those factors causing FLP, as mentioned above, is extrinsic, which implies that the FLP is adjustable by controlling the type and amount of defects.

Heine [37] pointed out that, due to the overlap of the conduction band of metal with the forbidden gap of semiconductor range from the top of the valence band to the Fermi level, the metal wavefunctions will decay into the forbidden gap of the semiconductor, thus, so called metal induced gap states (MIGS) are introduced within the forbidden gap of semiconductor near the interface of metal/semiconductor. In turn, those MIGS will pin the Fermi level of semiconductor to the energy level of MIGS, which results into the independence of SBH on the work function of metal. We also have to note that this viewpoint implies that these MIGS are intrinsic property of the semiconductor, which is hardly controllable.

To understand MIGS in detail, such as the density of states and the energy level, we consider a nearly free electron in a linear, one dimensional lattice [38]. The periodic potential is assumed to have the form

$$V(z) = V_0 + 2V_1 \cos(g_1 z) \quad (1.20)$$

where  $g_1 = 2\pi/a$  is the shortest vector of the reciprocal lattice,  $a$  is the lattice parameter, and  $V_1$  is Fourier coefficient of the potential. And the wavefunctions may be approximated by the first two terms of Fourier expansion,

$$\psi_k(z) = A \exp(ikz) + B \exp[i(k - g_1)z] \quad (1.21)$$

Substituting Equation (1.20) and (1.21) into Schrodinger's equation, we obtain the secular equation

$$\begin{bmatrix} (\hbar^2/2m_0)k^2 - V_0 - W & V_1 \\ V_1 & (\hbar^2/2m_0)(k - g_1)^2 - V_0 - W \end{bmatrix} \begin{bmatrix} A \\ B \end{bmatrix} = 0 \quad (1.22)$$

Solving Equation (1.22) by considering the edge of the Brillouin zone,  $k = \pi/a - \kappa$ , we obtain the energy dispersion,

$$W(\kappa) - V_0 = W_1 + \left(\frac{\hbar^2}{2m_0}\right) \kappa^2 \pm \left[ V_1^2 + 4W_1 \left(\frac{\hbar^2}{2m_0}\right) \kappa^2 \right]^{\frac{1}{2}} \quad (1.23a)$$

where  $W_1 = (\hbar^2/2m_0)(g_1/2)^2$ , thus the well-known energy band structure could

be drawn based on Equation (1.23), as shown in Figure 1.11. Two allowed bands are separated by an energy gap  $E_g$  whose magnitude is  $2|V_1|$ .

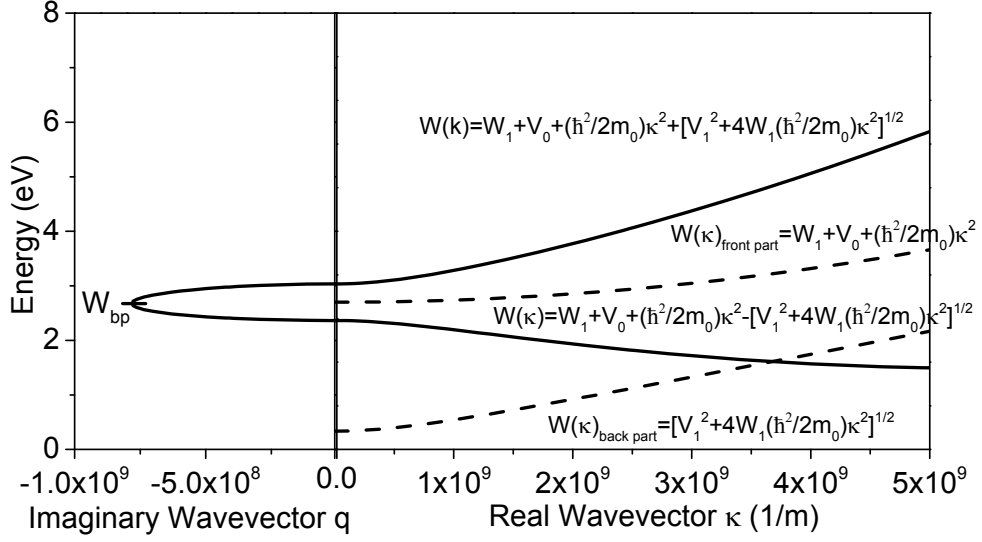


Figure 1.11 A typical energy band structure calculated by using the real wavevector  $k = \pi/a - \kappa$  and complex wavevector  $k = \pi/a + iq$  for the bulk and surface cases, respectively.

Since the energy  $W(\kappa)$  is a function of  $\kappa^2$ , both real wavevector and complex wavevector are permitted. However, only real wavevector is reasonable for bulk case because complex wavevector would result in the unnormalized Bloch waves (see Equation (1.21)). Whereas, a complex wavevector is suitable for surface case, imagining that a periodic wavefunction exponentially decays from the surface to semiconductor and has an exponential tail into vacuum, such wavefunctions could be normalized, thus could represent electrons bound to the surface. Therefore, electronic surface states at the end of a finite one-dimensional solid will have complex wavevectors.

By using the complex wavevector,  $k = \pi/a - q$ , the solution of Equation (1.22) is given by

$$W(q) - V_0 = W_1 - \left(\frac{\hbar^2}{2m_0}\right)q^2 \pm \left[V_1^2 - 4W_1\left(\frac{\hbar^2}{2m_0}\right)q^2\right]^{\frac{1}{2}} \quad (1.23b)$$

The energy  $W(q)$  as a function of imaginary part  $q$  is shown in Figure 1.11. This complex band structure has an energy loop across the energy gap of the two bulk bands at the edge of the Brillouin zone. Here, we have to note that when the imaginary  $q$  meets the condition  $\left(\frac{\hbar^2}{2m_0}\right)q_{max}^2 = V_1^2/4W_1$ , the contributions from

both bands are equal in magnitude, the energy level  $W_{bp}$  of this point, which is called *branch point* [39], as marked in Figure 1.11, is an important parameter to evaluate the energy level where the Fermi level is pinned in the forbidden gap of semiconductor. Another important parameter is the imaginary part  $q$ , since the inverse of  $q$  is the decay length of the respective wavefunction penetrating into the linear chain, or semiconductor.

Substituting the complex wavevector  $k = \pi/a - q$  into the secular equation (1.22), the ratio A/B is equal to  $\exp(i2\varphi)$ , where the phase factor  $\varphi$  is determined by the imaginary part  $q$

$$\sin^2 \varphi = -\frac{4W_1q}{V_1g_1} \quad (1.24)$$

Finally, we could write the wavefunction by the parameters,  $\varphi$ ,  $q$ ,  $A$ , and  $B$

$$\begin{aligned} \psi_q(z) &= \exp(-qz) \left[ A \exp\left(\frac{i\pi z}{a}\right) + B \exp\left(-\frac{i\pi z}{a}\right) \right] \\ &= A' \exp(-qz) \cos\left(\frac{\pi z}{a} + \varphi\right) \end{aligned} \quad (1.25)$$

Where  $A'$  is a constant.

Next, based on these solutions of Schrodinger's equation, the density of states is expressed [40],

$$D_{vs}(W)dW = (2\pi)^{-1} \frac{d\varphi}{dW} dW \quad (1.26a)$$

Since at the branch point  $\left(\frac{\hbar^2}{2m_0}\right)q^2$  has the maximum value  $V_1^2/4W_1$ , so the density of states is approximated by

$$D_{vs}(W)dW \cong (2\pi)^{-1} [V_1^2 - (W - V_0 - W_1)^2]^{1/2} dW \quad (1.26b)$$

By inspection of Equation (1.26b), the density of states varies  $\cap$ -shaped across the band gap of semiconductor.

This viewpoint is consistent with the theoretical calculation of the local density of states (LDOS) near the interface of Al/Si junction using a jellium density corresponding to Al and self-consistent Si pseudopotentials by Louie and Cohen [41]. As shown in Figure 1.12, each of the regions has a width of 0.314 nm, which is the distance between adjacent Si double layers in the [111] direction. Regions I - III correspond to the bulk-like LDOS of metal, while regions V and VI correspond to the bulk-like LDOS of Si. The most interesting is that an additional state  $S_k$  is found near the interface of Al/Si on the Si side by comparison of the calculated LDOS with the bulk-like LDOS of Si (indicated by the dash line), as

shown in region IV. Furthermore, those additional states exhibit a  $\cap$ -shaped energy distribution and exponentially decay into the Si. These features resemble the characteristics of MIGS.

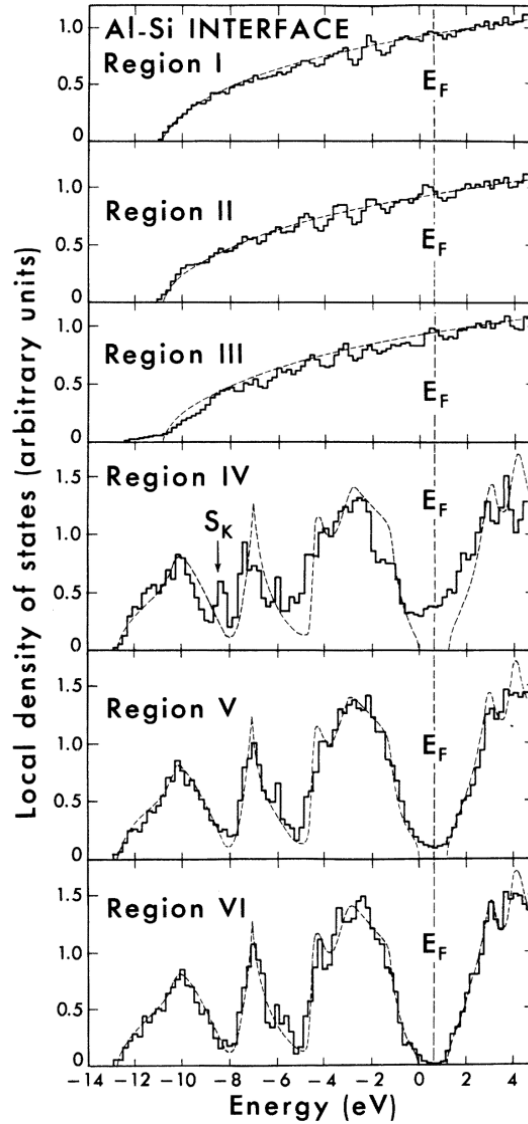


Figure 1.12 Local density of states at the interface of Al/Si junction calculated by a jellium-semiconductor model [41].

Next, we compare the degree of FLP for various materials by summarizing the branch point energy, tailing length, and densities of states of MIGS of each material, as shown in Table 1.1. Among those materials, the Fermi level of Ge is pinned much closer to the valence band by comparison of the relative branch point with that of other materials. On the other hand, the tailing length of wavefunction nearly has no difference for various materials.

Table 1.1 Branch point energies, tailing lengths, and densities of states of MIGS.

Semiconductor	Branch point energy [eV] $W_{bp} - E_v$	Tailing length [nm] $1/2q$	Densities of state [cm <sup>-2</sup> eV <sup>-1</sup> ] $D_s \times 10^{14}$
Si	0.36 [42]	0.3 [42, 43]	4.5 [44]
Ge	0.17 [45]	0.4 [42]	-
GaAs	0.5 [46]	0.3 [42]	5.0 [44]
	0.55 [47]	0.28 [44]	-

### 1.3.4 The ways to alleviate Fermi level pinning

So far, various methods have been proposed to alleviate, or completely remove FLP for the practical application of n-channel Ge MOSFET. One of the main methods is by inserting an ultra-thin (approximately, 0.7-2 nm-thick) insulator layer between the metal and semiconductor, which could be explained by MIGS model. The insulator layers, such as GeO<sub>x</sub> [48], Al<sub>2</sub>O<sub>3</sub> [49], Ge<sub>3</sub>N<sub>4</sub> [50], and SiN [51], play a role of shield to prevent the penetration of electron wavefunction of metal into semiconductor, thus the FLP effect becomes weak, and an Ohmic contact could be obtained on n-type semiconductor by choosing metals with low work function, while the rectifying characteristics still remains for the metal with high work function. For example, Cr/Ge<sub>3</sub>N<sub>4</sub>/n-type Ge contact exhibits an Ohmic characteristics, additionally, the rectifying characteristics is observed for Cr/Ge<sub>3</sub>N<sub>4</sub>/p-type Ge, which further proves that the FLP is alleviated by insertion of the interfacial layer.

However, an undesired dipole, at the Ge<sub>3</sub>N<sub>4</sub>/Ge interface, or at the metal/Ge<sub>3</sub>N<sub>4</sub> interface, may be induced by the insertion of Ge<sub>3</sub>N<sub>4</sub> insulator, since the SBH of Cr/Ge<sub>3</sub>N<sub>4</sub>/n-type Ge is a little higher than the value expected by the difference between the work function of Cr and the electron affinity of Ge substrate. On the other hand, the insertion of insulator would extra increase the sheet resistance, which might prohibit the application of this method into the contact technology. Take Al/SiN/Ge contact as an example, the lowest contact resistance obtained in an optimized condition is approximately 0.01 Ω·cm<sup>2</sup>, this value is more than six orders of magnitude higher than the requirement of the 16

nm technology, as mentioned in the section 1.2.3.

The second method to obtain low contact resistivity is by heavily doping [20, 52-55]. Generally, a thin layer with high impurity in semiconductor is prepared to form a very thin depletion region, this thin depletion region could give rise to a large tunneling current, thus the contact resistance could be reduced. However, this method just bypasses the FLP effect, the SBH is still high, so the reduction of the contact resistance by heavily doping is limited. In addition, the heavily doping also faces some challenges, such as the difficulty of the fabrication of the shallow doping layer due to the low solubility and high diffusion coefficient of dopant in Ge, especially the n-type one.

Table 1.2 Reduction of SBH by controlling crystalline structures of metal layer.

Metal/Ge	Crystalline structure	SBH (eV)
Mn/Ge(111) [56]	Epi. Mn <sub>5</sub> Ge <sub>3</sub> (001)//Ge(111)	0.43
Mn/Ge(001) [56]	Poly. Mn <sub>5</sub> Ge <sub>3</sub>	0.56
Fe/Ge(111) [57]	Epi. Fe <sub>3</sub> Si(111)//Ge(111)	0.46
Fe/Ge(001) [57]	Poly. Fe <sub>3</sub> Si	0.56

Recently, some works [56, 57] show that epitaxial metal/semiconductor contact has lower SBH compared with that of polycrystalline metal/semiconductor, the detail is summarized in Table 1.2. In the case of Mn/Ge system, the SBH of polycrystalline Mn<sub>5</sub>Ge<sub>3</sub>/n-type Ge(111) contact is estimated to be 0.56 eV by current density-voltage characteristics, while the epitaxial Mn<sub>5</sub>Ge<sub>3</sub>(001)/n-type Ge(111) contact has a SBH, approximately 0.13 eV lower than that of polycrystalline Mn<sub>5</sub>Ge<sub>3</sub>/n-type Ge(111) contact. Similar to Mn<sub>5</sub>Ge<sub>3</sub>/n-type Ge system, Fe<sub>3</sub>Si/n-type Ge(111) system also shows the reduction of SBH by controlling the crystalline structures of the metal layer. Basically, this reduction of SBH is considered as the Fermi level depinning due to the reduction of the defects at the interface between metal and semiconductor by epitaxial formation. Generally, there are fewer defects at the interface of epitaxial metal/semiconductor, compared with that of polycrystalline metal/semiconductor, because epitaxial metal/semiconductor has a good atomic matching at its interface, whereas, at the interface of polycrystalline meta/semiconductor, the

atomic arrangement is disorder due to the grain boundary and random orientation of each grain, thus at this disordered interface are many defects, such as point defect, dislocation, which would play a role of interface states to pin the Fermi level of semiconductor.

## 1.4 Introduction of contact materials

Before discussing about the contact materials, a brief introduction of the semiconductor material will be given firstly. At present, a great amount of microelectronics has been a silicon-based (Si-based) technology because of its mature process technology. However, it is expected that this Si-based technology will be replaced by other alternate semiconductor materials, such as germanium (Ge), III-V compounds,  $\text{Si}_{1-x}\text{Ge}_x$ ,  $\text{Ge}_{1-x}\text{Sn}_x$ . Among those semiconductors materials, Ge is often expected as one of the promising candidates due to its relative compatibility with silicon process and its high carrier mobility [58, 59]. As shown in Table 1.3, the effective electron mobility of Ge is over 2 times higher than that of Si, moreover, the effective hole mobility of Ge is over 4 times higher than that of Si.

Table 1.3 Comparison of the electrons and holes mobility between Si and Ge [60].

Effective mobility ( $\text{cm}^2/\text{V}\cdot\text{s}$ )	Si	Ge
Electron	1600	3900
Hole	430	1900

To realize the application of Ge-based microelectronics, developing a metal/Ge contacts with promising properties is quite necessary. Considering the fabrication process and its function in the device operation, the contact material should exhibit low sheet and contact resistance, good thermal stability, and low fabrication temperature. Based on those requirements, germanide, analogic to the application of silicide in current Si-based process, is known as one of the most promising contact materials, and those germanides could be used as a contact with source/drain and gate.

Gaudet [61] and his coworkers have systematically studied the thermally induced reaction of 20 transition metals (Ti, Zr, Hf, V, Nb, Ta, Cr, Mo, W, Mn, Re,

Fe, Ru, Co, Rh, Ir, Ni, Pd, Pt, and Cu) with Ge substrates, the phase formation sequence, sheet resistance, and the surface roughness for each metal/Ge system have been investigated to identify the most suitable contact material for Ge-based microelectronics. The first group of metals, including Ti, Zr, Hf, V, Nb, and Ta, have high germanidation temperature (above 450 °C), and are prone to be oxidized. The second group are Cr, Mo, Mn, Re, Rh, Ru, and Ir, the resistivity of the associated germanide is as high as above 130  $\mu\Omega\cdot\text{cm}$ , which is not suitable for the microelectronic applications. The third group, Fe, Co, Ni, Pd, Pt, and Cu, are the most interesting candidates because of their low formation temperature (150 - 360 °C) and low resistivity (22 - 129  $\mu\Omega\cdot\text{cm}$ ).

Among those leading materials, nickel monogermanide (NiGe) attracts considerable interest because of its low resistivity (approximately 22  $\mu\Omega\cdot\text{cm}$ ), low formation temperature (as low as 350 °C), final stable phase in Ni-Ge binary alloy system, and low Ge consumption for germanide formation. These advantages quite meet the requirement of nanoscale Ge-based microelectronics. However, the strong anisotropic properties of NiGe, with primitive orthorhombic structure in MnP-type ( $a=5.381 \text{ \AA}$ ,  $b=3.428 \text{ \AA}$ ,  $c=5.811 \text{ \AA}$ ) [62], might be one of the obstacles against its practical application. Firstly, due to an unusual negative thermal expansion coefficient along b-axis, positive ones along a and c-axis ( $\gamma_b = -5\times 10^{-6} \text{ K}^{-1}$ , and  $\gamma_a = 20\times 10^{-6} \text{ K}^{-1}$ ,  $\gamma_c = 25\times 10^{-6} \text{ K}^{-1}$ ) [63], the formation of NiGe layer might bring on local stress, and further result into rough surface or fractures in extreme case. Also, we should be concerned with the strong dependence of work functions  $\varphi_m$  on the crystalline orientation, which will cause the variability of electronic properties in nanoscale metal/Ge contacts (for the NiGe(100) surface,  $\varphi_m$  value is theoretically calculated to be 4.37 eV, while the highest one is 4.76 eV for the NiGe(101) surface.) [64].

## 1.5 Purpose and contents of this study

The purpose of this study is to develop a metal/Ge contact with low contact resistivity and feasible process for future highly scaled Ge-based MOSFET, like planar Ge MOSFET, Ge FinFET, etc. On the other hand, we also try to clarify the origin of FLP so as to find an effective way to alleviate the FLP, or further remove the FLP in extreme case. In order to achieve those purposes, the epitaxial

formation and electrical properties of NiGe/n-type Ge(001) and Ge(110) are systematically investigated. The reason why we choose NiGe as a contact material has been discussed in section 1.4. Next, we talk about the reason why we try to introduce epitaxial technology into the process of metal/Ge contact.

Besides the lower SBH of epitaxial metal/Ge contact as mentioned in section 1.3.4, there is another reason for the necessity of epitaxial metal layer. Because once contact dimension of nanometer technology devices scales down to a magnitude of grain size of contact materials, a variability of crystalline orientation of grains in metal contact materials may give rise to an unignorable variation of the work function [64] and morphology stability [65], particularly in the case of NiGe with strong anisotropic properties, that means, the problem of electrical fluctuation and non-reproducibility for each source and drain regions will occur for the polycrystalline contact layer. Therefore, the contact layer with polycrystalline structure may be not suitable for such nanometer technology devices, and the formation of an epitaxial contact layer and control of its relative orientations are quite required.

Compared with the epitaxial formation of silicide on Si substrate, the epitaxial formation of germanide on Ge substrate is much more difficult, since there are few germanide materials with good lattice matching with the diamond structure of Ge ( $a=5.6575 \text{ \AA}$ ). Fortunately, there are many ways to solve this problem. In previous studies, reactive deposition has been successfully conducted to form epitaxial cobalt germanide [66] and NiGe layers on Ge(001) [67] in an ultrahigh vacuum (UHV) chamber equipped with *in-situ* transmission electron microscope (TEM). Koike [68] also proposed an epitaxial formation of NiGe on Ge(001) substrate by inserting a thin interlayer (1-5 nm thick Sn layer). Of interesting, solid phase reaction somehow also contributes to the epitaxial formation of germanide layer even though the lattice mismatch between metal and Ge substrate is large. For example, high crystalline quality and threading dislocation free  $\text{Mn}_5\text{Ge}_3$  films can be epitaxially grown on Ge(111) substrate despite the existence of a misfit as high as 3.7% between epitaxial  $\text{Mn}_5\text{Ge}_3$  layer and Ge(111) substrate [69].

Therefore, we will conduct reactive deposition and solid phase reaction to form epitaxial NiGe layer on Ge(001) and Ge(110) substrates, and the epitaxial

formation mechanism also will be further investigated by considering the surface energy and strain energy. Finally, based on the investigation of crystalline structures of NiGe layer formed by the reactive deposition and solid phase reaction, the electrical properties of NiGe/Ge contact were studied to make clear the origin of FLP.

The construction of this dissertation is as follows. In chapter 2, the sample fabrication process and characterization method are introduced. In the chapter 3, we focus on the epitaxial formation of NiGe layer on Ge(110) substrate. At first, the effect of surface cleaning on the crystalline structure of NiGe layer will be discussed. Secondly, we talk about the dependence of epitaxial and polycrystalline growth of NiGe layer on the annealing temperature. Thirdly, the epitaxial formation mechanism of NiGe layer on Ge(110) substrate is established by considering its atomic arrangement. This chapter partly includes the results in our published paper, ref. 70 and 71. Chapter 4 is concerned with the epitaxial formation of NiGe layer on Ge(001) substrate, and a method to improve the epitaxial formation is proposed. This chapter partly includes the results in our submitted paper, ref. 72. Chapter 5 deals with the electrical properties of NiGe/Ge contact with various crystalline structures, and a summary of the effect of the crystalline structure on the electrical properties is given. Finally, the contribution to the Ge-based technology and academic theory in this study are summarized in chapter 6.

## References

- [1] I. Ferain, C.A. Colinge, J.P. Colinge, *Nature* **479**/7373 (2011) 310.
- [2] S.M. Sze, K.K. Ng, *Physics of semiconductor devices*, John Wiley & Sons, 2006.
- [3] N.H. Weste, K. Eshraghian, *Principles of CMOS VLSI design*, Addison-Wesley Reading, MA, 1993.
- [4] <http://www.itrs.net/Links/2013ITRS/2013Chapters/2013Overview.pdf>.
- [5] R.H. Dennard, F.H. Gaensslen, V.L. Rideout, E. Bassous, A.R. LeBlanc, *Solid-State Circuits*, *IEEE Journal of* **9**/5 (1974) 256.
- [6] G.E. Moore, *IEDM Tech. Digest* 11 (1975).
- [7] [http://en.wikipedia.org/wiki/Moore's\\_law](http://en.wikipedia.org/wiki/Moore's_law).
- [8] <http://www.itrs.net/Links/2011ITRS/2011Chapters/2011FEP.pdf>.
- [9] B. Anderson, R. Anderson, *Fundamentals of Semiconductor devices*, McGraw-Hill, Inc., 2004.
- [10] S.M. Sze, *Physics of semiconductor devices*, John Wiley & Sons, New York, 1981.
- [11] Intel Corporation, Press release, November 2007.
- [12] N. Kotani, S. Kawazu, *Solid-State Electronics* **22**/1 (1979) 63.
- [13] A. Dimoulas, A. Toriumi, S.E. Mohney, *MRS Bull* **34**/7 (2009) 522.
- [14] A.M. Noori, M. Balseanu, P. Boelen, A. Cockburn, S. Demuyneck, S. Felch, S. Gandikota, A.J. Gelatos, A. Khandelwal, J.A. Kittl, *Electron Devices*, *IEEE Transactions on* **55**/5 (2008) 1259.
- [15] N. Mott, *Mathematical Proceedings of the Cambridge Philosophical Society*, Cambridge Univ Press, 1938, p. 568.
- [16] W. Schottky, *Naturwissenschaften* **26**/52 (1938) 843.
- [17] E. Marshall, C. Wu, C. Pai, D. Scott, S. Lau, *MRS Proceedings*, Cambridge Univ Press, 1985, p. 161.
- [18] T. Nishimura, K. Kita, A. Toriumi, *Applied Physics Letters* **91**/12 (2007) 123123.
- [19] A. Dimoulas, P. Tsipas, A. Sotiropoulos, E.K. Evangelou, *Applied Physics Letters* **89**/25 (2006) 252110.
- [20] K. Ikeda, Y. Yamashita, N. Sugiyama, N. Taoka, S.-i. Takagi, *Applied Physics Letters* **88**/15 (2006) 152115.
- [21] M. Iyota, K. Yamamoto, D. Wang, H. Yang, H. Nakashima, *Applied Physics Letters* **98**/19 (2011) 192108.
- [22] H.B. Michaelson, *Journal of Applied Physics* **48**/11 (1977) 4729.
- [23] Y. Zhou, M. Ogawa, X. Han, K.L. Wang, *Applied Physics Letters* **93**/20 (2008) 202105.
- [24] C.C. Han, E.D. Marshall, F. Fang, L.C. Wang, S.S. Lau, D. Voreades, *Journal of Vacuum Science & Technology B* **6**/6 (1988) 1662.

- [25] R.R. Lieten, S. Degroote, M. Kuijk, G. Borghs, *Applied Physics Letters* **92/2** (2008) 022106.
- [26] A. Thanailakis, D.C. Northrop, *Solid-State Electronics* **16/12** (1973) 1383.
- [27] H.B. Yao, D.Z. Chi, R. Li, S.J. Lee, D.-L. Kwong, *Applied Physics Letters* **89/24** (2006) 242117.
- [28] Z. Shiyang, L. Rui, S.J. Lee, M.F. Li, A. Du, J. Singh, C. Zhu, A. Chin, D.L. Kwong, *Electron Device Letters, IEEE* **26/2** (2005) 81.
- [29] K. Ikeda, T. Maeda, S.-i. Takagi, *Thin Solid Films* **508/1–2** (2006) 359.
- [30] M. Mueller, Q.T. Zhao, C. Urban, C. Sandow, D. Buca, S. Lenk, S. Estévez, S. Mantl, *Materials Science and Engineering: B* **154–155/0** (2008) 168.
- [31] S.M.M. Coelho, F.D. Auret, P.J. Janse van Rensburg, C. Nyamhere, J.M. Nel, M. Hayes, *physica status solidi (c)* **5/2** (2008) 626.
- [32] A.M. Cowley, S.M. Sze, *Journal of Applied Physics* **36/10** (1965) 3212.
- [33] J. Bardeen, *Physical Review* **71/10** (1947) 717.
- [34] W.E. Spicer, A.M. Green, *Journal of Vacuum Science & Technology B* **11/4** (1993) 1347.
- [35] L.J. Brillson, *Journal of Vacuum Science & Technology A* **25/4** (2007) 943.
- [36] R.T. Tung, *Materials Science and Engineering: R: Reports* **35/1–3** (2001) 1.
- [37] V. Heine, *Physical Review* **138/6A** (1965) A1689.
- [38] A.W. Maue, *Z. Physik* **94/11-12** (1935) 717.
- [39] W. Mönch, *Semiconductor surfaces and interfaces*, Springer, 2001.
- [40] F. Flores, F. Garcia-Moliner, Cambridge University Press, Cambridge, 1979.
- [41] S. Louie, M. Cohen, *Physical Review B* **13/6** (1976) 2461.
- [42] J. Tersoff, *Physical Review B* **30/8** (1984) 4874.
- [43] J. Tersoff, *Physical Review Letters* **57/4** (1986) 440.
- [44] S.G. Louie, J.R. Chelikowsky, M.L. Cohen, *Physical Review B* **15/4** (1977) 2154.
- [45] F. Flores, C. Tejedor, *Journal of Physics C: Solid State Physics* **20/2** (1987) 145.
- [46] C. Tejedor, F. Flores, E. Louis, *Journal of Physics C: Solid State Physics* **10/12** (1977) 2163.
- [47] C. Tejedor, F. Flores, *Journal of Physics C: Solid State Physics* **11/1** (1978) L19.
- [48] T. Nishimura, K. Kita, A. Toriumi, *Applied Physics Express* **1** (2008) 051406.
- [49] Y. Zhou, M. Ogawa, X. Han, K.L. Wang, *Applied Physics Letters* **93/20** (2008) 202105.
- [50] R.R. Lieten, S. Degroote, M. Kuijk, G. Borghs, *Applied Physics Letters* **92/2** (2008) 022106.
- [51] M. Kobayashi, A. Kinoshita, K. Saraswat, H.-S.P. Wong, Y. Nishi, *Journal of Applied Physics* **105/2** (2009) 023702.

- [52] Y. Tong, B. Liu, P.S.Y. Lim, Y.-C. Yeo, *Electron Device Letters*, IEEE **33/6** (2012) 773.
- [53] H.-S. Wong, L. Chan, G. Samudra, Y.-C. Yeo, *Electron Device Letters*, IEEE **28/12** (2007) 1102.
- [54] M. Koike, Y. Kamimuta, T. Tezuka, *Applied Physics Letters* **102/3** (2013) 032108.
- [55] M. Koike, Y. Kamimuta, T. Tezuka, *Applied Physics Express* **4/2** (2011) 021301.
- [56] T. Nishimura, O. Nakatsuka, S. Akimoto, W. Takeuchi, S. Zaima, *Microelectronic Engineering* **88/5** (2011) 605.
- [57] K. Yamane, K. Hamaya, Y. Ando, Y. Enomoto, K. Yamamoto, T. Sadoh, M. Miyao, *Applied Physics Letters* **96/16** (2010) 162104.
- [58] Y.-J. Yang, W. Ho, C.-F. Huang, S. Chang, C. Liu, *Applied Physics Letters* **91/10** (2007) 102103.
- [59] T. Krishnamohan, D. Kim, T.V. Dinh, A.-T. Pham, B. Meinerzhagen, C. Jungemann, K. Saraswat, *Electron Devices Meeting, 2008. IEDM 2008. IEEE International*, IEEE, 2008, p. 1.
- [60] S. Takagi, T. Iisawa, T. Tezuka, T. Numata, S. Nakaharai, N. Hirashita, Y. Moriyama, K. Usuda, E. Toyoda, S. Dissanayake, M. Shichijo, R. Nakane, S. Sugahara, M. Takenaka, N. Sugiyama, *Electron Devices, IEEE Transactions on* **55/1** (2008) 21.
- [61] S. Gaudet, C. Detavernier, A.J. Kellock, P. Desjardins, C. Lavoie, *Journal of Vacuum Science & Technology A: Vacuum, Surfaces, and Films* **24/3** (2006) 474.
- [62] H. Pfisterer, K. Schubert, *Z. Metallkd* **41** (1950) 358.
- [63] C. Perrin, D. Mangelinck, F. Nemouchi, J. Labar, C. Lavoie, C. Bergman, P. Gas, *Materials Science and Engineering: B* **154–155/0** (2008) 163.
- [64] M. Niranjana, L. Kleinman, A. Demkov, *Physical Review B* **75/8** (2007) 085326.
- [65] D. Deduytsche, C. Detavernier, R. Van Meirhaeghe, J. Jordan-Sweet, C. Lavoie, *Journal of Applied Physics* **101** (2007) 044508.
- [66] H.P. Sun, Y.B. Chen, X.Q. Pan, D.Z. Chi, R. Nath, Y.L. Foo, *Applied Physics Letters* **86/7** (2005) 071904.
- [67] R. Nath, C.W. Soo, C.B. Boothroyd, M. Yeadon, D.Z. Chi, H.P. Sun, Y.B. Chen, X.Q. Pan, Y.L. Foo, *Applied Physics Letters* **86/20** (2005) 201908.
- [68] M. Koike, Y. Kamimuta, Y. Moriyama, Y. Kamata, E. Kurosawa, T. Tezuka, *Extended Abstracts of the 2013 International Conference on Solid State Devices and Materials*, Fukuoka, 2013, p. 600.
- [69] A. Spiesser, S. Olive-Mendez, M.-T. Dau, L. Michez, A. Watanabe, V. Le Thanh, A. Glachant, J. Derrien, A. Barski, M. Jamet, *Thin Solid Films* **518/6** (2010) S113.

- [70] Y. Deng, O. Nakatsuka, J. Yokoi, N. Taoka, S. Zaima, *Thin Solid Films* **557** (2014) 84.
- [71] Y. Deng, O. Nakatsuka, N. Taoka, S. Zaima, *Japanese Journal of Applied Physics* **53/5S2** (2014) 05GA06.
- [72] Y. Deng, O. Nakatsuka, A. Suzuki, M. Sakashita, S. Zaima. *Solid-State Electronics*. [*Submitted*]

## 2 Sample fabrication process and characterization method

### 2.1 Sample preparation

#### 2.1.1 Surface cleaning process

The substrates used were n-type Ge(110) and Ge(001). The Ge wafers were chemically cleaned by dipping in a diluted HF solution and rinsing in deionized water repeatedly for five times to remove contaminations and the surface oxide layer. After wet cleaning, the Ge wafer was dried with N<sub>2</sub> blow and immediately introduced into an ultra-high-vacuum (UHV) chamber whose base pressure was below  $2.5 \times 10^{-5}$  Pa. Note that a native oxide layer was formed during the transfer of the sample from the atmosphere into the UHV chamber [1]. Thermal cleaning was performed at 550 °C for 30 min in the UHV chamber to remove the native oxide layer for some samples. Some samples were not treated with thermal cleaning to investigate the effect of the native oxide layer on the epitaxial formation of the NiGe layer. The detail surface cleaning process is shown in Table 2.1.

Table 2.1 Surface cleaning process before Ni deposition.

Process number	Chemical solution	Treatment	Time
1	Deionized water	Overflow	5 min
2	Diluted HF solution (1%)	Dip	1 min
3	Deionized water	Overflow	1 min
4	Repeat process 2 and 3 for 3 times		
5	Diluted HF solution (1%)	Dip	1 min
6	Deionized water	Overflow	<1 min
7	Load into UHV chamber	550 °C desorption	30 min

#### 2.1.2 Ni deposition and germanidation

In this study, an electron beam evaporation method is used to deposit Ni layer. Basically, this deposition method is some kind of physical vapor deposition. The deposition fundament is instructed as follows: at first, electron beam is

generated by thermionic emission method from a tungsten filament, then this generated electron beam is accelerated, and is steered by an additional electrical and magnetic field to bombard the Ni target. Once the high energy electron beam reaches to the Ni target, the Ni target is heated up through converting the kinetic energy of electron beam into the thermal energy of Ni target, thus the Ni atoms are evaporated if the heated temperature is high enough. Finally, the evaporated Ni atoms would precipitate into solid form once landing onto Ge substrate, thus the deposition of Ni onto Ge substrate is achieved.

The schematic diagram of electron beam evaporation equipment is shown in Figure 2.1. The deposition chamber is vacuumed by a rotary pump and a mechanical booster pump, and the vacuum pressure is maintained around  $1 \times 10^{-5}$  Pa. During the Ni deposition, the vacuum pressure is decreased to approximately  $4-7 \times 10^{-5}$  Pa due to the evaporation of Ni atoms. On the other hand, the deposition rate and the thickness of as-deposited Ni layer are monitored by the quartz crystal microbalance, which has been calibrated before Ni deposition. In this study, the deposition rate is controlled at  $0.1 \text{ \AA/s}$  by adjusting the filament current and high voltage.

For the solid phase reaction, a 20- or 30-nm-thick Ni layer was deposited at room temperature. Then, after the as-deposited sample was cooled down in 3 - 6 hours, we take out the sample, and immediately introduce the as-deposited sample into a furnace chamber. Next, germanidation is conducted at 200 - 550 °C for a time ranging from 30 s to 5 min in N<sub>2</sub> ambient.

Different from the solid phase reaction, the reactive deposition method is performed at 350 °C (temperature of substrate), which is high enough to drive the reaction between as-deposited Ni and Ge substrate. In other words, the Ni deposition and germanidation are completed simultaneously for reactive deposition, while solid phase reaction is conducted by post germanidation after the process of Ni deposition.

Moreover, a 2-steps deposition, combined with solid phase reaction, is proposed. After the reactive deposition of a 5 nm-thick Ni layer at 350 °C to form thin Ni germanide layer, a 15 nm-thick Ni layer was additionally deposited at room temperature, then, this sample was taken out in atmosphere and annealed at 350 °C for 30 s in N<sub>2</sub> ambient using rapid thermal annealing (RTA) system.

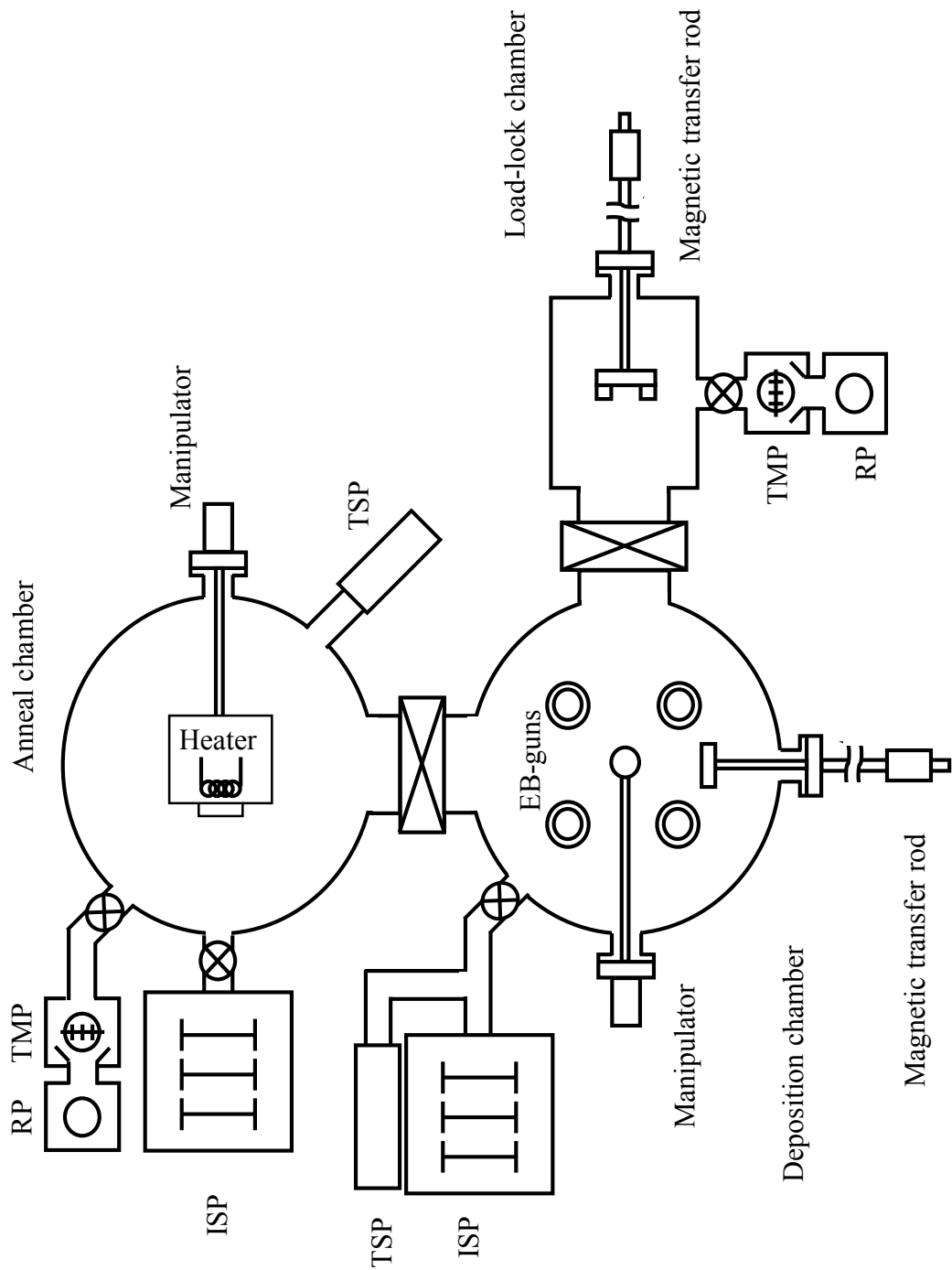


Figure 2.1 The schematic diagram of electron beam deposition equipment.

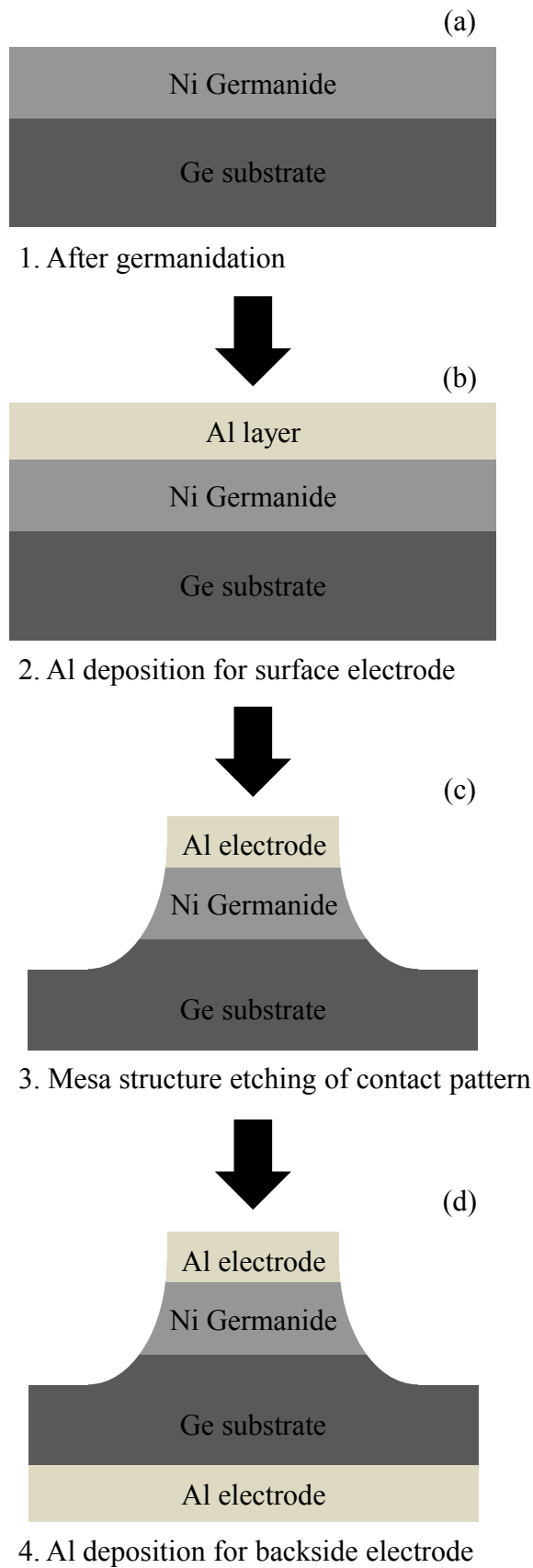


Figure 2.2 The process flow for fabricating the Schottky diode.

### **2.1.3 Fabrication process of Schottky diodes**

Figure 2.2 shows the process flow for fabricating a Schottky diode, note that those schematic diagrams are not drawn in scale. We started from the process after germanidation, the structure is shown in Figure 2.2(a). To know the processes of Ni deposition and germanidation in detail, please refer to section 2.1.2.

Followed by the process of germanidation, about a 500 - 1000 nm Al layer, which plays a role of electrode in Schottky diode, was thermally evaporated under the vacuum condition of  $5.0 \times 10^{-3}$  Pa firstly, as shown in Figure 2(b). Secondly, a resist layer was spin coated onto the Al/NiGe/Ge structure, using a speed of 5000 rpm for 30 s. To dry this sample, a baking at 90 °C for 9 s was conducted. Next, an etching window was opened by traditional photolithography. Then, a mesa structure was formed by wet etching at  $50 \pm 5$  °C for 4 min, the portion of wet etching solution was  $\text{H}_2\text{PO}_4$ :  $\text{CH}_3\text{COOH}$ :  $\text{HNO}_3$  = 250:20:3. Finally, after removing the remained resist by a MS2001 solution, a round contact pattern with various areas, e.g., 1000  $\mu\text{m}$  (diameter), 750  $\mu\text{m}$ , 500  $\mu\text{m}$ , was formed, the cross sectional structure is shown in Figure 2.2(c). The last process was the fabrication of backside electrode, which is same as the fabrication of surface electrode. The completed Schottky diode is shown in Figure 2.2(d).

## **2.2 Characterization of the crystalline structure**

### **2.2.1 X-ray diffraction**

X-ray diffraction (XRD) is one of the primary techniques often used in thin film field, including the identification of the crystalline phase and crystalline structure, evaluation of the stress and strain, and investigation of the texture. When an incident beam of monochromatic X-ray strikes a crystal material with a regular array of atoms, an elastic scattering occurs due to the interaction between the atoms and the incident beam. Since the atoms are regularly arrayed in the crystal materials, the scattered X-rays from those regularly arrayed atoms undergo constructive and destructive interference. Assuming the spacing between diffraction planes is  $d$  and the wavelength of the incident X-ray beam is  $\lambda$ , we can find a diffraction beam in the direction described by the  $2\theta$  the angle between incident beam and diffraction beam, this diffraction angle could be given by

Bragg's law,  $n\lambda = 2d\sin\theta$ . By inspecting this Bragg's law, we can easily get a conclusion that a specific lattice plane has its own diffraction angle  $2\theta$ , in other words, each material with specific crystal structure has a set of corresponding diffraction peaks, which is characterized by the diffraction angle  $2\theta$  and the intensity of the diffraction peak. The schematic diagram of the XRD equipment is shown in Figure 2.3, this equipment is mainly composed of X-ray source generator, incident slit, sample holder, and X-ray detector.

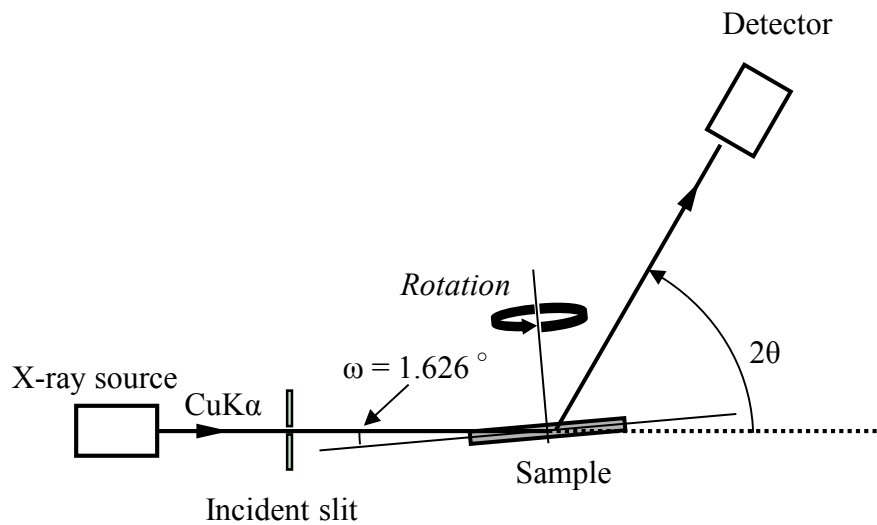


Figure 2.3 The schematic diagram of X-ray diffraction equipment.

In this study, grazing angle XRD ( $2\theta$  scan,  $\omega = 1.626^\circ$ ) and out-of-plane XRD ( $2\theta/\omega$  scan) using a Cu K $\alpha$  source ( $\lambda = 1.5405$  nm) were performed to investigate the crystalline structure of Ni germanide layer. Generally, grazing angle XRD is used to detect the polycrystalline growth of thin film, because the experimental angle of the grazing angle XRD is symmetrically changed, the scan trace in reciprocal map of Ge, in which the primary plane is Ge(110), and the secondary primary plane is Ge( $\bar{1}10$ ), is indicated by the dash arc in Figure 2.4. This scan trace could detect the diffraction plane from the random oriented grains. On the other hand, out-of-plane XRD shows us the diffraction plane of film parallel to the surface of substrate, and is often used to detect the epitaxial growth, because the experiment angle follows the relationship of  $\omega = 2\theta/2$ , namely, the scanning trace of out-of plane XRD is along the normal direction of substrate, as indicated by the dash line in Figure 2.4.

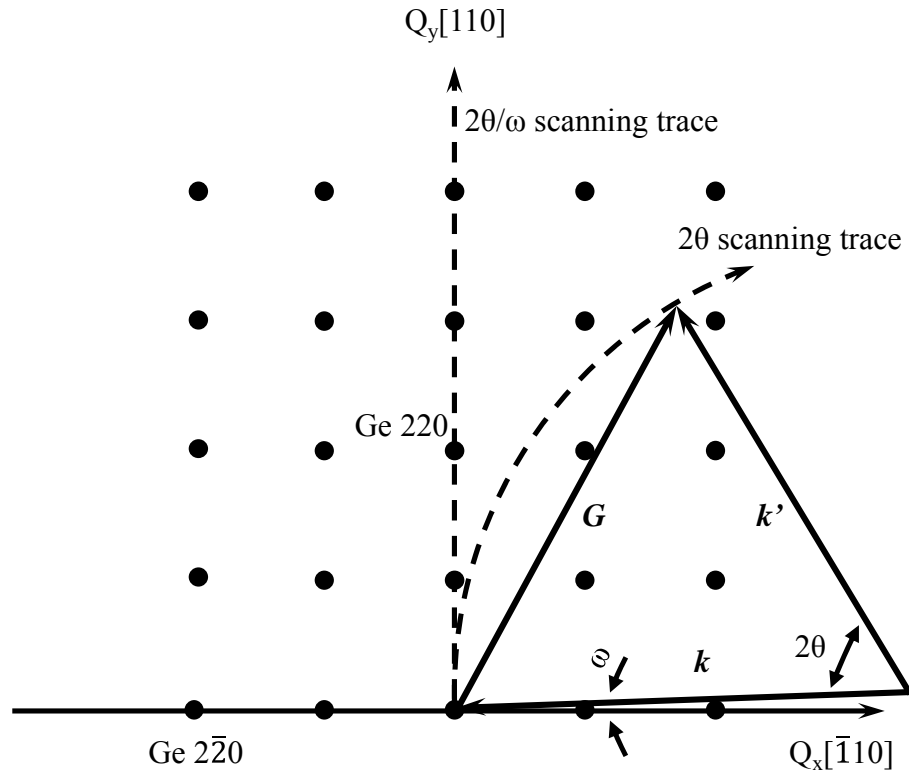


Figure 2.4 The scanning trace of  $2\theta$  and  $2\theta/\omega$  scan.

We also use x-ray diffraction two-dimensional reciprocal space mapping (XRD-2DRSM) to evaluate the residual stress and strain in the NiGe layer, which may be due to the misfit of lattice plane between the epitaxial NiGe layer and Ge substrate, or the difference of the thermal expansion efficiency between NiGe layer and Ge substrate, or the volume expansion during the phase transformation from Ni layer to NiGe layer. Assuming that there is an in-plane uniaxial tensile strain in the film, the in plane and out of plane lattice constant of the film would increase and decrease, respectively. As for the compressive strain in the film, the variations of the in plane and out of plane lattice constant are opposite. Therefore, by comparison the lattice constant of the strained film with that of the strain-free film (theoretical calculation based on the crystalline structure), the strain and stress could be evaluated by the XRD-2DRSM. Note before calculating the variation of the lattice constant of the film, the experimental results  $2\theta$  and  $\omega$  in the XRD-2DRSM, which could describe the lattice constant by Equation (2.1a) and (2.1b), should be calibrated by those values of substrate.

$$Q_x = \frac{1}{\lambda} \{ \cos \omega - \cos(2\theta - \omega) \} \quad (2.1a)$$

$$Q_y = \frac{1}{\lambda} \{ \sin \omega + \sin(2\theta - \omega) \} \quad (2.1b)$$

## 2.2.2 Transmission electron microscopy

Transmission electron microscopy (TEM) is known as a central tool for complete characterization of nanoscale materials and devices because of its high spatial resolution. Basically, TEM technique also relies on the Bragg' law, same with the XRD technique as mentioned in section 2.2.1. The main difference between TEM and XRD is the beam source, the beam source of TEM is electron beam, while XRD is X-ray (usually Cu K $\alpha$ ). And the high resolution of TEM is contributed by this electron beam source, the resolution could be approximately describe by equation  $\lambda = \frac{1.22}{E^{1/2}}$ , where  $\lambda$  is the resolution with a unit nm,  $E$  is the electron energy with a unit eV, hence, for a 100 keV electron,  $\lambda$  is about 0.004 nm, which is much smaller than the diameter of an atom [2].

Next, we briefly introduce the electron beam transmission path in a TEM apparatus, as shown in Figure 2.5 [3]. After a Wehnelt thermionic or field electron emission from a filament to the vacuum, the electron beam is manipulated and converged by a set of lenses with a magnetic field. Typically, a TEM apparatus consists of three lenses, including the condenser lens, objective lens, and projector lens. These lenses work at a given position in the electron beam transmission path, the condenser lens have a responsibility for the primary beam formation, the objective lens is used to focus the beam that penetrates through a thin specimen, note additional objective lens above the specimen is used to convergent the incident electron beam for cross sectional TEM scanning mode, the projector lens expand the electron beam onto the detector, like phosphor screen, CCD camera, etc.

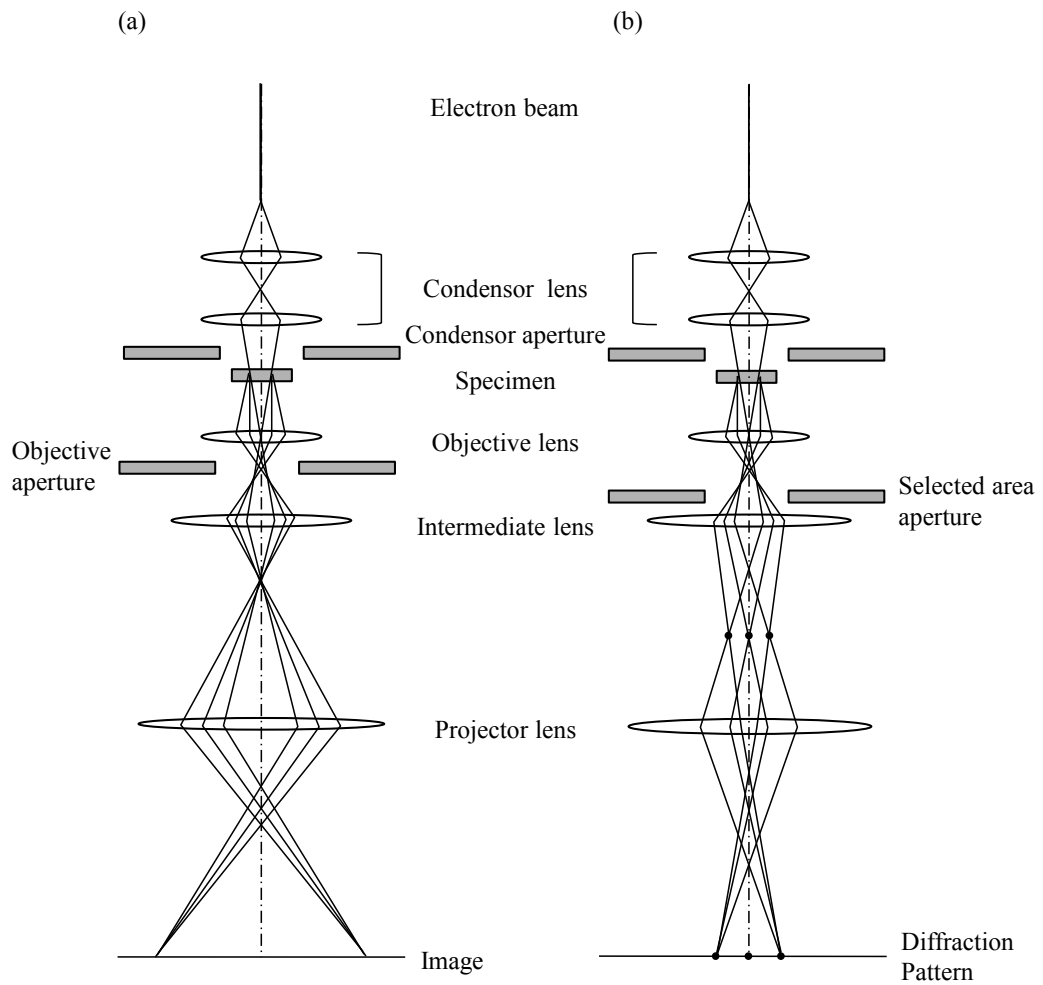


Figure 2.5 The schematic diagram of the optical configuration: (a) TEM observation, (b) TED measurement.



### 2.2.3 Reflection high energy electron diffraction

Reflection high energy electron diffraction (RHEED) technique is a kind of electron beam relied technique, like TEM, thus we can investigate the crystalline structure of film by analyzing the RHEED pattern similar with TED pattern, for example, when the film is polycrystalline, the RHEED pattern exhibits a ring pattern, while the RHEED pattern for an epitaxial film will show a streak or spot pattern (discussed later).

However, RHEED technique has some unique features, which makes RHEED technique different from TEM technique. One is that the TEM observation is realized by the penetration of electron beam through a thin specimen, whereas, the RHEED pattern could be easily obtained by making the incident beam graze the surface of the film, the schematic diagram [4] of this technique is shown in Figure 2.6(a). To introduce the principle of this technique, we take a fcc (100) surface as an example, and the corresponding reciprocal map is inserted in the lower right of Figure 2.6(a). When the set of lattice planes 00, 01, 02, etc., meets the Bragg's law, which is described by the Ewald's sphere, the corresponding diffraction beams could be detected by a CCD camera or phosphor screen, such as 00 spot, and 01 spot, and the typical RHEED pattern based on the reciprocal space map of fcc (001) surface is shown in Figure 2.6(b).

The second unique feature of RHEED technique is the relative low energy of the incident beam, generally, the electron gun of TEM apparatus is operated above 100 keV, whereas, that of RHEED is done as low as 10 - 30 keV. Due to this relatively low energy of incident beam, the penetration depth of incident beam into a film is approximately 1 nm, namely, RHEED technique is very sensitive to the surface state. When the surface of an epitaxial layer is rough, the RHEED pattern will exhibit spot characteristic, while a streak RHEED pattern will be obtained for an atomically flat surface. Another benefit from this relatively low energy of incident beam is the ignorable damage to the film due to the bombardment by the electron beam, hence, RHEED technique could be used as an *in-situ* surface characterization method during the film growth.

In this study, an electron energy of 26 keV is used for the RHEED measurement to confirm whether a native oxide layer has been desorbed by thermal cleaning, as mentioned in section 2.1.1. And *in-situ* RHEED measurement

is also conducted to characterize the surface information of the reactive deposited NiGe layer, including the crystalline structure and surface roughness.

#### **2.2.4 Atomic force microscopy**

We also used atomic force microscopy (AFM) to investigate the evolution of the surface topography of Ni/Ge system with the increase of the annealing temperature. AFM is a kind of scanning probe microscopy with a very high resolution. The measurement principle and a typical set up of AFM apparatus are shown in Figure 2.7(a) and 2.7(b), respectively. A cantilever with a sharp tip at its end is precisely controlled by piezoelectric elements, which consists of surface movement controller and height movement controller. When the tip is brought close to the surface, an atomic force between the tip and the sample results in a deflection of the cantilever, which is detected by the so called “position sensor”. According to Hooke’s law, the strain in the cantilever could be measured based on the deflection detection. During the scanning process, in turn, we maintain a constant force in the cantilever, namely, the deflection of the cantilever is kept at a constant distance between the tip and the sample. Thus, the surface topography could be characterized by the adjustment of the distance between the tip and the sample.

As mentioned in the previous paragraph, one of the main parts of AFM apparatus is the position sensor. Typically, a position sensor consists of a laser diode, a set of mirrors, a four-quadrant photodetector and a differential amplifier, as shown in Figure 2.7(b). A laser, generated from the laser diode, is reflected onto the cantilever by a set of mirrors, and finally the laser is reflected by the cantilever to a four-quadrant photodetector. According to the position of laser spot in the four-quadrant photodetector, the deflection of the cantilever could be detected, thus the measurement of surface topography is realized.

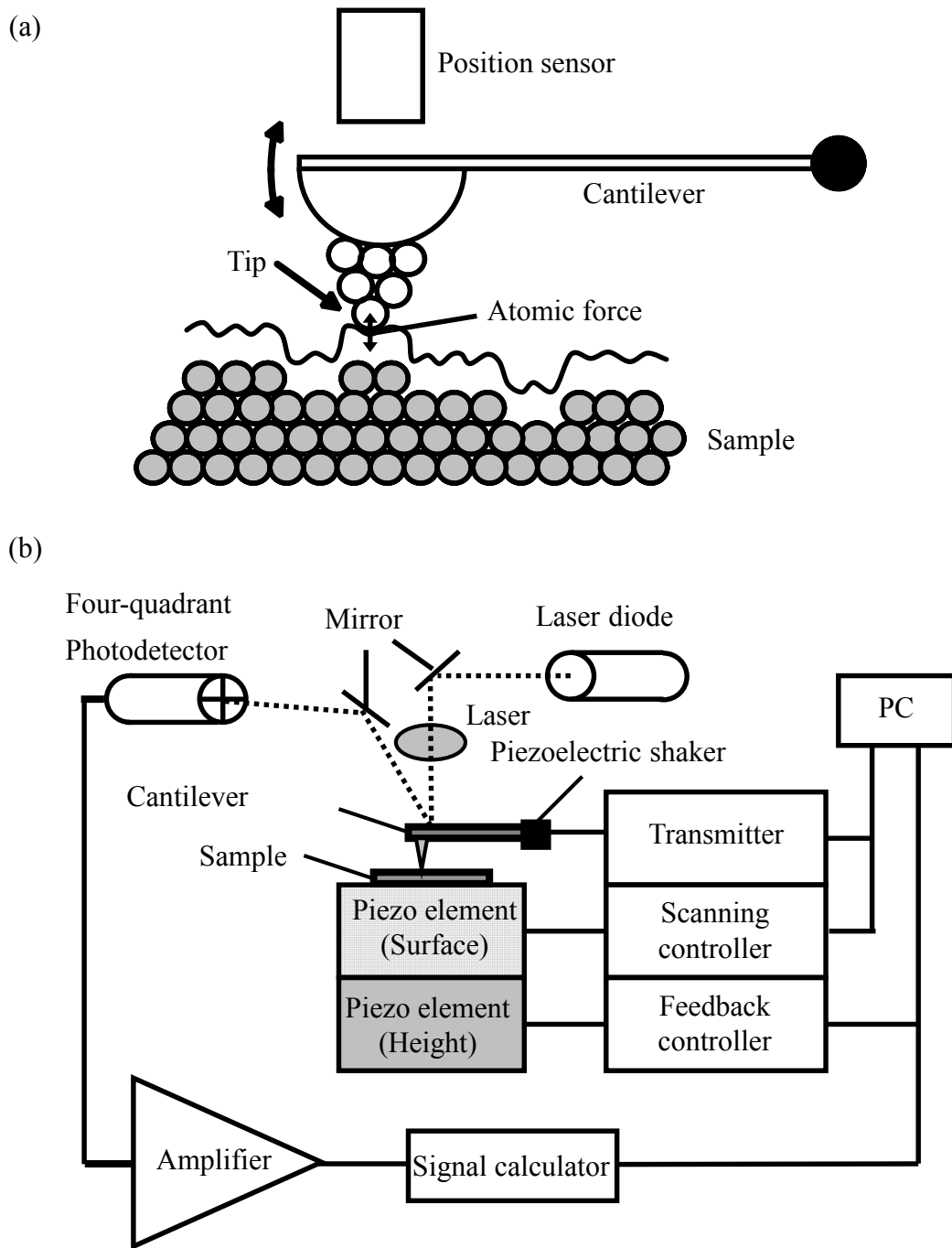


Figure 2.7 (a) Schematic diagram of the principle of AFM, (b) a typical set up of AFM apparatus.

## 2.3 Characterization of the electrical property

The current transport in metal/semiconductor contacts is mainly due to the majority carriers. Considering a forward bias, four basic transport processes is shown in Figure 2.8. One is the transport of electrons from the semiconductor into the metal, whose energy is high enough to overcome the potential barrier. This transport process is a dominant one for a Schottky diode with moderately doped semiconductors. The second one is quantum mechanical tunneling of electrons through the barrier, which often happens when the semiconductor is heavily doped. The third one is the recombination of hole and electron pairs in the space charge region. The fourth one is the hole injection from the metal to the semiconductor, like the recombination happened in the neutral region. Note that besides the four current transport processes, an edge leakage current and interface current are often observed in our study, the high electric field at the contact periphery and the traps at the interface of metal/semiconductor might take the responsibility of the edge leakage current and interface current, respectively.

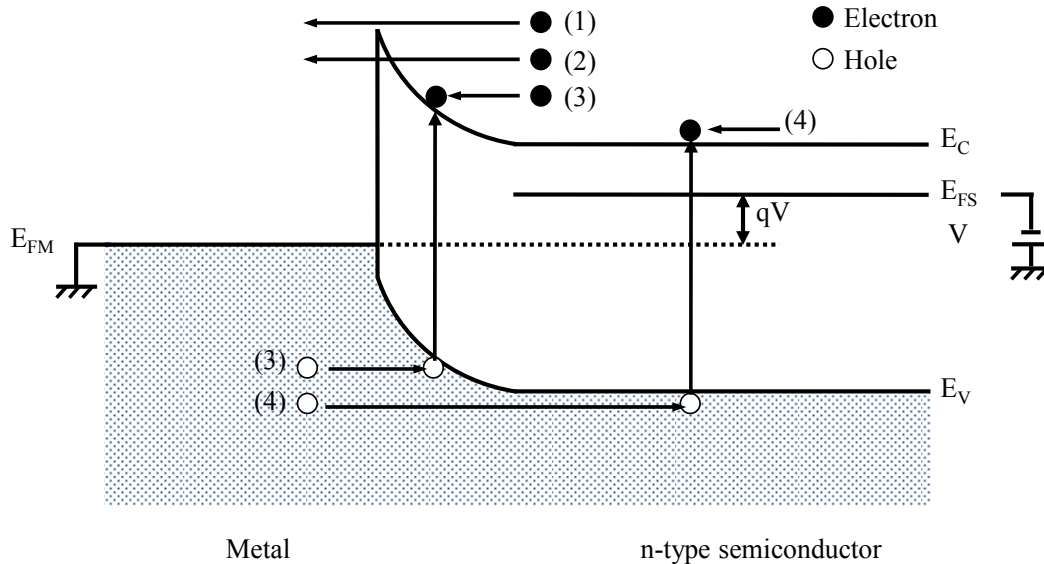


Figure 2.8 Four basic current transport processes in metal/n-type semiconductor contact under forward bias.

- (1) Transport of electrons from the semiconductor over the potential barrier into the metal.
- (2) Quantum mechanical tunneling of electrons through the barrier.
- (3) Recombination in the space-charge region.
- (4) Hole injection from the metal to the semiconductor.

In this section, we only discuss the transport of electrons over the potential barrier, since this transport mechanism is the dominate one for metal/n-type Ge contact in this study. To understand the other transport mechanism, we recommend one to refer to a book [5]. And we consider a thermionic emission theory [6] to describe this transport current. At first, we assume a thermal equilibrium is established, and the net current flow, a sum of the current fluxes due to electron transport from metal to semiconductor (denoted as reverse current  $I_{m \rightarrow s}$ ) and the other one from semiconductor to metal (denoted as forward current  $I_{s \rightarrow m}$ ), does not affect this equilibrium. The other assumption is that the current flow is determined solely by the barrier height. Therefore, the current density  $J_{s \rightarrow m}$  could be given by the concentration of those electrons with enough high energy to overcome the barrier height,

$$J_{s \rightarrow m} = \int_{E_F + q\Phi_B}^{\infty} qv_x dn(E) \quad (2.2)$$

Where  $E_F + q\Phi_B$  is the minimum energy required for an electron to be thermionically emitted into metal,  $v_x$  is the carrier velocity in the direction from semiconductor to metal,  $dn(E)$  is the electron density in an incremental energy range  $E$ . By multiplication the density of states  $N(E)$  with the distribution function  $F(E)$ ,  $dn(E)$  could be described by Equation (2.3)

$$\begin{aligned} dn(E) &= N(E)F(E)dE \\ &= \frac{4\pi(2m^*)^{\frac{3}{2}}}{h^3} (E - E_c)^{\frac{1}{2}} \exp\left(-\frac{E - E_c + qV_n}{k_B T}\right) dE \end{aligned} \quad (2.3)$$

Where  $m^*$  is the effective electron mass of the semiconductor, and the product  $qV_n$  is  $E_c - E_F$ ,  $k_B$  is Boltzmann's constant, and  $h$  is Planck constant.

Next, considering that all the energy of electrons in the conduction band is kinetic energy, thus we have

$$E - E_c = \frac{1}{2} m^* v^2 \quad (2.4)$$

$$\sqrt{E - E_c} = v \sqrt{\frac{m^*}{2}} \quad (2.5)$$

$$dE = m^* v dv \quad (2.6)$$

Substitute Equation (2.4) - (2.6) into Equation (2.3), the electron density in an incremental speed has the form

$$N(E)F(E)dE = 2\left(\frac{m^*}{h}\right)^3 \exp\left(-\frac{qV_n}{k_B T}\right) \exp\left(-\frac{m^* v^2}{k_B T}\right) (4\pi v^2 dv) \quad (2.7)$$

On the other hand, the velocity  $v$  has three components in  $x$ ,  $y$ ,  $z$  directions, as mentioned previously, the electron transport direction is along  $x$  direction, thus combining the conditions  $v^2 = v_x^2 + v_y^2 + v_z^2$  and  $4\pi v^2 dv = dv_x dv_y dv_z$ , Equation (2.2) is transformed into

$$J_{s \rightarrow m} = \left(\frac{4\pi q m^* k_B^2}{h^3}\right) T^2 \exp\left(-\frac{qV_n}{k_B T}\right) \exp\left(-\frac{m^* v_{ox}^2}{k_B T}\right) \quad (2.8)$$

Where  $v_{ox}$  is the minimum velocity required for an electron to overcome the barrier, and this parameter could be obtained by solving the equation  $\frac{1}{2} m^* v_{ox}^2 = q(V_{bi} - V)$ , where  $V$  is the applied voltage,  $V_{bi}$  is the built-in potential at zero bias, as shown in Figure 1.10. Finally, the current density  $J_{s \rightarrow m}$  is given by

$$J_{sm} = A^* T^2 \exp\left(-\frac{q\Phi_B}{k_B T}\right) \exp\left(\frac{V}{k_B T}\right) \quad (2.9)$$

$$\Phi_B = V_n + V_{bi} \quad (2.10)$$

$$A^* = \frac{4\pi q m^* k_B^2}{h^3} \quad (2.11)$$

where  $\Phi_B$  is the barrier height, and equals to the sums of  $V_n$  and  $V_{bi}$ ,  $A^*$  is the effective Richardson constant [5] for thermionic emission. As for Si case,  $A^*$  is 250 and 79 A/cm<sup>2</sup>K<sup>2</sup> for electron and hole, respectively, while those of electron and hole in Ge case are 143 and 41 A/cm<sup>2</sup>K<sup>2</sup> [7].

Next, we demonstrate the current density  $J_{m \rightarrow s}$ . Since the barrier height for electron transporting from metal to semiconductor does not depend on the applied voltage, the current contributed by electron transport from metal to semiconductor is constant no matter how much the voltage is applied. Thus, we could easily obtain this reverse current by considering the equilibrium state when the applied voltage is zero. Under this condition, the current density  $J_{m \rightarrow s}$  is equal to the current density  $J_{s \rightarrow m}$ , thus by setting  $V = 0$ , we obtain the current density  $J_{m \rightarrow s}$

$$J_{m \rightarrow s} = -J_{s \rightarrow m}(V = 0) = -A^* T^2 \exp\left(-\frac{q\Phi_B}{k_B T}\right) \quad (2.12)$$

Finally, the net current density could be given by the sum of Equation (2.9) and (2.12),

$$J = J_s \left\{ \exp\left(\frac{qV}{k_B T}\right) - 1 \right\} \quad (2.13)$$

where  $J_s$  is the saturation current densities, this parameter has the form,

$$J_s \equiv A^* T^2 \exp\left(-\frac{q\Phi_B}{k_B T}\right) \quad (2.14)$$

In practical experiment, the net current density is not only contributed by thermionic emission current component, but also sometimes contributed by other current component, such as tunneling current as mentioned in the previous part. Thus, we introduce the ideality factor  $n$  to judge whether the thermionic emission current dominates the current flow. The Equation (2.13) is rewritten as follows

$$J = J_s \left\{ \exp\left(\frac{qV}{nk_B T}\right) - 1 \right\} \quad (2.15)$$

where the ideality factor  $n$  is defined as

$$n \equiv \frac{q}{k_B T} \frac{\partial V}{\partial(\ln J)} \quad (2.16)$$

When the thermionic emission current is the majority contributor (e.g., for low dopings, at high temperature), the ideality factor  $n$  is very close to a unity. However, this parameter departs from the unity when the doping is high or the measurement temperature is low, which means that the majority contributor of the current flow is other transport mechanism except the thermionic emission current. Furthermore, if  $V \gg kT/q$ , or  $V > 3kT/q$ , Equation (2.15) is approximated

$$J \approx J_s \exp\left(\frac{qV}{nk_B T}\right) \quad (2.17)$$

### 2.3.1 Current-Voltage measurement

As discussed in the last section, for a moderately doped semiconductor, and  $V > 3kT/q$ , the current density-voltage ( $J$ - $V$ ) characteristics is described by Equation (2.15). Thus, the saturation current densities  $J_s$  and ideality factor  $n$  could be obtained by fitting the experimental  $J$ - $V$  characteristics in forward bias using Equation (2.15). On the other hand, over a limited range of measurement temperature, e.g., 250K - 300K in this study, the value  $A^*$  and  $\Phi_B$  are nearly independent on the measurement temperature. Therefore, according to Equation

(2.14), the slope of an Arrhenius plot of  $\ln(J_s/T^2)$  versus  $1/T$  yields the Schottky barrier height  $\Phi_B$  [8], as described in Equation (2.18),

$$\ln\left(\frac{J_s}{T^2}\right) = \ln(A^*) - \frac{q\Phi_B}{kT} \quad (2.18)$$

And the intercept at  $1/T=0$  gives the parameter  $A^*$ , which is a product of the electrically active area and the effective Richardson constant.

### 2.3.2 Capacitance-Voltage measurement

The Schottky barrier height is also estimated by capacitance-voltage ( $C$ - $V$ ) method [9, 10]. For a metal/semiconductor with a uniformly impurity concentration, the relationship between capacitance  $C$  and applied voltage  $V$  is often given by

$$C \equiv \frac{|\partial Q_{sc}|}{\partial V} = \sqrt{\frac{q\epsilon_s N_D}{2(V_{bi} - V - \frac{k_B T}{q})}} \quad (2.19)$$

Where  $Q_{sc}$  is the space charge per unit area of the semiconductor,  $q$  is the electronic charge,  $\epsilon_s$  is the permittivity of semiconductor,  $N_D$  is the net donor concentration,  $V_{bi}$  is the built-in potential,  $k_B$  is Boltzmann's constant, and  $T$  is the measurement temperature.

To estimate the Schottky barrier height, Equation (2.19) is often transformed as follows,

$$\frac{1}{C^2} = \frac{2(V_{bi} - V - \frac{k_B T}{q})}{q\epsilon_s N_D} \quad (2.20)$$

Based on this equation, the built-in potential  $V_{bi}$  could be extrapolated from the intercept on the voltage axis in a plot of  $1/C^2$  versus the applied voltage  $V$ , moreover, the impurity concentration  $N_D$  could be calculated by the slope of  $1/C^2$  as a function of applied voltage  $V$ , the detail is as follows

$$N_D = \frac{2}{q\epsilon_s} \frac{dV}{d\left(\frac{1}{C^2}\right)} \quad (2.21)$$

On the other hand, according to the energy band diagram of metal/semiconductor, as shown in Figure 1.10, the Schottky barrier height could be expressed by the sum of  $V_{bi}$  and  $V_n$ , and the Equation (2.10) is rewritten here

$$\Phi_B = V_n + V_{bi} \quad (2.10)$$

where  $V_n$  is the energy difference between  $E_c$  and  $E_F$  of semiconductor, this parameter is a function of the impurity concentration  $N_D$

$$V_n = \frac{k_B T}{q} \ln \left( \frac{N_C}{N_D} \right) \quad (2.22)$$

where  $N_C$  is the effective density of states in the conduction band. Therefore, combining Equation (2.21), (2.10), and (2.22), the Schottky barrier height could be obtained.

## References

- [1] S.K. Sahari, H. Murakami, T. Fujioka, T. Bando, A. Ohta, K. Makihara, S. Higashi, S. Miyazaki, Japanese Journal of Applied Physics **50**/4 (2011) 04DA12.
- [2] D.B. Williams, C.B. Carter, The Transmission Electron Microscope, Springer, 1996.
- [3] 坂公恭, 結晶電子顕微鏡学: 材料研究者のための, 内田老鶴圃, 1997.
- [4] 表面科学会, 表面分析技術選書ナノテクノロジーのための表面電子回折法, 丸善株式会社, 2003.
- [5] S.M. Sze, Physics of semiconductor devices, John Wiley & Sons, New York, 1981.
- [6] H.A. Bethe, Theory of the boundary layer of crystal rectifiers, Radiation Laboratory, Massachusetts Institute of Technology, 1942.
- [7] C.R. Crowell, Solid-State Electronics **8**/4 (1965) 395.
- [8] K. Chino, Solid-State Electronics **16**/1 (1973) 119.
- [9] C. Crowell, J. Sarace, S. Sze, TRANSACTIONS OF THE METALLURGICAL SOCIETY OF AIME **233**/3 (1965) 478.
- [10] A.M. Goodman, Journal of Applied Physics **34**/2 (1963) 329.

## 3 Epitaxial formation of Ni Germanide on Ge(110) substrate

### 3.1 Background

By introducing an uniaxial compressive strain along Ge[ $\bar{1}10$ ] direction, a Ge(110) channel is reported to have a highest hole mobility compared with Si and Ge with other strain structures, or other surface orientations [1]. Thus, the Ge(110) channel has attracted a great interest, and is expected as one of the promising candidates for the future high speed germanium metal-oxide-semiconductor field effect transistor (Ge MOSFET).

Considering this potential application of Ge(110) channel, developing a metal/Ge(110) contact becomes quite imperative for realizing the Ge(110)-channel-based MOSFET device. However, so far, there are few reports on the metal/Ge(110) contact, including the contact formation and its electrical properties, although the metal/Ge contact has been extensively studied, most of those reported works only focus on metal/Ge(001) contact [2-5]. Therefore, we have to investigate the metal contact formed on Ge(110) substrates other than Ge(001).

Considering the self-align contact formation process for the nanoscale transistor structure, metal germanide formed by solid-phase reaction is one of the promising candidates for contact materials. Recently, germanides with various metals such as Er [4], Ti [6], Co [7], Pt [8], Pd [2], and Ni [9] have been investigated. Among these leading germanides, nickel monogermanide (NiGe) attracts considerable interest because of its low resistivity (approximately 22  $\mu\Omega\cdot\text{cm}$ ), low formation temperature (as low as 350 °C), final stable phase in Ni-Ge binary alloy system, and low Ge consumption for germanide formation [10]. These advantages quite meet the requirement of nanoscale Ge MOSFET, so the contact material we choose in this study is NiGe, with a primitive orthorhombic structure in MnP-type ( $a = 5.381 \text{ \AA}$ ,  $b = 3.428 \text{ \AA}$ ,  $c = 5.811 \text{ \AA}$ ) [11].

However, the strong anisotropic properties of NiGe might be one of the obstacles against its practical application in subnano Ge MOSFET. Firstly, due to an unusual negative thermal expansion coefficient along b-axis, positive ones along a and c-axis ( $\gamma_b = -5 \times 10^{-6} \text{ K}^{-1}$ , and  $\gamma_a = 20 \times 10^{-6} \text{ K}^{-1}$ ,  $\gamma_c = 25 \times 10^{-6} \text{ K}^{-1}$ ) [12],

the polycrystalline NiGe layer might have a large local strain, which may result into a rough surface or fractures in extreme case. Secondly, there is also another concern of the strong dependence of work functions  $\varphi_m$  on the crystalline orientation, for the NiGe(100) surface,  $\varphi_m$  value is theoretically calculated to be 4.37 eV, while the highest one is 4.76 eV for the NiGe(101) surface [13], this large variation of work function may cause a variability and non-reproducibility of the electronic properties for each polycrystalline NiGe/Ge contacts when the contact area scales down to a magnitude of the grain size of contact materials. Therefore, to avoid those issues, the formation of an epitaxial NiGe layer and control of its relative orientations are quite required.

In previous studies of metal silicide/Si contacts, an intermediate layer between metal and Si is often used to obtain or promote epitaxial silicide formation of the metal contact layer, e.g., epitaxial silicide formation from Pd/Ti/Si [14], Co/Ti(O)/Si [15], Co/TiN/Si [16], and Co/SiO<sub>x</sub>/Si [17] structures in the Si case. Among those intermediate layers, the oxide intermediate layer is expected to effectively control the epitaxial formation and its relative orientation of metal contact layer, because it does not depend on substrate orientation and doping level, and the preparation of the oxide layer is easy [17,18].

In this study, we investigated the epitaxial formation of NiGe layer on a Ge(110) substrate. The effect of the surface native oxide layer on the orientation of epitaxial NiGe domain grown on Ge(110) substrate has been investigated, and the epitaxial and polycrystalline growths with increase in the annealing temperature are further discussed. We also compared the morphology of the NiGe layer with different crystalline structures. Finally, the epitaxial formation of NiGe layer on Ge(110) has been discussed by considering the strain due to the misfit, and also considering the interfacial energy. Our results reveal that the orientation of the epitaxial NiGe layer on Ge(110) could be controlled by the native oxide layer, and the annealing temperature affects the crystalline properties of epitaxial and polycrystalline NiGe layers grown on the Ge(110) substrate.

## **3.2 Experiment**

The substrate used was an n-type Ge(110) wafer with a resistivity of 0.1-10  $\Omega$  cm. The Ge wafers were chemically cleaned by dipping in a diluted HF solution

and rinsing in deionized water repeatedly for five times to remove contaminations and the surface oxide layer. After wet cleaning, the Ge wafer was exposed to the atmosphere and immediately introduced into an ultra-high-vacuum (UHV) chamber whose base pressure was below  $2.5 \times 10^{-5}$  Pa. Note that a native oxide layer was formed during the introduction of the sample from the atmosphere to the UHV chamber. Thermal cleaning was performed at 550 °C for 30 min in the UHV chamber to remove the native oxide layer for some samples. Some samples were not treated with thermal cleaning to investigate the effect of the native oxide layer on the epitaxial formation of the NiGe layer. A 20- or 30-nm-thick Ni layer was deposited by e-beam evaporation at room temperature. Then, the samples were exposed to the atmosphere and annealed in a quartz furnace chamber at 200-550 °C for a time ranging from 30 s to 5 min in N<sub>2</sub> ambient.

Reflection high-energy electron diffraction (RHEED), with an electron energy of 28 keV, was used to confirm whether the native oxide layer was removed by thermal cleaning. Grazing angle X-ray diffraction (XRD;  $2\theta$  scan,  $\omega = 1.626^\circ$ ) and out-of-plane XRD ( $2\theta/\omega$  scan) using a Cu K $\alpha$  source ( $\lambda = 1.5405$  nm) were performed to observe the crystalline structure of Ni germanide layers. Cross-sectional transmission electron microscopy (XTEM) was also performed to reveal the crystalline structure of the germanide layer and the orientation relationship with respect to the Ge substrate. The surface roughness was measured by atomic force microscopy (AFM). The strain in the epitaxial NiGe layer was estimated by X-ray diffraction two-dimensional reciprocal space map (XRD-2DRSM).

### **3.3 Results and discussion**

#### **3.3.1 Effect of surface cleaning on crystalline structure of NiGe**

First, we investigated the effect of thermal cleaning on the surface condition of the Ge substrate before Ni deposition. For the samples without thermal cleaning, a native oxide layer, formed during the transfer of the chemically cleaned Ge(110) wafer from the atmosphere to the UHV chamber, exists between an as-deposited Ni layer and the Ge(110) substrate. The thickness of this native oxide layer was estimated to be 0.5 nm by X-ray photoemission spectroscopy

(XPS) measurement (*not shown*), which is consistent with the previously reported thickness of a native oxide layer (0.7 nm) on Ge under a similar condition [28].

For the samples with thermal cleaning at 550 °C for 30 min in a UHV chamber, the native oxide layer was completely removed, namely, there is no native oxide layer existing between the as-deposited Ni layer and the Ge(110) substrate. This was confirmed by RHEED observation of the Ge(110) surface along the  $[\bar{1}10]$  direction. Before thermal cleaning, owing to the existence of the native oxide layer, the long streak patterns related to the Ge(1×1) surface reconstruction are dim, as shown in Figure 3.1(a). Whereas, after thermal cleaning, the streaks become clear, and we can observe the appearance of a fourth-order pattern, as indicated by the arrows in Figure 3.1(b). Figure 3.1(c) shows the intensity profiles for the RHEED pattern, which are integrated from the dot rectangular. We can also see the appearance of the fourth-order pattern (as indicated by the arrows) and the increase in the intensities of RHEED patterns after thermal cleaning. These results indicate that the native oxide layer is effectively removed and a clean Ge(110) surface is prepared by thermal cleaning.

Figures 3.2(a) and 3.2(b) show grazing angle and out-of-plane XRD profiles, respectively, of a typical crystalline structure of NiGe layers for the Ni/Ge(110) samples with and without the native oxide layer after annealing at 350 °C for 30 s. In the grazing angle XRD profiles, as shown in Fig. 2(a), diffraction peaks identified to be NiGe111, 210, 112, 211, 103, 212, 013, 311, and 122 [11] are observed, and the intensities of these peaks are relatively weak compared with powder diffraction. This result indicates that the polycrystalline NiGe domain is formed in the Ni/Ge(110) samples with and without a native oxide layer.

On the other hand, in the out-of-plane XRD ( $2\theta/\omega$ -scan) as shown in Fig. 2(b), we can detect the diffractions related to a preferentially oriented NiGe layer parallel to the Ge(110) surface; these diffractions are identified to be NiGe102 and NiGe200 for the samples with and without the native oxide layer, respectively. These results suggest that the epitaxial NiGe domain has also been formed on the Ge(110) substrate regardless of the existence of native oxide layer, and the orientation of the epitaxial NiGe domain is affected by the native oxide layer.

Figures 3.3(a) - 3.3(d) show cross-sectional TEM images of NiGe layers grown on a Ge(110) substrate for the samples as mentioned in Figs. 3.2(a) and

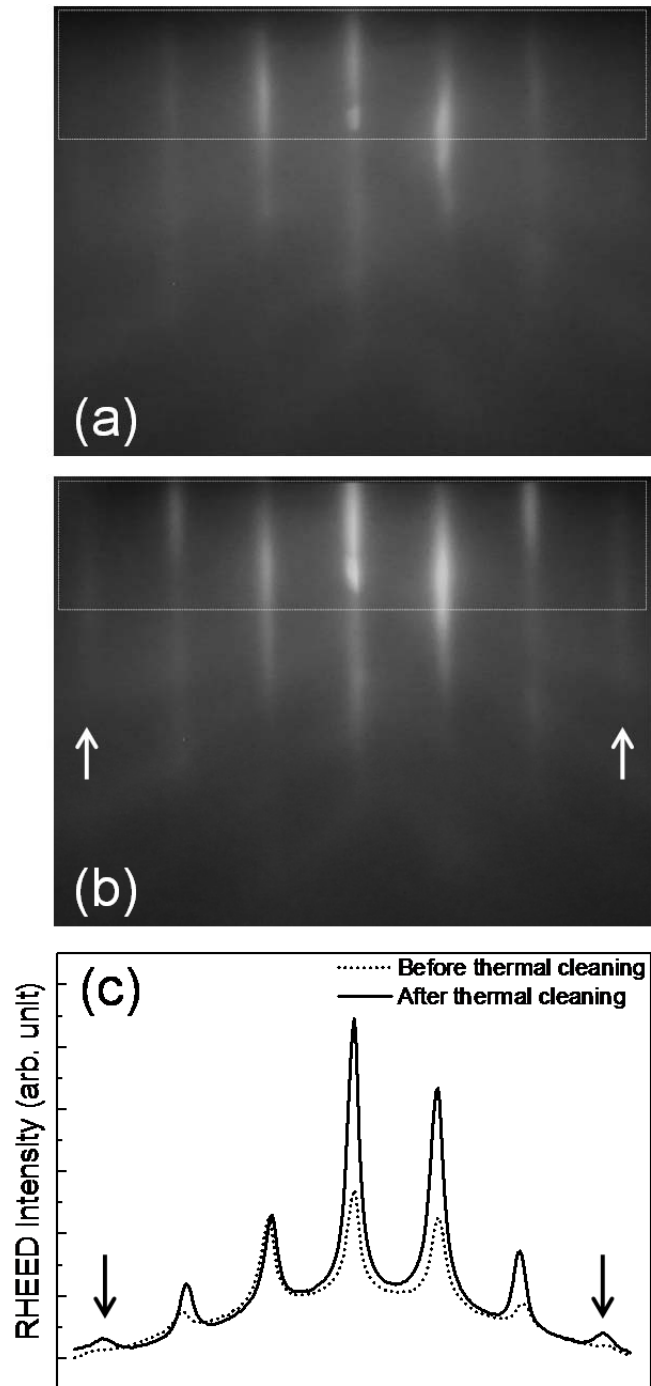


Figure 3.1 RHEED patterns of Ge(110) surface taken along  $[\bar{1}10]$  direction: (a) before thermal cleaning, (b) after thermal cleaning at 550 °C for 30 min, (c) integrated intensity of RHEED pattern from the dot rectangular in (a) and (b).

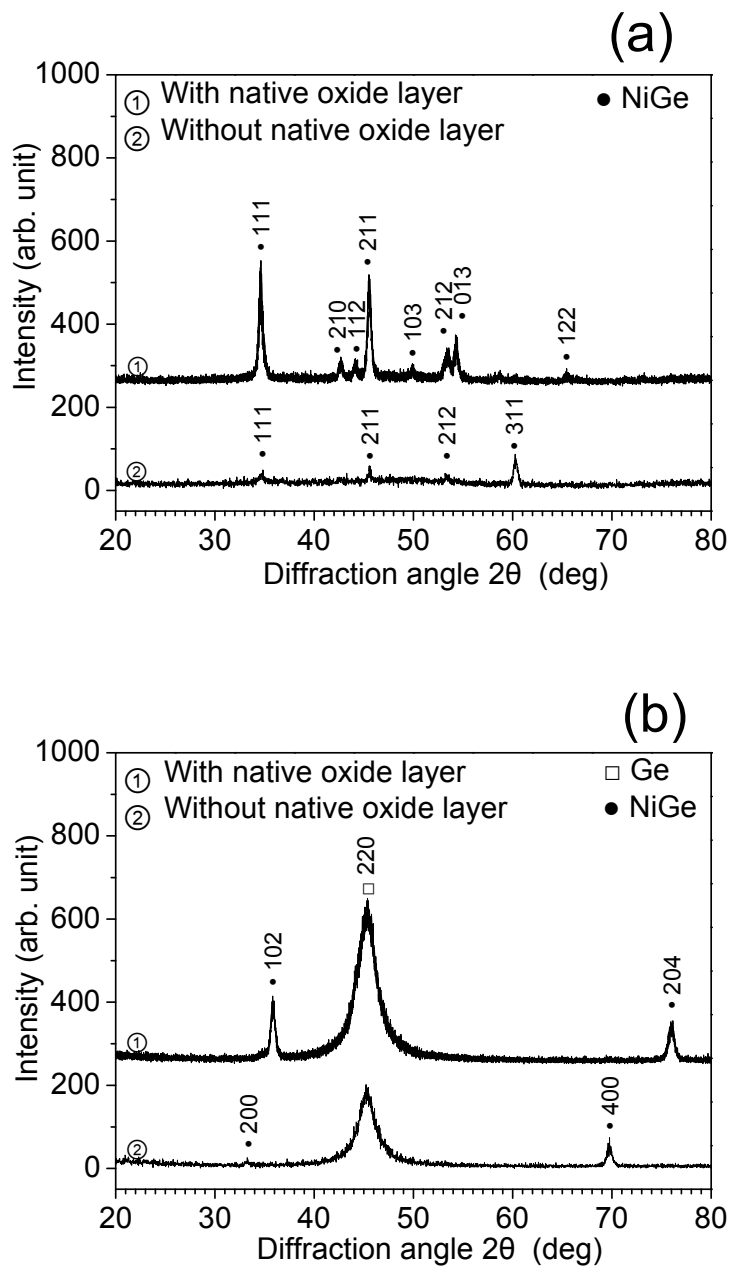


Figure 3.2 Typical XRD profile of 20-nm-thick Ni/Ge(110) system annealed at 350 °C for 30 s with and without a native oxide layer: (a) grazing angle XRD ( $2\theta$  scan,  $\omega = 1.626^\circ$ ), (b) out-of-plane XRD ( $2\theta/\omega$  scan).

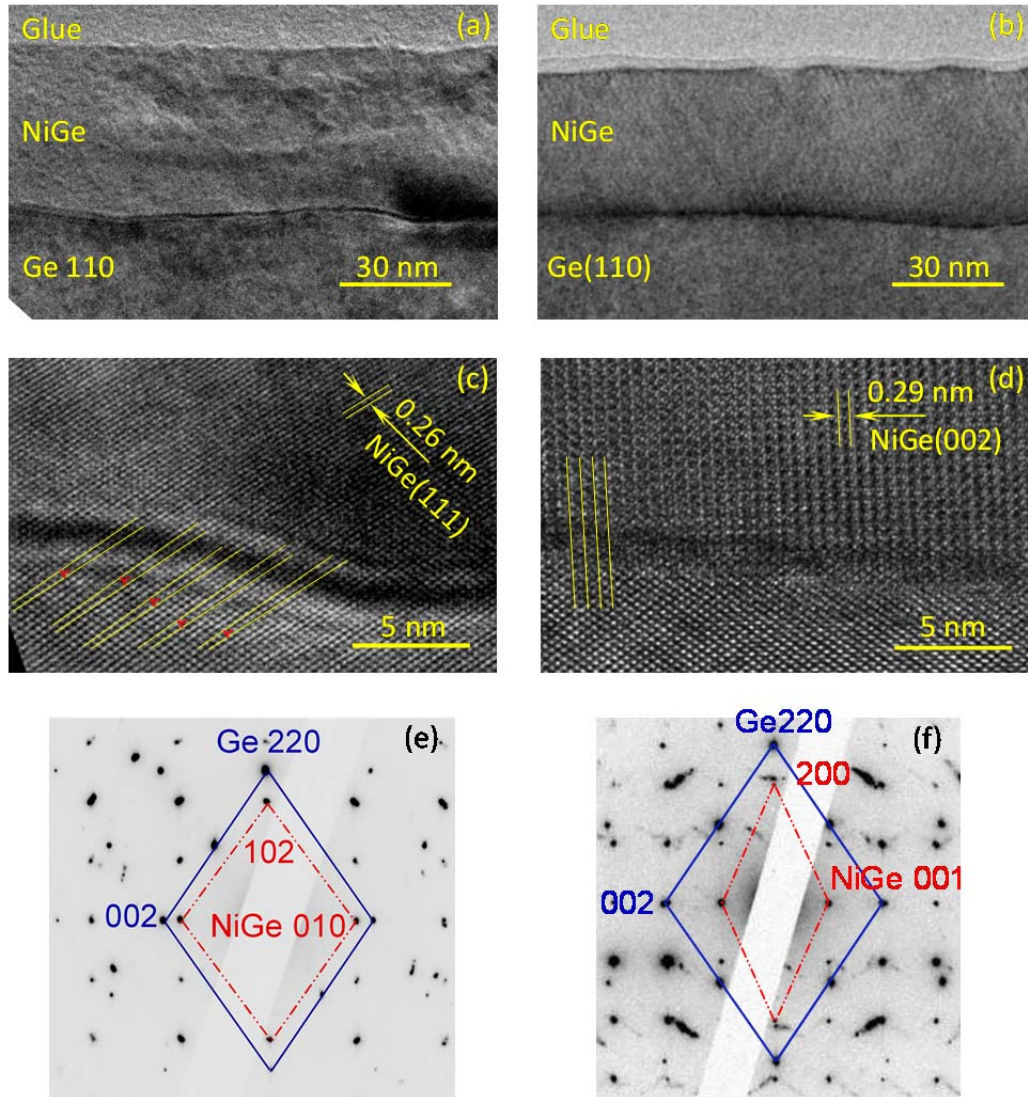


Figure 3.3 Cross-sectional morphology and crystalline structure of 20-nm-thick Ni/Ge(110) system annealed at 350 °C for 30 s: (a) and (b) cross-sectional TEM image, (c) and (d) high-resolution images, (e) and (f) TED pattern. (a), (c), and (e) correspond to the sample with a native oxide layer; (b), (d), and (f) correspond to the sample without a native oxide layer.

3.2(b); Figs. 3.3(a) and 3.3(c) correspond to the samples with a native oxide layer, and Figs. 3.3(b) and 3.3(d) correspond to those without a native oxide layer. For both samples with and without a native oxide layer, the interfaces between NiGe and the Ge(110) substrate are smooth. As shown in high-resolution TEM images, lattice spacings in NiGe layers are estimated to be 0.26 and 0.29 nm in Figs. 3.3(c) and 3.3(d), and those are identified to be lattice planes of NiGe(111) and (002), respectively. These well-resolved lattice planes extend throughout the entire NiGe layer, which reveals the high crystalline quality of the NiGe epitaxial layer. However, note that several misfit dislocations are observed for the sample with a native oxide layer, while the lattice planes of NiGe(002) nearly perfectly match with Ge(001) planes; nearly no misfit dislocations are visible for the sample without a native oxide layer. These differences in defects at the interface might lead to different electrical properties of the NiGe/Ge(110) contact [29, 30], which will be discussed in Chapter 5.

In TED patterns, as shown in Figs. 3.3(e) and 3.3(f), we can observe only a spot pattern, not a ring pattern for both samples with and without a native oxide layer. This result suggests that the epitaxial NiGe domain is dominant and the polycrystalline NiGe domain is minority, which is in agreement with the high resolution images. The orientation relationships between the NiGe layer and the Ge(110) substrate are deduced from these patterns; some diffraction spots are connected by lines to guide the eyes. For the sample with native oxide layer, the orientation relationships are NiGe(102)//Ge(110) and NiGe[010]//Ge[001], while those are NiGe(100)//Ge(110) and NiGe[001]//Ge[001] for the sample without a native oxide layer. These results are consistent with the previous result of out-of-plane XRD profiles.

### **3.3.2 The effect of annealing temperature on the epitaxial and polycrystalline growth of Ni germanide on Ge(110) substrate**

Figures 3.4(a) and 3.4(b) show the typical out-of-plane and grazing angle XRD profiles as a function of the annealing temperature for the Ni/Ge(110) samples without a native oxide layer. For samples annealed at high temperature above 250 °C, the diffraction peaks related to the NiGe layer in both out-of-plane and grazing angle XRD profiles are observed, and the corresponding intensities

are strong for the sample annealed at 350 °C, compared with those for the sample annealed at 250 °C. Whereas, for samples annealed at a low temperature of 200 – 250 °C, those NiGe peaks in both out-of-plane and grazing angle XRD are hardly observed, and the corresponding intensities are very weak.

Figures 3.5(a) and 3.5(b) show the typical out-of-plane and grazing angle XRD profiles as a function of the annealing temperature for the Ni/Ge samples with a native oxide layer. Unlike Ni/Ge(110) samples without a native oxide layer, when the Ni/Ge samples with a native oxide layer were annealed at a high temperature above 250 °C, the diffraction peaks related to NiGe are observed in grazing angle XRD profiles, while they are hardly observed in out-of-plane XRD profiles. On the other hand, when annealed at a low temperature below 250 °C, the diffraction peaks related to NiGe are hardly observed in grazing angle XRD profiles, but clearly observed in out-of-plane XRD.

To clearly show the variation of the intensity of diffraction peaks related to epitaxial and polycrystalline NiGe as a function of the annealing temperature, the intensities of diffraction peaks in out-of-plane and grazing angle XRD profiles are normalized by the intensity of Ge220 from the Ge substrate. The intensities of experimental results for polycrystalline domains are additionally divided by the relative intensity  $I(f)$  referenced from the powder diffraction profile [11]. Note that the intensity of diffraction peaks could not be used for quantity analysis of the volume of the relative crystalline structures, but the intensities qualitatively reflect the volumetric variation: the intensities of diffraction peaks NiGe102 and NiGe100 in out-of-plane XRD profiles represent the epitaxial domains for the samples with and without a native oxide layer, respectively, while those of NiGe111, 211, and 013 in grazing angle XRD profiles represent the polycrystalline domains. As shown in Figs. 3.6(a) and 3.6(b), the tendencies of intensities of NiGe111, 211 and 013 for the annealing temperature show good consistency.

At first, we discuss the crystalline structure of the Ni germanide layer for the sample without a native oxide layer, as shown in Fig. 3.6(a). In the case of low annealing temperature (200 – 220 °C), the growths of polycrystalline and epitaxial domains of the NiGe layer are restrained. With the increase in the annealing temperature, the polycrystalline and epitaxial domains of the NiGe phase grow

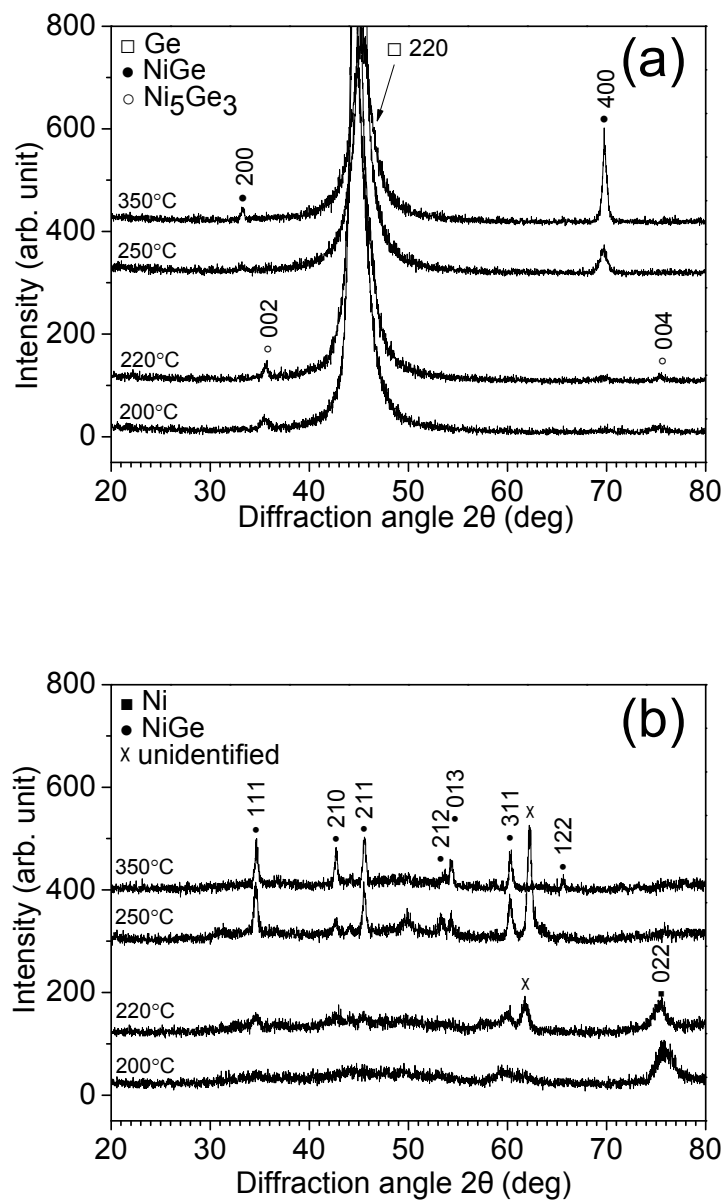


Figure 3.4 Crystalline structure of 30-nm-thick Ni/Ge(110) without a native oxide layer annealed at various temperatures for 5 min: (a) out-of-plane XRD ( $2\theta/\omega$  scan), (b) grazing angle XRD ( $2\theta$  scan,  $\omega = 1.626^\circ$ ).

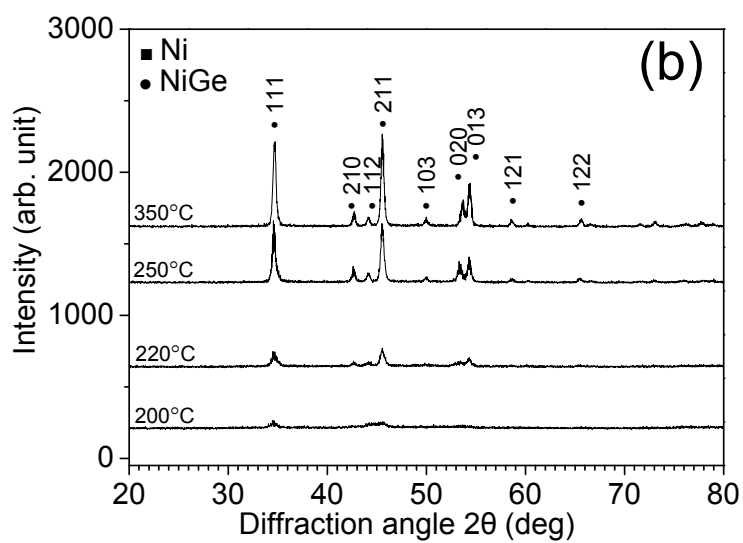
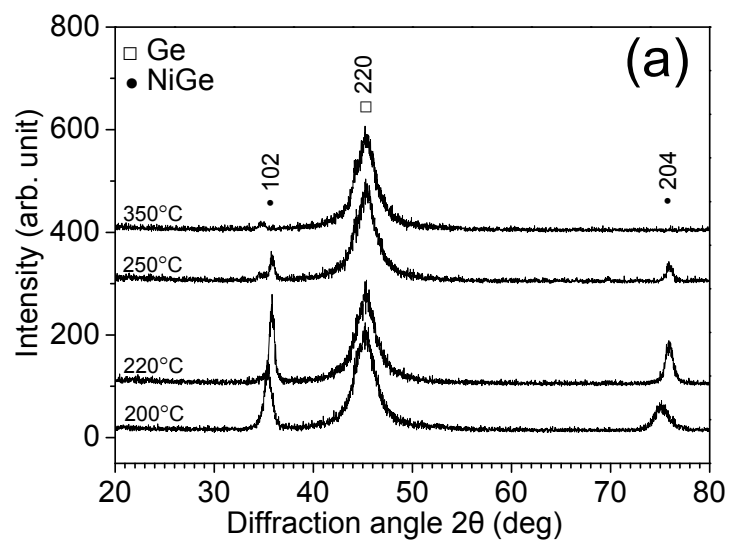


Figure 3.5 Crystalline structure of 30-nm-thick Ni/Ge(110) with a native oxide layer annealed at various temperatures for 5 min: (a) out-of-plane XRD ( $2\theta/\omega$  scan), (b) grazing angle XRD ( $2\theta$  scan,  $\omega = 1.626^\circ$ ).

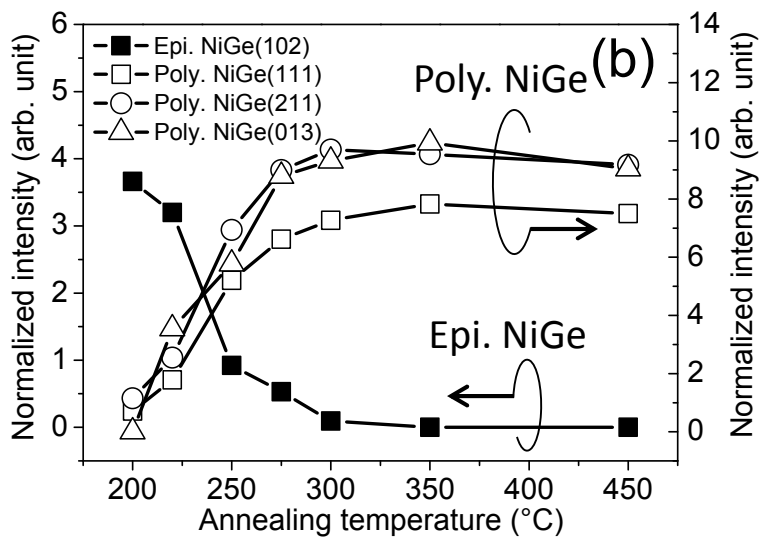
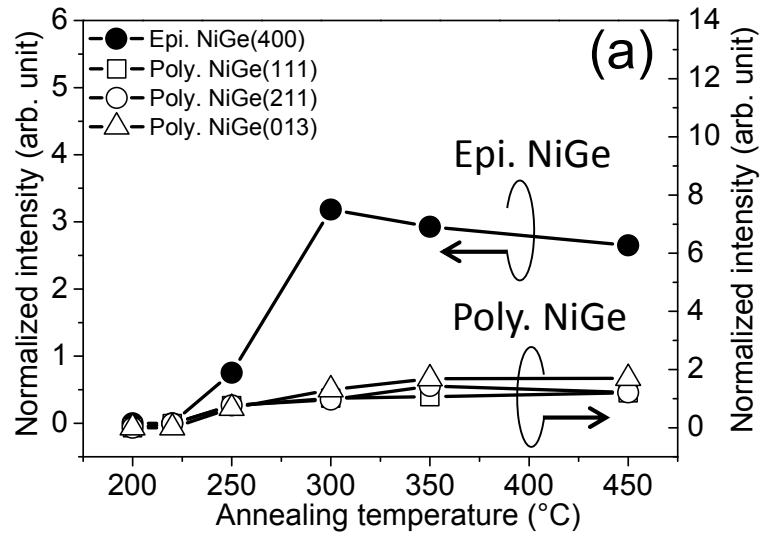


Figure 3.6 Normalized intensities of diffraction peaks from grazing angle XRD profiles and out-of-plane XRD profiles: (a) without a native oxide layer, (b) with a native oxide layer.

together and reach to maximum with annealing at 300 °C. When annealing above 300 °C, the intensities of polycrystalline and epitaxial NiGe domains remain constant, which means that the polycrystalline and epitaxial domains do not transform mutually, namely, both domains are thermally stable.

On the other hand, for the samples with a native oxide layer, as shown in Fig. 3.6(b), in the case of low annealing temperature (200 – 220 °C), the epitaxial NiGe growth is dominant, since the normalized intensity of epitaxial NiGe domains is very high compared with those of the polycrystalline NiGe domain. On the other hand, the polycrystalline growth becomes dominant at high annealing temperature, since the intensities of the polycrystalline NiGe domain increase, whereas the intensity of the epitaxial NiGe domain is nearly zero. These results indicate that a low annealing temperature favors the formation of epitaxial NiGe.

### **3.3.3 Morphology stability of Ni germanide layers**

Figures 3.7(a) - 3.7(h) show AFM images of Ni germanide surfaces for the samples with and without a native oxide layer after annealing at 220 - 550 °C. For the samples with a native oxide layer from low to high annealing temperature, the morphology of the Ni germanide surface changes from uniform to rugged topography, as shown in Figs. 3.7(a) - 3.7(c). The corresponding root-mean-square (RMS) roughness increases from 1.4 to 2.8 nm, as shown in Fig. 3.8. This result indicates that the surface of the NiGe layer keeps getting rough with the increase in the annealing temperature. We consider that the polycrystalline growth gives rise to this surface roughness degradation. As discussed previously with XRD results shown in Fig. 3.6(b), the growth of polycrystalline NiGe gradually becomes dominant with the increase in the annealing temperature, namely, the fraction of the polycrystalline NiGe domain increases, hence, the surface of the Ni germanide layer degrades, since a polycrystalline NiGe layer is generally rough compared with an epitaxial NiGe layer. When annealed at 550 °C, the surface becomes discontinuous as shown in Fig. 3.7(d), and the RMS value becomes extremely large so that it could not be shown in Fig. 3.8, which indicates that the agglomeration of the Ni germanide layer occurs.

For the sample without a native oxide layer annealed at the temperature

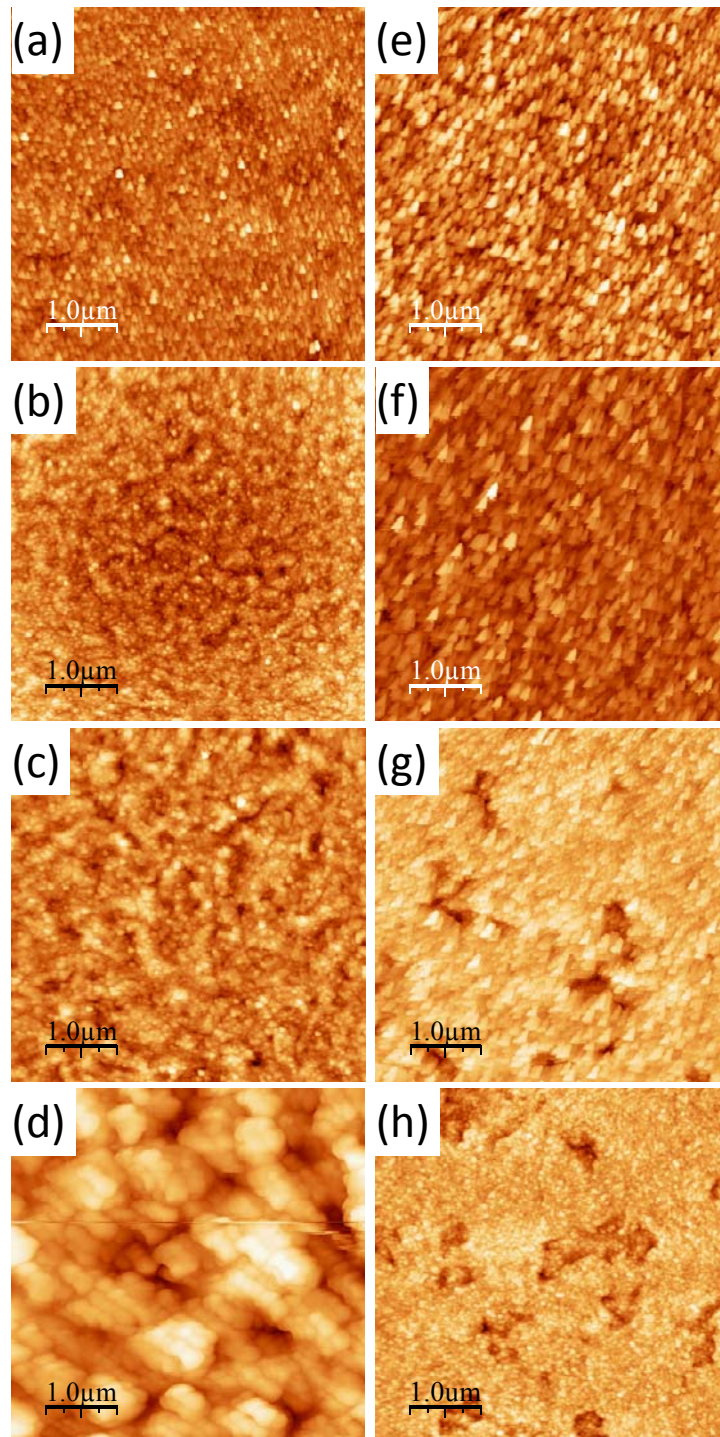


Figure 3.7 AFM images showing the evolution of surface morphology of Ni germanides with increasing annealing temperature. Samples with a native oxide layer: (a) 220, (b) 300, (c) 350, and (d) 550 °C. Samples without a native oxide layer: (e) 220, (f) 300, (g) 350, and (h) 450 °C.

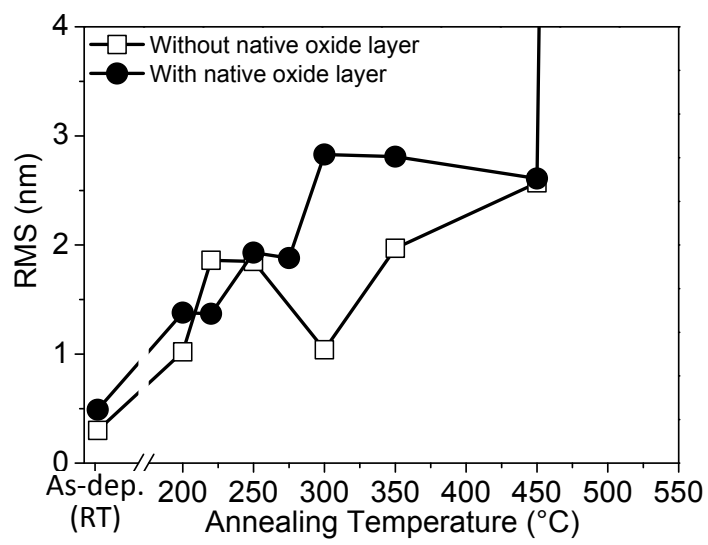


Figure 3.8 RMS values as a function of annealing temperature for samples with and without a native oxide layer.

ranging from 200 – 250 °C, the corresponding RMS values are nearly not different from those of the samples without a native oxide layer. When annealed at 300 °C, the surface becomes flat compared with the samples annealed at 220 and 250 °C, and the RMS value decreases from 1.9 to 1.0 nm. We consider that this improvement in the surface roughness is due to the formation of the epitaxial NiGe layer. As discussed previously in Fig. 3.6(a), the fraction of the epitaxial NiGe domain reaches to maximum, which contributes to the flat surface. When annealed at 350 and 450 °C, the RMS value increases again, and the AFM image shows that the layer structure of the Ni germanide becomes discontinuous, as indicated by the black region in Figs. 3.7(g) and 3.7(h). This result indicates that the agglomeration of Ni germanide layer occurs with annealing above 350 °C.

### **3.3.4 Crystalline quality of epitaxial NiGe(100)/Ge(110)**

Figure 3.9 shows the reciprocal lattice points of NiGe  $4\bar{1}0$  in X-ray diffraction two-dimensional reciprocal space map (XRD-2DRSM) for the samples annealed at 250 - 450 °C with thermal cleaning. The intensity of NiGe  $4\bar{1}0$  reciprocal lattice point for the sample annealing at low temperature (250 °C and 300 °C) is weak, compared with those of samples annealed at 350 - 450 °C. In addition, the intensities of those samples annealed at 350 - 450 °C hardly have difference. This result suggests that the epitaxial formation of NiGe layer have already started when annealing temperature is 250 °C, although the epitaxial formation is incomplete. And the annealing temperature 350 °C is high enough for completing the epitaxial formation.

On the other hand, the full width at half maximum (FWHM) of NiGe  $4\bar{1}0$  reciprocal lattice point is wide for the sample annealed at low temperature, particularly for the one annealed at 250 °C, as shown in Figure 3.9(a). Whereas, the NiGe  $4\bar{1}0$  reciprocal lattice point is concentrated when the annealing process is conducted at 350 - 450 °C, as shown in Figure 3.9(c) and 3.9(d). This evolution of NiGe  $4\bar{1}0$  reciprocal lattice point from scattering to concentrated with the increase of the annealing temperature is clearly shown by the variation of the FWHM in the projected intensity of XRD-2DRSM to omega axis, as shown in Figure 3.10. This result shows that epitaxial domains are not formed uniformly at a low temperature, the lattice of epitaxial domains are tilted with a small deviation

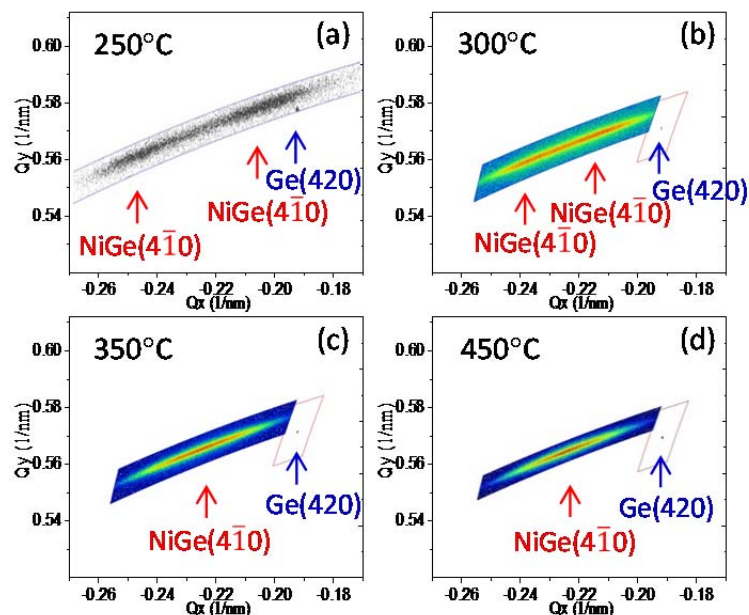


Figure 3.9 Reciprocal lattice points of NiGe( $4\bar{1}0$ ) of XRD-2DRSM for the NiGe/Ge samples annealed at (a) 250 °C, (b) 300 °C, (c) 350 °C, and (d) 450 °C.

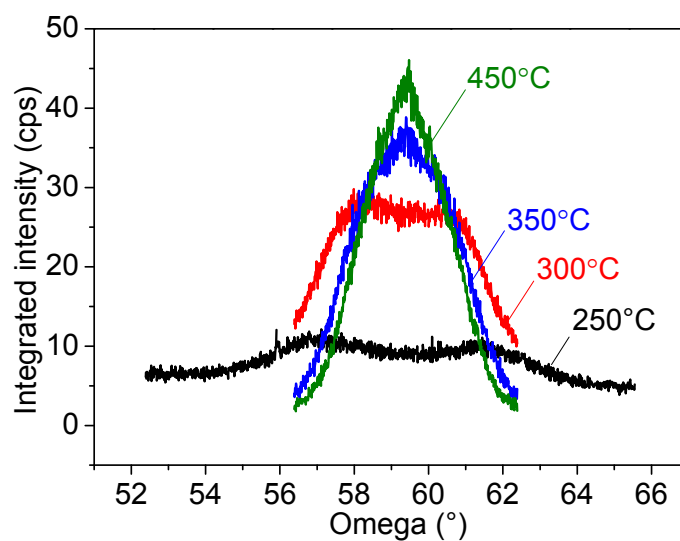


Figure 3.10 Projected intensity to omega axis, based on the XRD-2DRSM as shown in Figure 3.9.

angle, take the sample annealed at 250 °C for example, the deviation angle of the tilted epitaxial domains is estimated to be about  $\pm 2^\circ$ .

Next, we talk about the crystalline structures of epitaxial NiGe layer and Ge(110) substrate before discussion about the dependence of crystalline quality of epitaxial NiGe layer on the annealing temperature. As mentioned in section 3.3.1, for the sample with thermal cleaning, the orientation relationship between epitaxial NiGe layer and Ge(110) substrate is NiGe(100) // Ge(110), NiGe[001] // Ge[001] and NiGe[010] // Ge[ $\bar{1}10$ ], and the corresponding atomic arrangements of epitaxial NiGe(100) and Ge(110) substrate projected in the normal direction are found to be very similar, both of them have a hexagonal-like structure, as shown in Figure 3.11. This similarity in the crystalline structure is expected to contribute to a low surface energy, hence gives rise to the epitaxial formation of NiGe layer.

However, in terms of misfit strain (epitaxial NiGe suffered), the value is theoretically calculated to be -1.7% (compressive strain) in the direction NiGe[001] // Ge[001], whereas, that is as large as 17.6% (tensile) in the direction NiGe[010] // Ge[ $\bar{1}10$ ]. This large uniaxial misfit strain might lead to a stripped island growth, the stripped island has a long axis in the strain free direction NiGe[001] // Ge[001], while the short axis is along the large strain direction NiGe[010] // Ge[ $\bar{1}10$ ]. This stripped island growth is proven indirectly by a stripped surface topography, as shown in an AFM image (Figure 3.12(a)), the topography has a long axis along the direction NiGe[001], and a short axis along the direction NiGe(010), which is consistent with the misfit strain environment as discussed previously.

On the other hand, when the annealing temperature is low, the formed epitaxial layer is very thin, in this case, it is possible for stress relaxation through a tilting of the epitaxial domain in the direction NiGe[010], the tilting schematic diagram is shown in Figure 3.12(b), thus the diffraction profile of the NiGe  $4\bar{1}0$  reciprocal lattice point has a broad FWHM, as shown in Figure 3.12(c). When the annealing temperature is high, the atomic migration becomes much easier, which might contribute to a uniform epitaxial formation. Another reason for this uniform epitaxial formation might be that a relaxed epitaxial layer has already formed initially due to the large strain, then the subsequently epitaxial formation is completed on this relaxed epitaxial layer, thus a uniform epitaxial layer is formed.

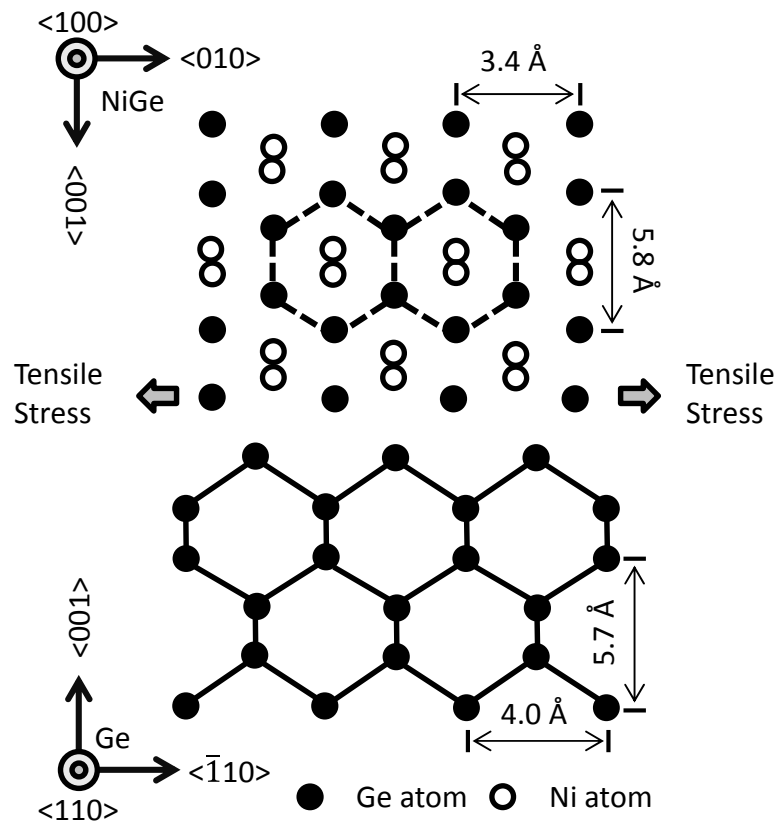


Figure 3.11 Atomic arrangement seen in projection down from the normal direction of the sample NiGe(100)//Ge(110), the upper one corresponds to NiGe, the lower one corresponds to Ge(110) substrate.

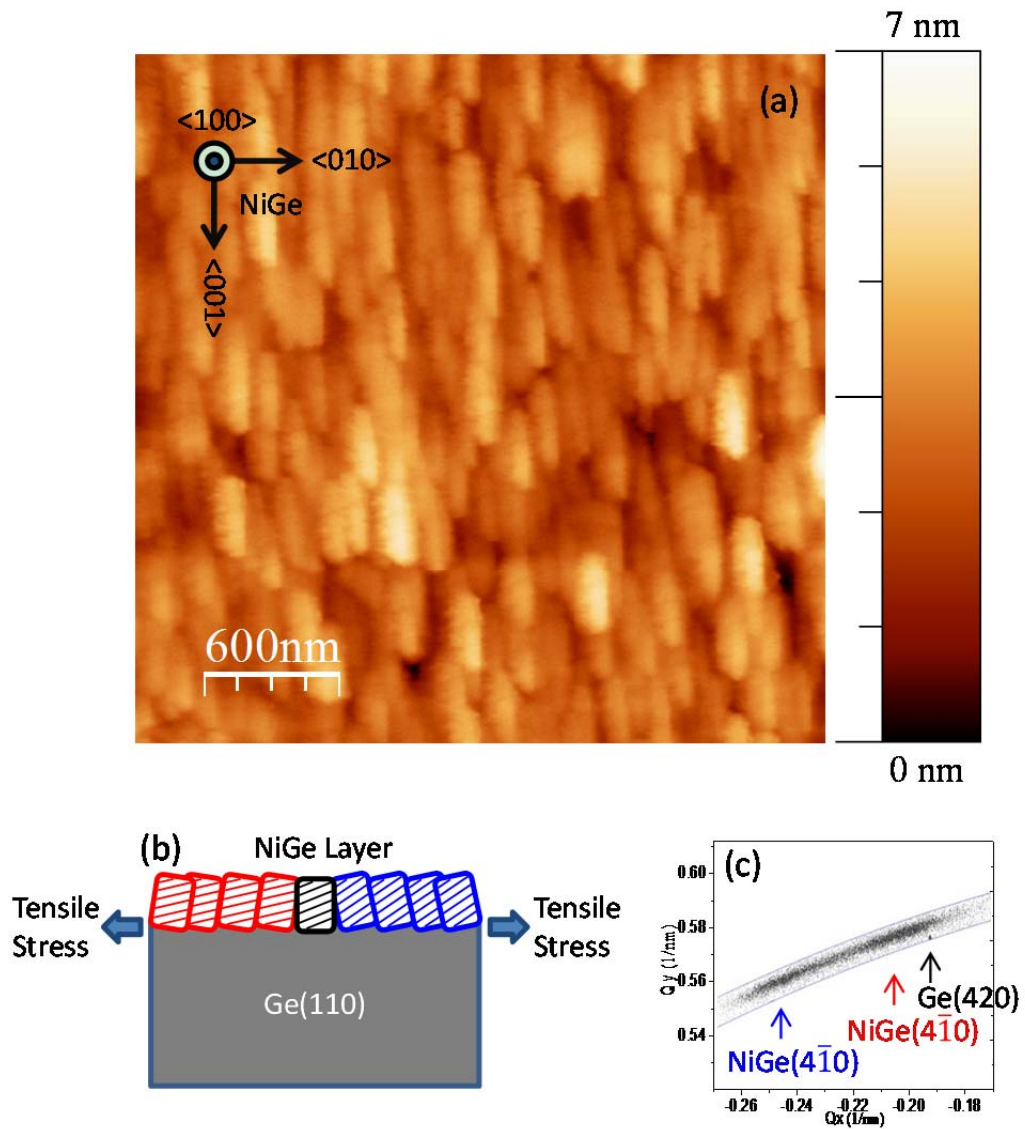


Figure 3.12 (a) AFM image with a striped topography aligning along NiGe[001] direction, the sample is annealed at 220 °C for 10 min. (b) Schematic diagram to show the tilting of epitaxial domains due to tensile strain in NiGe[010] direction. (c) XRD-2DRSM of NiGe 410 for the sample NiGe(100)//Ge(110) annealed at 250 °C.

### 3.4 Conclusions

We investigated the effect of thermal cleaning of the Ge surface before Ni deposition on the formation and crystalline structure of Ni germanide layers on Ge(110) substrate. The surface cleaning of the Ge substrate in a UHV chamber removes a very thin native oxide layer and provides a clean Ge surface. Although a partially epitaxial NiGe layer is formed on the Ge(110) substrate regardless of with and without a native oxide layer, the crystalline orientation relationships between epitaxial domains of Ni germanides and the Ge(110) substrate are strongly affected by the native oxide layer. For the samples with a native oxide layer, the orientation relationships are NiGe(102) // Ge(110) and NiGe[010] // Ge[001], while those are NiGe(100) // Ge(110) and NiGe[001] // Ge[001] for the samples without a native oxide layer. We also found that the growths of epitaxial and polycrystalline Ni germanides depend on the annealing temperature. For the samples without a native oxide layer, the growth of the epitaxial domain is coincident with that of the polycrystalline domain. The growths of polycrystalline and epitaxial domains are restrained at an annealing temperature lower than 250 °C, and they grow together at an annealing temperature higher than 300 °C. For the samples with a native oxide layer, a low annealing temperature of 200 °C favors the epitaxial growth, which is replaced by polycrystalline growth at a high annealing temperature of above 275 °C. Generally, compared with the samples with a native oxide layer, the samples without a native oxide layer present good surface roughness, but the thermal stability is poor. In addition, we also found the crystalline quality of epitaxial NiGe domain depends on the annealing temperature, when annealed at low temperature, epitaxial domains are not formed uniformly, the epitaxial domains are tilted with a small deviation angle, whereas, high temperature annealing could achieve a uniform epitaxial layer.

## References

- [1] T. Krishnamohan, D. Kim, T.V. Dinh, A.-T. Pham, B. Meinerzhagen, C. Jungemann, K. Saraswat, Electron Devices Meeting, 2008. IEDM 2008. IEEE International, IEEE, 2008, p. 1.
- [2] Y.F. Hsieh, L.J. Chen, Thin Solid Films **162**/1-2 (1988) 295.
- [3] K. Opsomer, D. Deduytsche, C. Detavernier, R.L. Van Meirhaeghe, A. Lauwers, K. Maex, C. Lavoie, Applied Physics Letters **90**/3 (2007) 031906.
- [4] S.L. Liew, B. Balakrisnan, C.S. Ho, O. Thomas, D.Z. Chi, Journal of The Electrochemical Society **154**/1 (2007) H9.
- [5] T. Nishimura, O. Nakatsuka, S. Akimoto, W. Takeuchi, S. Zaima, Microelectronic Engineering **88**/5 (2011) 605.
- [6] D. Han, Y. Wang, D. Tian, W. Wang, X. Liu, J. Kang, R. Han, Microelectronic Engineering **82**/2 (2005) 93.
- [7] K. De Keyser, R.L. Van Meirhaeghe, C. Detavernier, J. Jordan-Sweet, C. Lavoie, Journal of The Electrochemical Society **157**/4 (2010) H395.
- [8] K. Ikeda, T. Maeda, S.-i. Takagi, Thin Solid Films **508**/1–2 (2006) 359.
- [9] E. Simoen, K. Opsomer, C. Claeys, K. Maex, C. Detavernier, R.L. Van Meirhaeghe, S. Forment, P. Clauws, Applied Physics Letters **88**/18 (2006) 183506.
- [10] S. Gaudet, C. Detavernier, A.J. Kellock, P. Desjardins, C. Lavoie, Journal of Vacuum Science & Technology A: Vacuum, Surfaces, and Films **24**/3 (2006) 474.
- [11] H. Pfisterer, K. Schubert, Z. Metallkd **41** (1950) 358.
- [12] C. Perrin, D. Mangelinck, F. Nemouchi, J. Labar, C. Lavoie, C. Bergman, P. Gas, Materials Science and Engineering: B **154-155** (2008) 163.
- [13] M. Niranjana, L. Kleinman, A. Demkov, Physical Review B **75**/8 (2007) 085326.
- [14] R. Suryana, O. Nakatsuka, S. Zaima, Japanese Journal of Applied Physics **49** (2010) 05FA09.
- [15] F. Hong, G.A. Rozgonyi, B.K. Patnaik, Applied Physics Letters **64**/17 (1994) 2241.
- [16] M.L.A. Dass, D.B. Fraser, C.S. Wei, Applied Physics Letters **58**/12 (1991) 1308.
- [17] R.T. Tung, Applied Physics Letters **68**/24 (1996) 3461.

## **4 Epitaxial formation of Ni germanide on Ge(001) substrate by reactive deposition**

### **4.1 Background**

As the dimensional scaling of complementary metal-oxide-semiconductor (CMOS) devices shrinks deeper into nanometer order, the source/drain contact faces numerous new challenges besides controlling of the series resistance within tolerable limits [1]. One of the challenges is to control the crystalline structure of contact materials [2], including the homogeneity of crystalline structure and crystalline orientation. Because once contact dimension of nanometer technology devices scales down to a magnitude of grain size of contact materials, a variability of crystalline orientation of grains in metal contact materials may give rise to a unignorable variation of the work function [3] and morphology stability [4]. Particularly in the case that the contact material has strong anisotropic properties, the problem of electrical fluctuation and non-reproducibility for each source and drain regions will occur by using a polycrystalline material as contact layer. Therefore, the contact layer with polycrystalline structure may be not suitable for such nanometer technology electronic devices, and the formation of an epitaxial contact layer and control of its relative orientations are quite required.

Compared with the epitaxial formation of silicide on silicon substrate, the epitaxial formation of germanide on germanium (Ge) substrate is much more difficult, since there are few germanide materials with good lattice match with the diamond structure of Ge. In previous studies, reactive deposition method has been successfully conducted to form epitaxial cobalt [5] and nickel germanide [6] layers on Ge(001) in an ultrahigh vacuum (UHV) chamber equipped with *in-situ* transmission electron microscope (TEM), with which the nucleation, island growth, and coalescence of epitaxial germanide are clarified. However, these epitaxial formations observed with *in-situ* TEM cannot represent the general germanide formation on bulk Ge substrate, since the thickness of Ge(001) specimen for *in-situ* UHV-TEM is very thin so as to allow the electron beam penetrate through the Ge specimen, which would result in the difference of germanidation on this thin Ge specimen from that happened on bulk Ge substrate.

Moreover, this observation of epitaxial formation by TEM cannot represent the whole germanidation area due to the limitation of observation field of TEM.

Considering the requirement of nanoscale Ge MOS field effect transistor (MOSFET), nickel monogermanide (NiGe) is thought as one of the most promising contact materials because of its low resistivity (approximately  $22 \mu\Omega\cdot\text{cm}$ ), low formation temperature (as low as  $350 \text{ }^\circ\text{C}$ ), final stable phase in Ni-Ge binary alloy system, and low Ge consumption for germanide formation [7]. Previously, we found a NiGe epitaxial layer could be formed on Ge(110) substrate by solid phase reaction, but the crystalline structure of a NiGe layer formed on Ge(001) substrate is generally polycrystalline [8-10]. In this study, we adapt the reactive deposition method to form epitaxial NiGe on bulk Ge(001) substrate, the effect of thickness of reactive deposited NiGe layer on its epitaxial formation has been investigated, and the growth mechanism is also further discussed. In addition, we propose and demonstrate the 2-step deposition method to form a thick and uniform NiGe epitaxial layer on Ge(001) substrate.

## 4.2 Experiment

Substrate used was an n-type Ge(001) wafer with a resistivity of  $2.0 \Omega\cdot\text{cm}$ . A Ge substrate was cleaned by dipping in a diluted HF solution and rinsing in deionized water repeatedly for five times in order to remove contaminations and a surface oxide layer. After wet chemical cleaning, the Ge substrate was immediately introduced into an UHV chamber whose base pressure was below  $2.5\times 10^{-5}$  Pa. Thermal cleaning was performed at  $550 \text{ }^\circ\text{C}$  for 30 min in the UHV chamber to remove native oxide layer. A 5–20-nm-thick-Ni layer monitored with a thickness meter was reactively deposited using electron beam evaporation at a substrate temperature of  $350 \text{ }^\circ\text{C}$ .

We also prepared a sample with 2-steps of NiGe reactive deposition and Ni germanidation as follows in order to investigate the epitaxial growth mechanism. After the reactive deposition of a 5 nm-thick Ni layer at  $350 \text{ }^\circ\text{C}$ , a 15 nm-thick Ni layer was additionally deposited at room temperature, then, this sample was taken out in atmosphere and annealed at  $350 \text{ }^\circ\text{C}$  for 30 s in  $\text{N}_2$  ambient using rapid thermal annealing (RTA) system.

*In-situ* reflection high energy electron diffraction (RHEED) with an electron

energy of 26 keV was used to investigate the crystalline structure of reactive deposited Ni germanide. Grazing angle X-ray diffraction (XRD) ( $2\theta$  scan,  $\omega = 1.626^\circ$ ) and out-of-plane XRD ( $2\theta/\omega$  scan) using a Cu  $K\alpha$  source were further performed to confirm the crystalline structure of Ni germanide layers. The cross-sectional transmission electron microscopy (XTEM) and transmission electron diffraction (TED) were also performed to observe interfacial crystalline structure, and to clarify the orientation relationship of Ni germanide with respect to Ge substrate, respectively. The surface morphology and roughness were observed with atomic force microscopy (AFM).

### 4.3 Results and discussion

#### 4.3.1 Epitaxial formation of Ni germanide by reactive deposition

Figures 4.1(a) – 4.1(d) show the *in-situ* RHEED patterns associated with each process from chemical cleaning to reactive deposition. After transferring of chemical cleaned sample into a UHV chamber, the RHEED pattern is unclear, and only the first order streak pattern corresponding to Ge(110) plane is observed, as indicated by the solid arrow in Fig. 4.1(a). This unclear pattern is considered to be due to the formation of a native oxide layer on the surface of Ge(001) substrate during the transferring from atmosphere to UHV chamber [11, 12]. Fig. 4.1(b) shows the RHEED pattern after thermal cleaning at 550 °C for 30 min, the first order streak pattern from Ge(110) plane becomes obviously clear compared with that in Fig. 4.1(a), and the additional secondary order streak pattern appears, as indicated by dot arrow. This result means that a native oxide layer has been completely removed by thermal cleaning in UHV, the subsequent reactive deposition is conducted on a flat Ge(001) surface without any contamination.

Figure 4.1(c) shows the RHEED pattern after the reactive deposition of an 11-nm thick NiGe layer at 350 °C. This RHEED pattern also shows a typical streak pattern, although it is quite different from that of Ge(001) clean surface after thermal cleaning. The lattice constant estimated from the spacing of the streak pattern was about 0.286 nm, which is identified to be NiGe  $\bar{1}10$  reflection. This result suggests that an epitaxial NiGe layer is formed on Ge(001), and the growth mode is two-dimension growth.

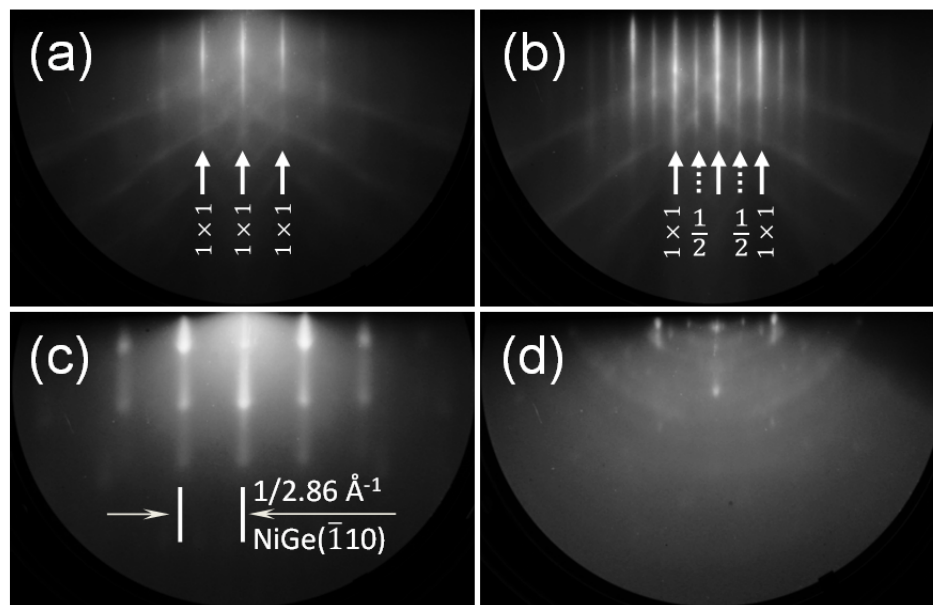


Figure 4.1 RHEED patterns correspond to various processes: (a) After the transferring of chemical cleaned sample from atmosphere to UHV chamber; (b) After thermal cleaning at 550 °C for 30min; (c) After 11 nm NiGe layer is formed by reactive deposition at 350 °C; (d) After 22 nm NiGe layer is formed by reactive deposition at 350 °C.

However, here, we have to emphasize two points. One is that this clear streak pattern is observed once the deposition shutter is opened, which indicates that an epitaxial NiGe layer is formed at 350 °C on Ge directly without any initial formation of Ni-rich germanides, such as Ni<sub>5</sub>Ge<sub>3</sub> [10, 13] and Ni<sub>2</sub>Ge [14, 15]. This direct formation of epitaxial NiGe without other transition phase is consistent with the previous investigation by *in-situ* UHV-TEM [6]. Another point is that the clear streak pattern disappears once the thickness of this NiGe layer reaches to 22 nm, spot and ring patterns appear simultaneously as shown in Fig. 4.1(d), which indicates that the surface become rough, the growth mode turns to three-dimension (3-D) growth, and polycrystalline domain grows with epitaxial domain together. This result reveals that the thickness of NiGe layer is a key factor to determine the formation model (epitaxial formation or polycrystalline formation), and the critical thickness for the transition from epitaxial to polycrystalline formation is about 22 nm.

Generally, grazing angle XRD is used to detect the polycrystalline structure of thin film, while out-of-plane XRD, which shows us the diffraction plane of film parallel to the surface of substrate, is used to detect the epitaxial growth. Figures 4.2(a) and 4.2(b) show the grazing angle XRD and out-of-plane XRD profiles, respectively, corresponding to the samples as mentioned previously. The crystalline structure of epitaxial NiGe is clarified besides the thickness dependence of epitaxial formation. As for the sample with an 11 nm-thick NiGe layer prepared with reactive deposition, no diffraction peak is observed except a diffraction peak related to Ge311 in the grazing angle XRD. However, in the out-of-plane XRD profile, we can observe a weak (because the film is as thin as 11nm) but visible diffraction peak at 34.57°, which is identified to be NiGe111, meaning a NiGe layer is epitaxially formed. This orientation relationship with Ge substrate is NiGe(111) // Ge(001), while Nath *et al* [6] reported that the orientation relationship was NiGe( $\bar{1}01$ ) // Ge(001) in an *in-situ* UHV-TEM study. We consider that this difference might be due to the condition of Ge substrate, the thickness of Ge(001) substrate in Nath's study is very thin, since the TEM observation requires that the specimen should be as thin as a few hundred nanometers [16]. On the other hand the thickness of Ge(001) substrate used in this study was as thick as 400 μm.

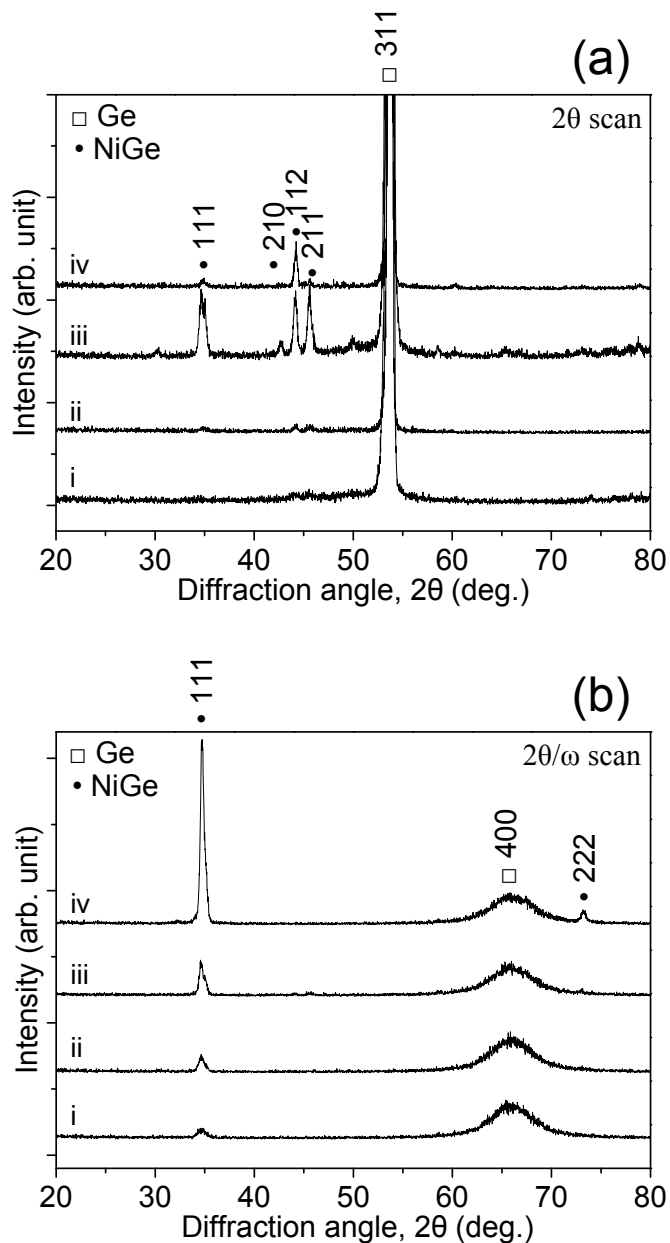


Figure 4.2 (a) Grazing angle XRD ( $2\theta$  scan,  $\omega = 1.626^\circ$ ), (b) Out-of-plane XRD ( $2\theta / \omega$  scan) for the samples after various treatments: i. After the formation of 11 nm NiGe layer by reactive deposition; ii. After the formation of 22 nm NiGe layer by reactive deposition; iii. After the formation of 45 nm NiGe layer by reactive deposition; iv. After the formation of 45 nm NiGe layer by 2-steps deposition combined with annealing by RTA.

### 4.3.2 Thickness dependence of epitaxial formation

For the sample prepared with the reactive deposition of a 45 nm-thick NiGe layer, various diffraction peaks corresponding to NiGe111, 210, 112, and 211 are observed in the grazing angle XRD, while the diffraction peak of NiGe111 is also observed in out-of-plane XRD, this result suggests the polycrystalline and epitaxial domain coexist. By comparison of the peak area of NiGe111 from the grazing angle XRD and out-of-plane XRD, we roughly expect that the amount of epitaxial domain is similar with that of polycrystalline domain (the normalized peak area of NiGe111 from grazing angle XRD is  $2.8 \times 10^3$ , while that from out-of-plane XRD is  $2.5 \times 10^3$ ).

The evolution of surface morphology with the thickness of reactive deposited NiGe layer from 11 nm to 45 nm was investigated with AFM observation. Figure 4.3(a) shows the AFM image of reactive deposited sample with an 11 nm-thick NiGe layer, a uniform island-like surface is observed, and the root mean square (RMS) roughness was estimated to be 1.8 nm. Figure 4.3(b) shows the AFM image of the reactive deposited sample with a 22 nm-thick NiGe layer, the islands also distribute uniformly on the surface, although the islands grow up which was characterized by the large lateral length and height compared with those of 11 nm-thick NiGe sample, as shown in the height profiles below the AFM images. Moreover, the RMS roughness also increases to 2.4 nm. Figure 4.3(c) shows the AFM image of the reactive deposited sample with a 45 nm-thick NiGe layer, the corresponding RMS roughness was estimated to be as large as 10.9 nm, and two distinctive morphologies are simultaneously observed on the surface, one is chrysanthemum-like topography, and another is flat topography which has a clear boundary with chrysanthemum-like topography, as marked with solid border line. We consider those two distinctive morphologies are contributed by polycrystalline and epitaxial domains, the chrysanthemum-like topography corresponds to polycrystalline domain, while the flat localized topography is related to the epitaxial domain, because epitaxial layer is generally known to be flat compared with polycrystalline layer.

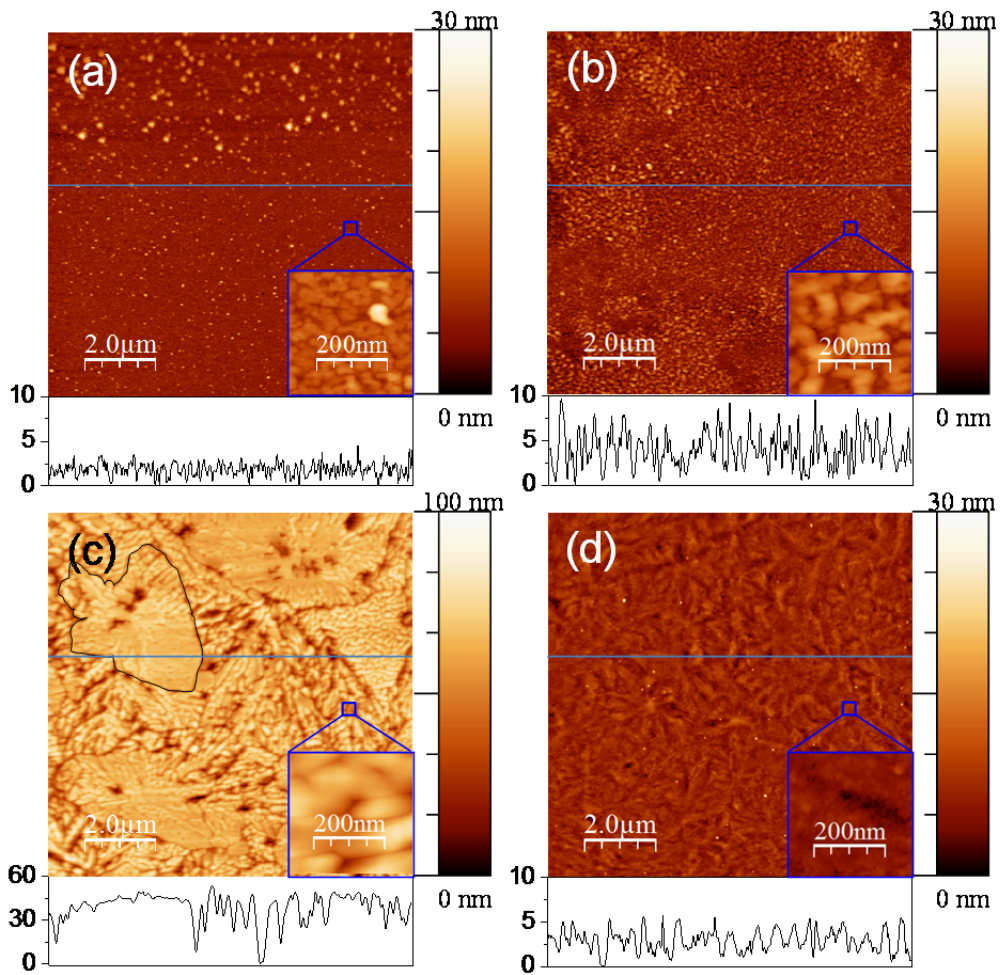


Figure 4.3 AFM images correspond to various processes: (a) After the formation of 11 nm NiGe layer by reactive deposition; (b) After the formation of 11 nm NiGe layer by 2-steps deposition combined with annealing by RTA; (c) After the formation of 22 nm NiGe layer by reactive deposition; (d) After the formation of 45 nm NiGe layer by reactive deposition; (e) After the formation of 45 nm NiGe layer by 2-steps deposition combined with annealing by RTA.

### 4.3.3 Improvement of epitaxial formation by 2-steps deposition

Next, we demonstrate a way to avoid polycrystalline NiGe growth even when the thickness of reactive deposited Ni is over the critical thickness. A 15 nm-Ni layer was subsequently deposited at room temperature after the formation of an 11 nm-thick epitaxial NiGe layer by reactive deposition method. We name this sample as *2-steps deposition sample*. Then, a thermal annealing at 350 °C for 30 s in N<sub>2</sub> ambient was performed for germanidation by RTA. The out-of-plane XRD, AFM, and TEM observation were used to confirm a complete formation of an epitaxial NiGe layer.

As shown in Fig. 4.2(b) and Fig. 4.3(d) respectively, a strong diffraction peak related to NiGe111 and a flat surface (RMS is 1.4 nm) are observed for the 2-steps deposition sample after annealing, compared to the reactive deposited sample with a 45 nm-thick NiGe layer. This result indicates that an epitaxial NiGe layer with high quality is formed, which is further confirmed by TEM observation. Figure 4.4(a) shows the XTEM image of the 2-steps deposited sample after thermal annealing, a single layer with smooth interface for a wide area is observed. In the high resolution TEM image, as shown in Fig. 4.4(b), the lattice spacing in NiGe layer is estimated to be 0.26 nm, which is identified to be the lattice planes of NiGe111. This well-resolved lattice plane extends throughout the entire NiGe layer, which reveals that the high crystalline quality of the NiGe epitaxial layer was achieved by 2-steps deposition combined with solid phase reaction. Figure 4.4(c) shows the TED pattern of this sample. Only the spot pattern is observed, and no ring pattern associated with polycrystalline structure is observed. And the orientation relationships between epitaxial NiGe and Ge(001) substrate, deduced from these patterns, is NiGe(111) // Ge(001) and NiGe[0 $\bar{1}$ 1] // Ge[1 $\bar{1}$ 0].

### 4.3.4 Discussion about the epitaxial formation mechanism

Before the discussion about the promotion of epitaxial formation by 2-steps deposition, we discuss about the Ni germanide formation with reactive deposition firstly. As mentioned previously, an epitaxial NiGe layer is formed directly on Ge(001) by reactive deposition method, before which no Ni-rich germanide is formed. This result suggests that the dominant diffusion species are Ge atoms

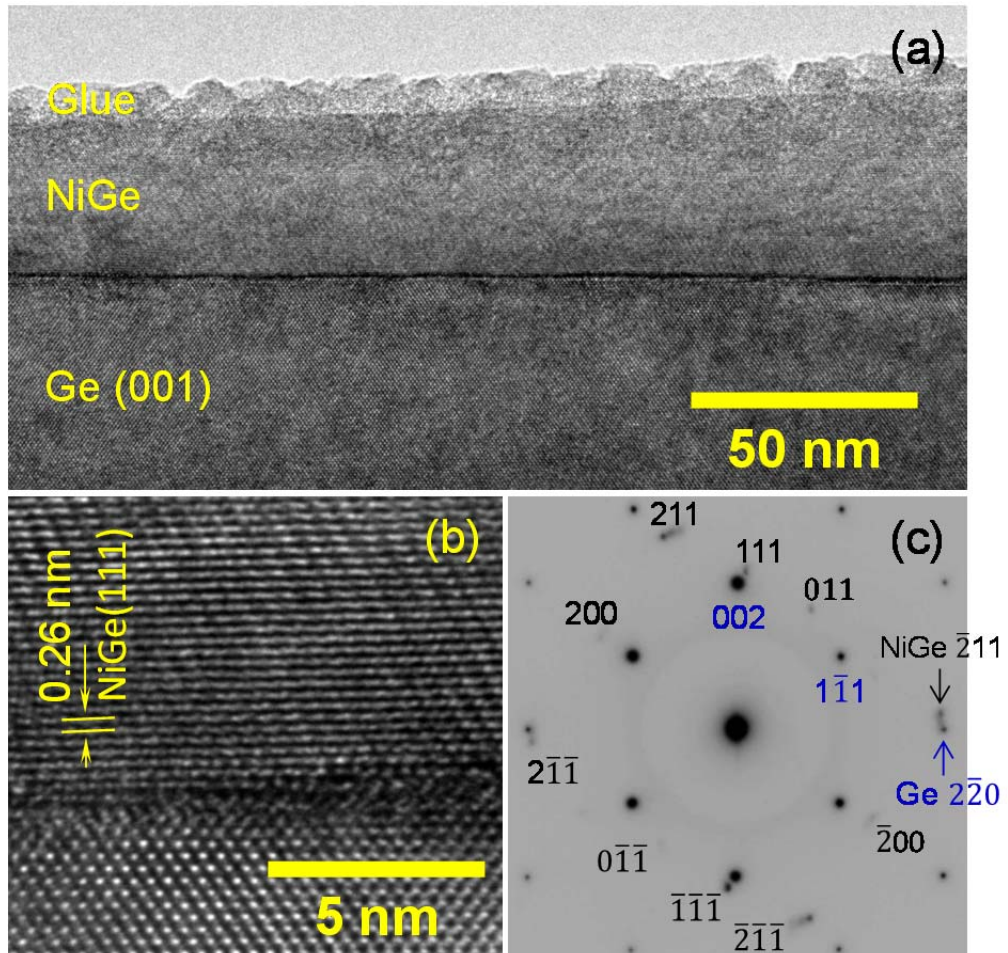


Figure 4.4 Cross-sectional morphology and crystalline structure of the 2-steps deposited sample after annealing at 350 °C for 30s by RTA: (a) cross-sectional TEM image, (b) high-resolution image, (c) TED pattern.

during the reactive deposition, because generally the first phase is known to be Ni-rich germanide if Ni atoms are the dominant diffusion species [17-19]. Moreover, the transition of *in-situ* RHEED pattern from typical streak pattern to a mixture pattern of ring and spot also support this conclusion indirectly. Assuming the dominate diffusion species are Ni atoms, the crystallization front should be at the interface between NiGe and Ge substrate, rather than at the surface. It means that the *in-situ* RHEED pattern should have kept exhibiting the characterization of the surface either the previously formed epitaxial NiGe layer or the residual Ni layer, in other words, RHEED pattern should not have changed even though the polycrystalline is formed at the NiGe/Ge interface, since the formed polycrystalline is located beneath the initially formed epitaxial NiGe layer under this assumption.

As for the thickness limitation of epitaxial formation, the misfit strain and 3-D growth mode should take the responsibility. As mentioned in the TED pattern, the misfit of the lattice spacings of NiGe[ $\bar{1}01$ ] and Ge[ $0\bar{1}0$ ] is as large as 7%, it makes sense that the strain increases with the growth of epitaxial layer, once the thickness reaches to a certain value, the strain in the epitaxial layer becomes so large that strain relaxation will occur, which may induce the polycrystalline growth. On the other hand, the 3-D growth mode might cause a rugged surface. The lower-lying area in this rugged surface might be the origin of the polycrystalline nucleation.

As for the case of 2-steps deposition, the dominant diffusion species are Ge atoms during the reactive deposition, as mentioned before. In contrast, the dominant diffusion species turn to Ni atoms during the thermal annealing of 2-steps deposition sample, because a large amount of Ni atoms are already deposited on the epitaxial NiGe template layer before annealing. That has been confirmed in general solid-phase reaction of Ni/Ge system [18]. And the pre-formed epitaxial NiGe plays a role of single crystal seed to induce the epitaxial formation, hence polycrystalline growth is effectively suppressed.

#### **4.4 Conclusions**

We have investigated the crystalline structure of an epitaxial NiGe layer on Ge(001) substrate prepared by reactive deposition method. The corresponding

orientation relationship with Ge(001) substrate is NiGe(111) // Ge(001) and NiGe[0 $\bar{1}$ 1] // Ge[110]. We found the thickness of NiGe layer prepared in the reactive deposition method is a key factor to form epitaxial germanide layer, once the thickness of epitaxial NiGe layer reaches to as thick as 22 nm, the polycrystalline NiGe formation would occur. We proposed a 2-steps deposition method combined with solid phase reaction in order to suppress the polycrystalline formation, and a 45 nm-thick epitaxial NiGe layer on Ge(001) substrate with atomically flat interface and uniformity was successfully achieved. Furthermore, the evolution of *in-situ* RHEED pattern from the streak to ring pattern reveals the crystallization front during the reactive deposition is on the surface of NiGe layer, in other words, the dominant diffusion species are Ge atoms during the reactive deposition, while the promotion of epitaxial formation by 2-steps deposition with post annealing gives an evidence that the crystallization front is at the interface between epitaxial NiGe and Ge(001) substrate, thus the dominant diffusion species are Ni atoms for the solid phase reaction. 2-steps deposition method realizes the high quality epitaxial NiGe/Ge(001) contact with atomically flat and uniform interface, and that promises suppressing the variability of electronic properties in nanoscale contacts in Ge nanoelectronic integrated devices.

## References

- [1] <http://www.itrs.net/Links/2013ITRS/2013Chapters/2013Overview.pdf>.
- [2] O. Nakatsuka, A. Suzuki, S. Akimoto, A. Sakai, M. Ogawa, S. Zaima, *Japanese Journal of Applied Physics* **47** (2008) 2402.
- [3] M. Niranjana, L. Kleinman, A. Demkov, *Physical Review B* **75**/8 (2007) 085326.
- [4] D. Deduytsche, C. Detavernier, R. Van Meirhaeghe, J. Jordan-Sweet, C. Lavoie, *Journal of Applied Physics* **101** (2007) 044508.
- [5] H.P. Sun, Y.B. Chen, X.Q. Pan, D.Z. Chi, R. Nath, Y.L. Foo, *Applied Physics Letters* **86**/7 (2005) 071904.
- [6] R. Nath, C.W. Soo, C.B. Boothroyd, M. Yeadon, D.Z. Chi, H.P. Sun, Y.B. Chen, X.Q. Pan, Y.L. Foo, *Applied Physics Letters* **86**/20 (2005) 201908.
- [7] S. Gaudet, C. Detavernier, A.J. Kellock, P. Desjardins, C. Lavoie, *Journal of Vacuum Science & Technology A: Vacuum, Surfaces, and Films* **24**/3 (2006) 474.
- [8] S. Gaudet, C. Detavernier, C. Lavoie, P. Desjardins, *Journal of Applied Physics* **100**/3 (2006) 034306.
- [9] B. Balakrishnan, C.C. Tan, S.L. Liew, P.C. Lim, G.K.L. Goh, Y.L. Foo, D.Z. Chi, *Applied Physics Letters* **87**/24 (2005) 241922.
- [10] Y. Deng, O. Nakatsuka, J. Yokoi, N. Taoka, S. Zaima, *Thin Solid Films* **557** (2014) 84.
- [11] Y. Deng, O. Nakatsuka, N. Taoka, S. Zaima, *Japanese Journal of Applied Physics* **53**/5S2 (2014) 05GA06.
- [12] S.K. Sahari, H. Murakami, T. Fujioka, T. Bando, A. Ohta, K. Makihara, S. Higashi, S. Miyazaki, *Japanese Journal of Applied Physics* **50**/4 (2011) 04DA12.
- [13] F. Nemouchi, D. Mangelinck, C. Bergman, G. Clugnet, P. Gas, J.L. Lábár, *Applied Physics Letters* **89**/13 (2006) 131920.
- [14] Y.F. Hsieh, L.J. Chen, E.D. Marshall, S.S. Lau, *Thin Solid Films* **162** (1988) 287.
- [15] J. Li, Q. Hong, J. Mayer, L. Rathbun, *Journal of Applied Physics* **67**/5 (1990) 2506.
- [16] D.B. Williams, C.B. Carter, *Transmission Electron Microscopy*, Springer, 2009, p. 3.
- [17] R. Thompson, K. Tu, J. Angillelo, S. Delage, S. Iyer, *Journal of The Electrochemical Society* **135**/12 (1988) 3161.
- [18] S.-L. Zhang, *Microelectronic Engineering* **70**/2 (2003) 174.
- [19] C. Yan, J.M. Higgins, M.S. Faber, P.S. Lee, S. Jin, *ACS nano* **5**/6 (2011) 5006.

## 5 Electrical properties of NiGe/Ge contacts

### 5.1 Background

Owing to its high mobilities for both electron and hole [1, 2], germanium (Ge) is expected as one of the promising channel materials to replace silicon (Si) in complementary metal-oxide-semiconductor (COMS) devices. However, parasitic resistance is one of the critical issues for the application of Ge COMS, since it degrades the drive current and increases the power consumption especially when the scaling technology proceeds deeper [3, 4]. The main parasitic resistance component is contact resistance at the metal/heavily doped Source/Drain interface [3, 5, 6], which is exponentially proportional to Schottky barrier height (SBH). Thus, controlling SBH is indispensable to reduce the contact resistivity for developing high performance Ge COMS.

Since strong Fermi level pinning (FLP) occurs at the charge neutrality level, which is close to the valence band edge in the case of Ge [7], the rectifying characteristics, rather than Ohmic characteristics, are always experimentally observed for a variety of metals or metallic/n-type Ge contact, the corresponding SBH are estimated to be very high [8], and are hardly controlled by the metal work function.

Although a large amount of reports discussed the origin of FLP, the detail has not yet been clarified. Nishimura *et al.* [9] attributed this strong FLP to metal-induced gap states (MIGS) at metal/Ge interface, which is formed by the penetration of the free electron wave function from metal to substrate. This MIGS theory is indirectly supported by the fact that the FLP could be effectively alleviated by inserting an ultra-thin interlayer between metal and Ge substrate, e.g., Al<sub>2</sub>O<sub>3</sub> [10], Ge<sub>3</sub>N<sub>4</sub> [11], or SiN [12]. Such intrinsic contribution to FLP suggests that the pinning level is hardly modulated by annealing in forming gas, forming metal-germanide/Ge interfaces, or changing the substrate orientation.

However, our group [13] found the SBH of Mn germanide/n-type Ge(111) contact with epitaxial structure is as much as 0.26 eV lower than that of Mn germanide/Ge(001) contact with polycrystalline structure. Moreover, Yamane *et al.* [14] examined that the FLP is apparently modified by the atomically controlled epitaxial Fe<sub>3</sub>Si/Ge(111) interfaces compared with the disordered interfaces. These

results could not be explained only by MIGS theory, but we can tentatively regard these alleviations of FLP as a consequence of the reduction of the density of interface states such as dangling bonds or disorders.

Previously, we proposed some effective methods to control the crystalline structures of NiGe layers on Ge substrate (for detail, recommend to refer to Chapter 3 and 4). The solid phase reaction contributes to the epitaxial formation of NiGe on Ge(110) substrate, while polycrystalline formation on Ge(001) substrate [15]. On the contrary, the reactive deposition leads to an epitaxial formation of NiGe on Ge(001) substrate, while the polycrystalline formation on Ge(110) substrate. In this study, we investigated the electrical properties of various NiGe/n-type Ge contacts with different crystalline structures. By considering interface states at the NiGe/Ge interface, the effect of extrinsic factors such as dangling bonds and disorder on the FLP has been discussed. And our results give us a hint that it can realize further low SBH for n-type Ge if a completely atomic matching is obtained.

## 5.2 Experiment

The substrates used are n-type Ge(110) and Ge(001) with donor concentrations of  $3.5 - 6.0 \times 10^{16}$  and  $3.5 - 6.0 \times 10^{14} \text{ cm}^{-3}$ , respectively. The Ge wafers were cleaned by dipping in a diluted HF solution and rinsing in deionized water repeatedly for five times in order to remove contaminations and a surface oxide layer.

After wet cleaning, the Ge wafer was exposed to the atmosphere and immediately introduced into an ultra-high-vacuum (UHV) chamber whose base pressure was below  $2.5 \times 10^{-5}$  Pa. Note that a native oxide layer was formed during the introduction of the sample from the atmosphere to the UHV chamber. Thermal cleaning was performed at 550 °C for 30 min in the UHV chamber to remove the native oxide layer for some samples. Some samples were not treated with thermal cleaning. A 20-nm-thick Ni layer was deposited by e-beam evaporation at room temperature. Then, the samples were exposed to the atmosphere and annealed in a furnace chamber at 350 °C for 30 s in N<sub>2</sub> ambient for germanidation. In this solid phase reaction method, an epitaxial NiGe layer with the orientation relationship of NiGe(100) // Ge(110) and NiGe[001] // Ge[001] was obtained for the sample with

thermal cleaning. While, for the sample without thermal cleaning, another epitaxial NiGe layer with different orientation relationship was obtained, the orientation relationship of this epitaxial NiGe layer is NiGe(102) // Ge(110), NiGe[010] // Ge[001]. In addition, the polycrystalline formation happened for the Ni/Ge(001) system regardless of the thermal cleaning process.

In terms of the reactive deposition method, a 5 – 20-nm-thick-Ni layer was reactively deposited at 350 °C after the wet cleaning and thermal cleaning, same as those processes in solid phase reaction method. In this method, a polycrystalline NiGe on Ge(110) substrate was prepared. On the other hand, an epitaxial NiGe layer on Ge(001) substrate, with the orientation relationship of NiGe(111) // Ge(001) and NiGe[0  $\bar{1}$  1] // Ge[11 0], was prepared with a combination method (2-steps deposition + solid phase reaction). The detail is as follows: After the reactive deposition of a 5 nm-thick Ni layer at 350 °C on Ge(001) substrate, a 15 nm-thick Ni layer was additionally deposited at room temperature, then, this sample was taken out in atmosphere and annealed at 350 °C for 30 s in N<sub>2</sub> ambient using rapid thermal annealing (RTA) system.

To fabricate a Schottky diode, after the formation of NiGe layer on Ge substrate, a top Al electrode was deposited in a conventional vacuum chamber by resistance heating method, then the contact patterns with various diameters ( $\phi$ 1000 – 100  $\mu$ m) were formed by a photolithography process and an etching process. Finally, a backside Al electrode was formed same as the top electrode. Electrical properties were investigated by current density-voltage characteristics ( $J$ - $V$ ) and capacitance-voltage characteristics ( $C$ - $V$ ).

## 5.3 Results and discussion

### 5.3.1 Evaluation of the edge leakage current

Before the discussion about the effect of crystalline structure of NiGe layer on the electrical properties of NiGe/Ge contacts, we firstly talk about two general components of the current flowing across the contact pattern, one is contact area current, the other one is edge leakage current, because the accuracy of SBH estimation with  $J$ - $V$  method is directly associated with those two currents.

To evaluate the edge leakage current,  $J$ - $V$  characteristics of epitaxial

NiGe(111)/n-type Ge(001) contacts with various contact pattern dimensions were measured. One typical  $J$ - $V$  characteristic (pattern dimension is  $\phi 1000 \mu\text{m}$ ), measured at measurement temperatures of 235 - 300K, is shown in Figure 5.1(a). This  $J$ - $V$  characteristic exhibits a rectifying characteristic. And the corresponding saturation current density  $J_s$  is estimated by fitting the forward current density with the thermionic emission current density equation [16],

$$J = J_s \left[ \exp\left(\frac{qV}{nk_B T}\right) - 1 \right] \quad (5.1)$$

And the saturation current density  $J_s$  is

$$J_s = A^* T^2 \exp\left(-\frac{q\Phi_{\text{Bn}}}{k_B T}\right) \quad (5.2)$$

where  $q$  is the elementary charge,  $V$  is the applied voltage,  $n$  is the ideality factor,  $k_B$  is the Boltzmann constant,  $T$  is the measurement temperature,  $J$  is the measured current density,  $A^*$  is the effective Richardson constant,  $\Phi_{\text{Bn}}$  is the SBH.

On the other hand, assuming that (1) only the edge leakage current density  $J_P$  and area current density  $J_A$  contribute to the saturation current density  $J_s$ , and (2) the parameters  $J_P$  and  $J_A$  are independent of the contact dimension, such as the contact area  $A$  and the contact periphery  $P$ , thus the total saturation current  $I_s$  is given by

$$I_s = A \times J_A + P \times J_P \quad (5.3a)$$

By dividing the contact area  $A$  in both sides of Equation (5.3a), it yields that the saturation current density  $J_s$  has a linear relationship with the ratio of  $P/A$

$$J_s = J_A + \left(\frac{P}{A}\right) J_P \quad (5.3b)$$

Thus, through a plot of the saturation current density  $J_s$  versus  $P/A$ , the area current density  $J_A$  could be extracted by the intercept on the saturation current density axis, while the edge leakage current density  $J_P$  could be given by the slope.

Figure 5.1(b) shows the plot of the saturation current density  $J_s$  versus  $P/A$  for various measurement temperatures, the estimated edge leakage current  $J_P$  and the area current density  $J_A$  are summarized in Table 5.1. Generally, the edge leakage current  $J_P$  is several orders of magnitude smaller than the area current density  $J_A$ , e.g., for the measuring temperature at 294 K, the area current density  $J_A$  is estimated to be  $6.2 \times 10^{-4} \text{ A/cm}^2$ , whereas, the edge leakage current density  $J_P$  is  $3.4 \times 10^{-6} \text{ A/cm}^2$ , two orders of magnitude smaller than the area current density

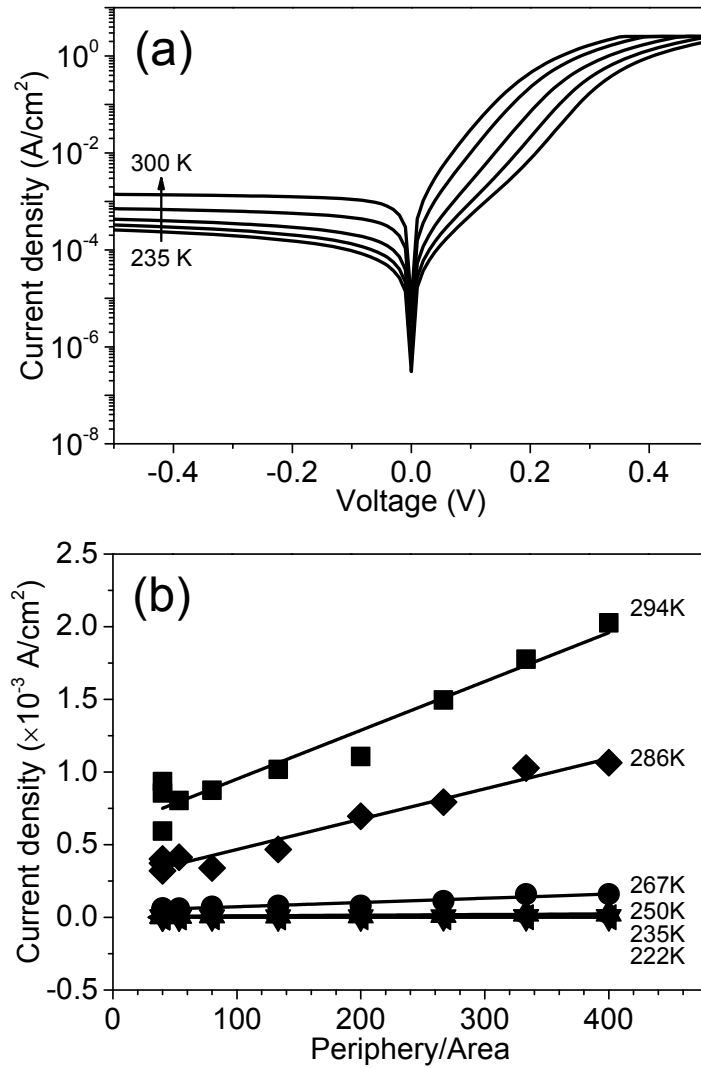


Figure 5.1 (a)  $J$ - $V$  characteristics of epitaxial NiGe(111)/n-type Ge(001) contact measured at 235, 250, 267, 286, and 300 K; (b) Saturation current density as a function of the ratio of contact pattern's periphery and area in order to deduce the current flowing through the edge and area.

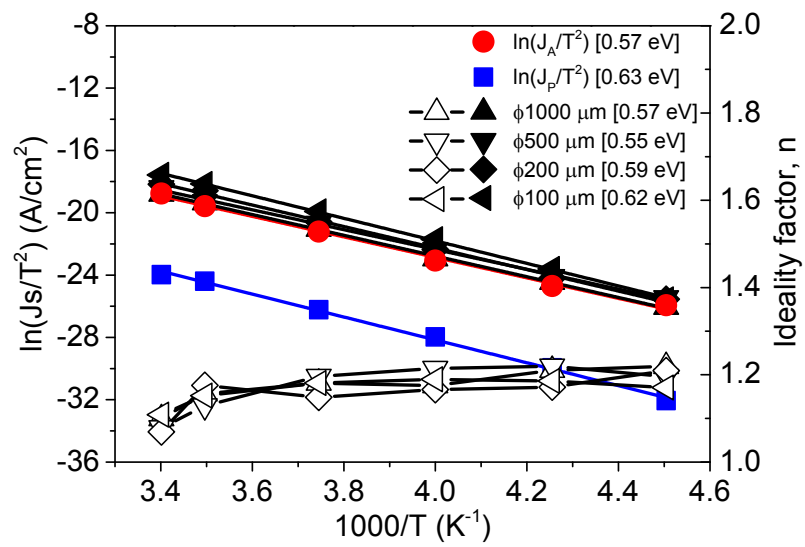


Figure 5.2 The left axis corresponds to the Arrhenius plot of  $\ln(J_s/T^2)$  versus  $1000/T$ , the right axis corresponds to the ideality factor.

$J_A$ . This result indicates the edge leakage current density  $J_P$  is negligibly small, and hardly affects the total saturation current density  $J_s$ , thus the estimated SBH by this method is reliable.

Table 5.1 Summary of the estimated edge leakage current density  $J_P$  and the area current density  $J_A$  for the NiGe(111)/n-type Ge(001) contact.

Current density component	222 K	235 K	250 K	267 K	286 K	294 K
$J_P$ (A/cm <sup>2</sup> )	$5.9 \times 10^{-10}$	$5.4 \times 10^{-9}$	$4.5 \times 10^{-8}$	$2.9 \times 10^{-7}$	$2.1 \times 10^{-6}$	$3.4 \times 10^{-6}$
$J_A$ (A/cm <sup>2</sup> )	$2.7 \times 10^{-7}$	$1.0 \times 10^{-6}$	$6.0 \times 10^{-6}$	$4.4 \times 10^{-5}$	$2.6 \times 10^{-4}$	$6.2 \times 10^{-4}$

### 5.3.2 Uniformity of SBH distribution in the whole contact area

Figure 5.2 shows the Arrhenius plots of  $\ln(J_s/T^2)$  as a function of  $1000/T$  for the NiGe(111)/n-type Ge(001) contacts, and the ideality factors extracted by fitting the forward current density with the thermionic emission current density equation are also shown. The ideality factors are nearly close to 1, which suggests that thermionic emission current is the dominant conduction mechanism. Based on the estimated edge leakage current density  $J_P$  and the area current density  $J_A$  as listed in Table 5.1, the SBHs of contact area and contact edge, estimated by extracting the slopes in the Arrhenius plot, are 0.57 (red line) and 0.63 (blue line) eV, respectively. Those two similar SBHs suggest that the currents flowing through the contact area and through the contact periphery are nearly equivalent.

In addition, the SBH for NiGe(111)/n-type Ge(001) contacts with various contact pattern dimensions (only four kinds of dimensions are shown in Figure 5.2) are also estimated, the estimated SBH are 0.57 – 0.62 eV for the contact pattern dimension range from  $\phi 1000$  – 100  $\mu\text{m}$ , respectively, which are not nearly different from each SBH. This result indicates that the SBHs are nearly not dependent on the contact pattern dimension, namely, the SBH is uniformly distributed in the whole contact area, including the edge.

### 5.3.3 The effect of defects in the depletion region on the electrical properties of NiGe/n-type Ge contacts

Figures 5.3 - 5.6 show the  $J$ - $V$  characteristics and the corresponding

Arrhenius plots of various NiGe/Ge contacts with different crystalline structures of NiGe layer. Figure 5.3 corresponds to an epitaxial NiGe(100)/n-type Ge(110) contact, Figure 5.4 corresponds to an epitaxial NiGe(102)/n-type Ge(110) contact, Figure 5.5 corresponds to a polycrystalline NiGe/n-type Ge(110) contact, and Figure 5.6 corresponds to a polycrystalline NiGe/n-type Ge(001). All of those  $J$ - $V$  characteristics show the rectifying characteristics.

As mentioned in the section 5.3.1, the saturation current density  $J_s$  is extracted by fitting the forward current density with the thermionic emission current density equation. Besides that, the saturation current density  $J_s$  also could be estimated by the reverse current density  $J_r$ , since the  $\exp\left(\frac{qV}{nk_B T}\right)$  section in Equation (5.1) is nearly equal to zero when the applied voltage is negative, thus, the saturation current density  $J_s$  is equal to the reverse current density  $J_r$ , which is described by the transformed Equation (5.4),

$$J_r = J_s \left[ \exp\left(\frac{qV}{nk_B T}\right) - 1 \right] = -J_s \quad (5.4)$$

In this study, we extracted the saturation current density  $J_s$  at the reverse bias -0.2 V.

By comparison the extracted saturation current density  $J_s$  from the reverse current density and the forward current density in the Arrhenius plots of Figures 5.3(b) - 5.6(b) for various NiGe/n-type Ge contacts with different crystalline structures of NiGe layer, the  $J_s$  from the reverse current density is generally larger than that from forward current density, moreover, the corresponding SBH base on the  $J_s$  from the reverse current density is also smaller than that based on the  $J_s$  from the forward current density, as summarized in Table 5.2. We consider that this discrepancy is due to the defects locating at the depletion region. For the reverse bias, the depletion width is longer than that for forward bias, take the epitaxial NiGe(111)/n-type Ge(001) contact for an example, the estimated depletion width (applied voltage  $V = -0.2$  V) from  $C$ - $V$  characteristics is about 1.4  $\mu\text{m}$ , which is about 0.8  $\mu\text{m}$  longer than that when the applied voltage is 0.2 V, as shown in Figure 5.7. Thus the amount of defects for the reverse bias is more than that for forward bias, those defects might cause the recombination current, thus the  $J_s$  from the reverse current density is generally larger than that from forward current density, and the SBH is under estimated by the reverse current density.

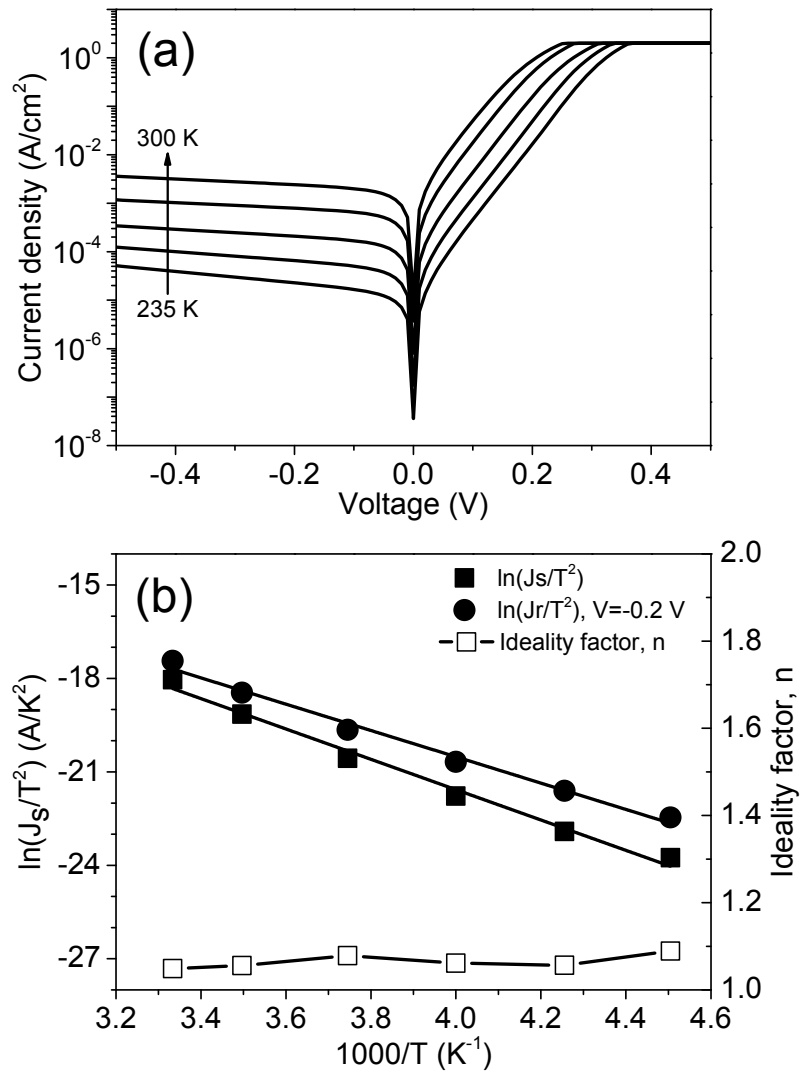


Figure 5.3 (a)  $J$ - $V$  characteristics measured at 235, 250, 267, 286, and 300 K, (b) the corresponding Arrhenius plot of epitaxial NiGe(100)/n-type Ge(110) contact.

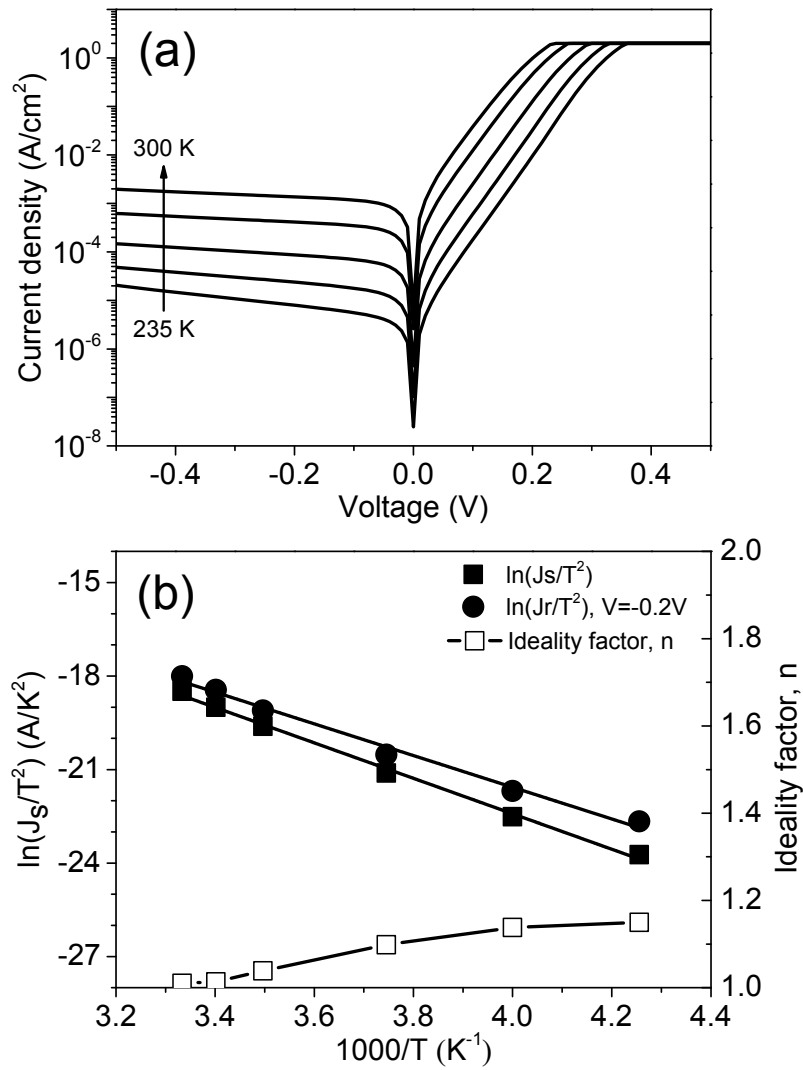


Figure 5.4 (a)  $J$ - $V$  characteristics measured at 235, 250, 267, 286, and 300 K, (b) the corresponding Arrhenius plot of epitaxial NiGe(102)/n-type Ge(110) contact.

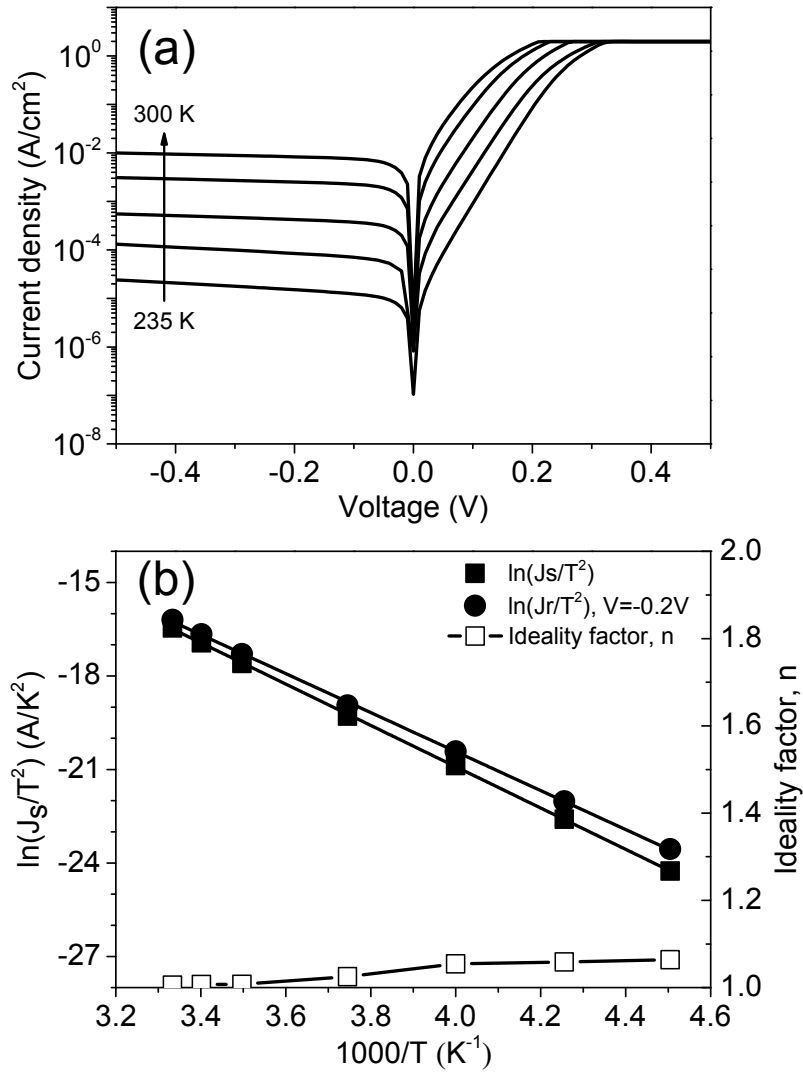


Figure 5.5 (a)  $J$ - $V$  characteristics measured at 235, 250, 267, 286, and 300 K, (b) the corresponding Arrhenius plot of polycrystalline NiGe/n-type Ge(110) contact.

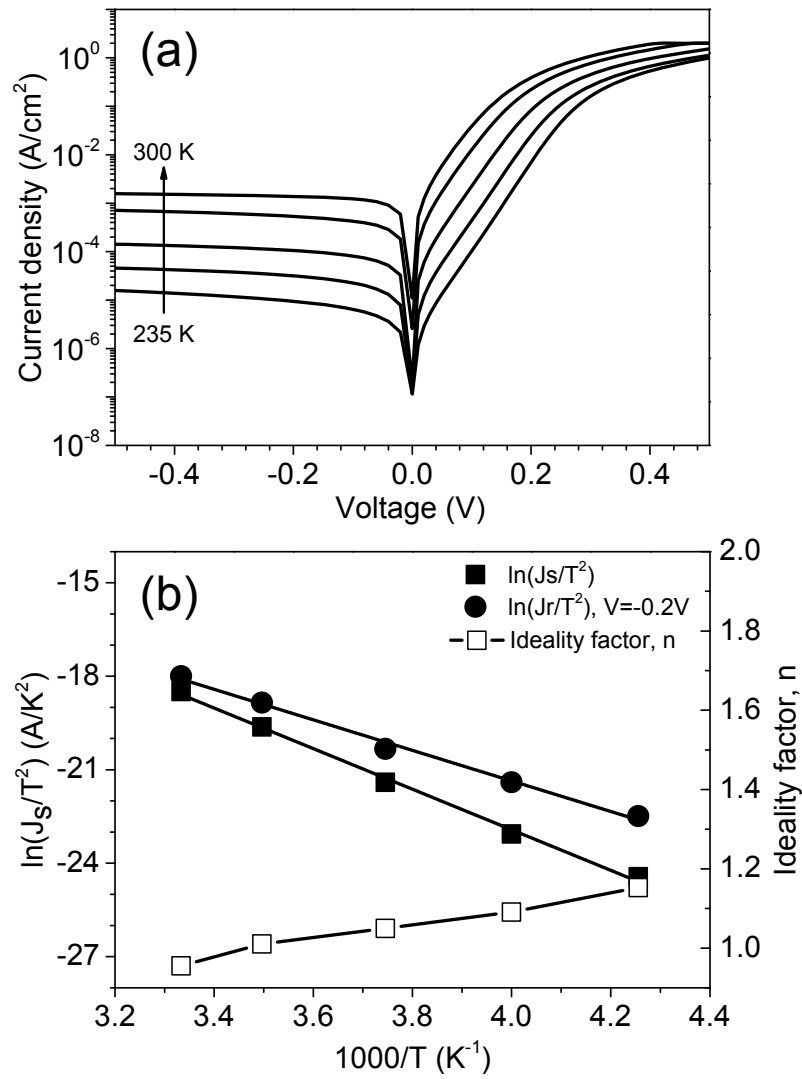


Figure 5.6 (a)  $J$ - $V$  characteristics measured at 235, 250, 267, 286, and 300 K, (b) the corresponding Arrhenius plot of polycrystalline NiGe/n-type Ge(001).

Table 5.2 Summary of the SBHs of NiGe/n-type Ge contacts with different crystalline structures.

Sample (n-type Ge)	Germanidation method	Crystalline structure	SBH, eV (Forward)	SBH, eV (Reverse)
Ni/Ge(110)	Solid phase reaction	Epi. NiGe(100)//Ge(110)	0.42	0.36
Ni/GeO <sub>x</sub> (thin)/ Ge(110)	Solid phase reaction	Epi. NiGe(102)//Ge(110)	0.49	0.44
Ni/Ge(110)	Reactive deposition	Poly. NiGe/Ge(110)	0.57	0.54
Ni/Ge(001)	Solid phase reaction	Poly. NiGe/Ge(001)	0.56	0.42
Ni/Ge(001)	Reactive deposition	Epi. NiGe(111)//Ge(001)	0.57	0.36

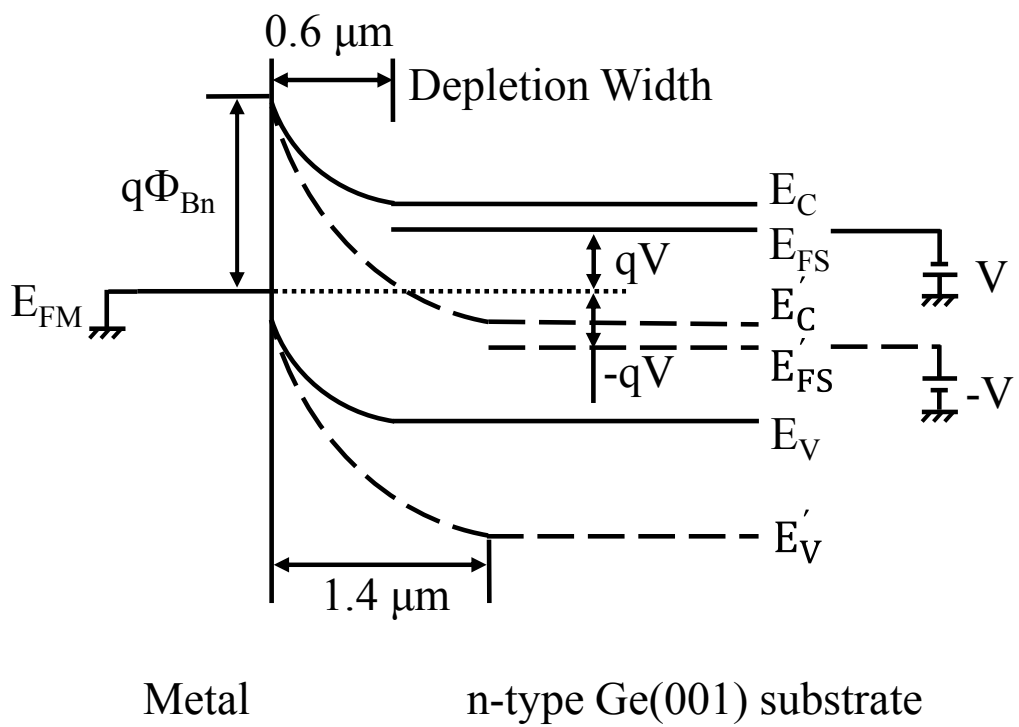


Figure 5.7 The energy band diagram of epitaxial NiGe(111)/n-type Ge(001) contact under the forward bias ( $V = 0.2 \text{ V}$ ) and reverse bias ( $V = -0.2 \text{ V}$ ).

### **5.3.4 The effect of crystalline structure of NiGe layer on the electrical properties of NiGe/n-type Ge contacts**

As discussed previously, the calculated SBH based on the reverse current density is underestimated, thus the following mentioned SBHs is estimated based on the forward current, if not specified. As summarized in Table 5.2, the SBHs of the polycrystalline NiGe/n-type Ge contacts hardly depend on the orientation of Ge substrate, the SBHs of the polycrystalline NiGe/n-type Ge(110) contact and polycrystalline NiGe/n-type Ge(001) contact are estimated to be 0.57 eV and 0.56 eV, respectively. Whereas, the SBHs of the epitaxial NiGe/n-type Ge contacts present a dependence on the crystalline structure of NiGe layer. For the epitaxial NiGe(100)/n-type Ge(110) contact, the SBH is estimated to be 0.42 eV, which is about 0.15 eV lower than that of the polycrystalline NiGe/n-type Ge contacts. The epitaxial NiGe(102)/n-type Ge(110) contact has a medium SBH (0.49 eV), and the epitaxial NiGe(111)/n-type Ge(001) contact shows a SBH as large as that of the polycrystalline NiGe/n-type Ge contact.

Generally, it is reported that the SBH is hardly modulated by the extrinsic factors, such as the germanide reaction, annealing ambient, and the orientation of the Ge substrate, since the FLP is caused by MIGS, an intrinsic factor. However, in this study, the distinctive modulation of SBHs through controlling the crystalline structures of NiGe/n-type Ge contact could not only be explained by the MIGS model.

We consider that this modulation of SBHs is a consequence of the variation of the density of the interface states induced by the extrinsic factors, such as the dangling bonds and defects. Figure 5.8 (a) shows the high resolution image of the epitaxial NiGe(100) layer on Ge(110) substrate, the well-resolved lattice planes are observed to extend throughout the entire NiGe layer, which reveals the high crystalline quality of the epitaxial NiGe layer. Of importance, the NiGe 002 lattice plane matches well with the Ge 002 lattice plane, and the misfit is as small as approximately 2.4%. Therefore, we can expect that the density of the defects or dangling bonds at the NiGe/Ge interface is much lower than that for polycrystalline NiGe on Ge(001), thus, the FLP is alleviated for the epitaxial NiGe(100)/n-type Ge(110) contact.

As for the epitaxial NiGe(102) on Ge(110) substrate, a high crystalline

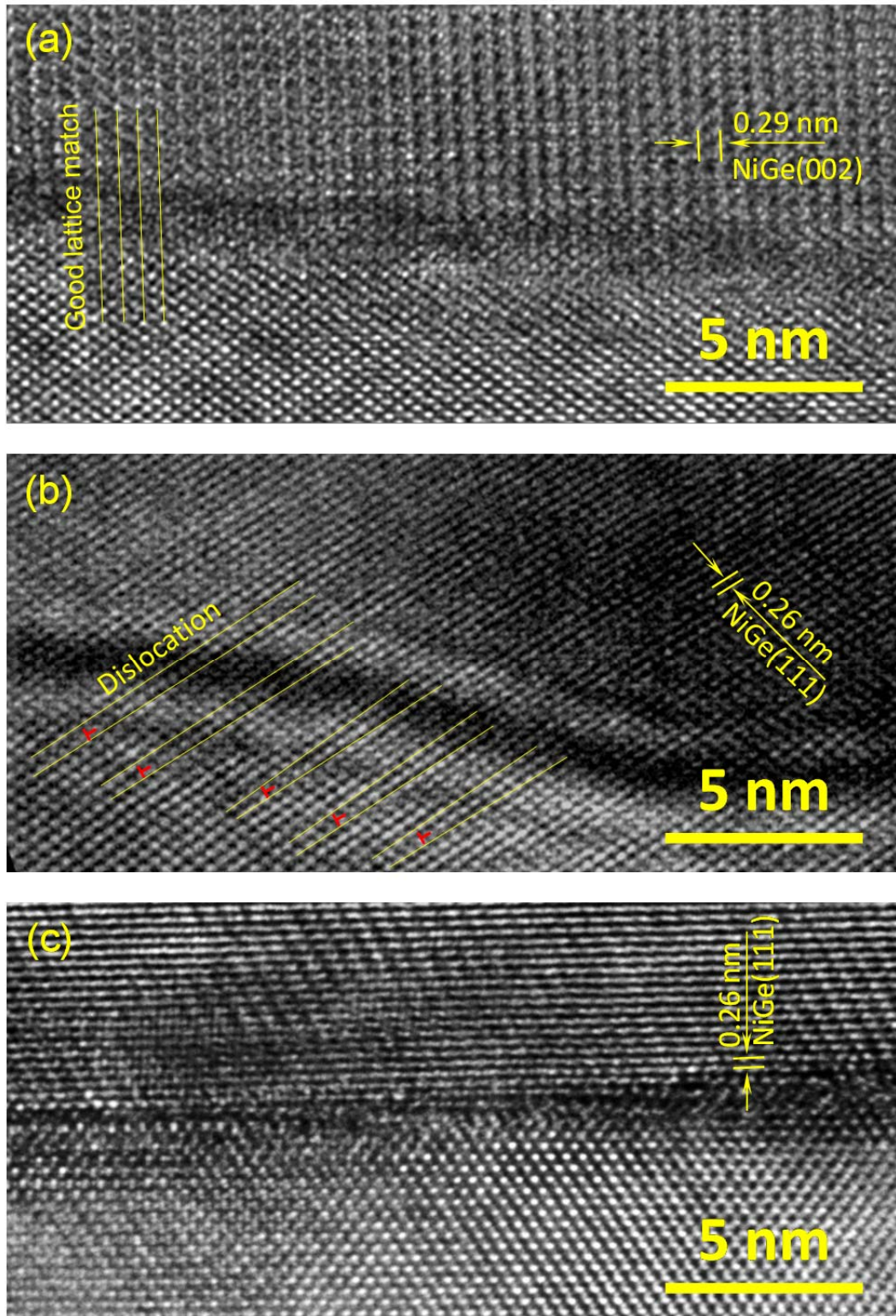


Figure 5.8 High resolution images of the NiGe/Ge interface: (a) Epitaxial NiGe(100)/Ge(110), (b) Epitaxial NiGe(102)/Ge(110), (c) Epitaxial NiGe(111)//Ge(001).

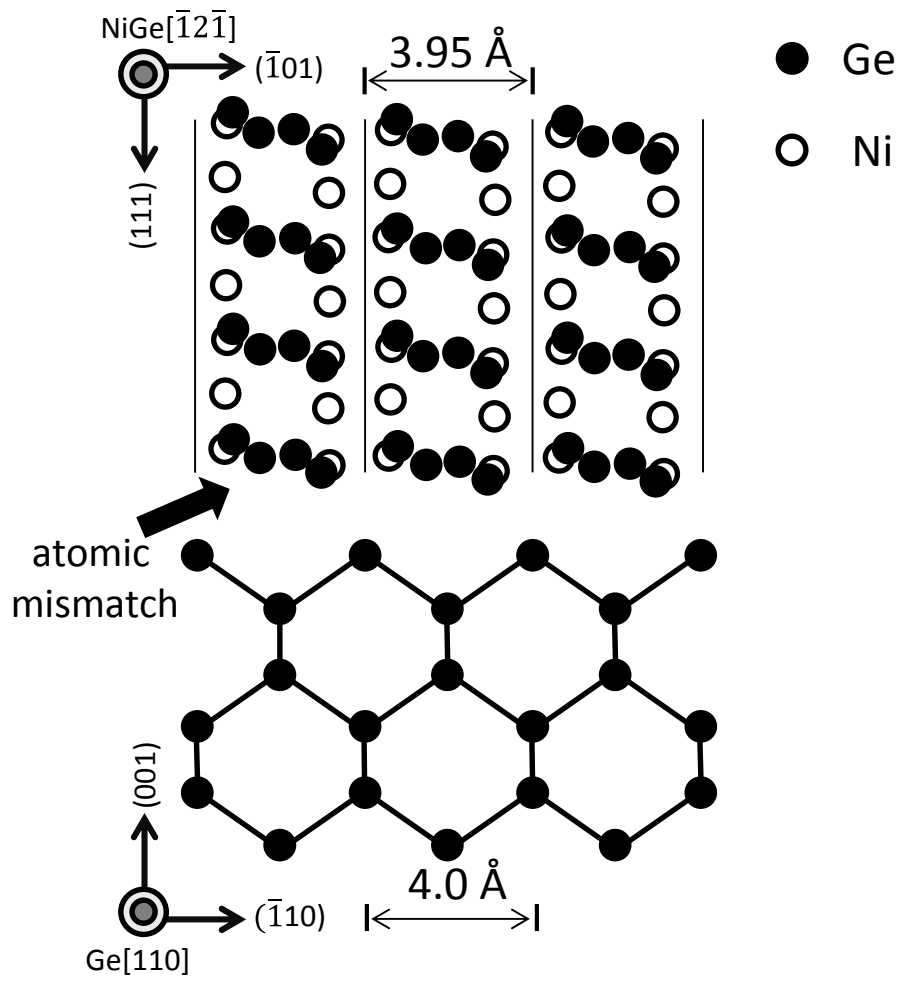


Figure 5.9 Atomic arrangement at the interface between epitaxial NiGe(111) layer and Ge(001) substrate, projected from the Ge[110] direction.

quality of epitaxial layer is also observed in the high resolution image (Figure 5.8(b)), but many dislocations are found near to the interface, as indicated by the “ $\perp$ ”. Those dislocations might induce the interface states, thus result in a relative high SBH (0.49 eV), compared with that of the epitaxial NiGe(100)/n-type Ge(110) contact.

Next, we discuss about the special case of the epitaxial NiGe(111)/n-type Ge(001) contact. The estimated SBH is 0.57 eV, which nearly has no difference from that of the polycrystalline NiGe/n-type Ge contact, even though the epitaxial NiGe layer with good crystalline quality is formed, as shown in Figure 5.8(c). However, it makes sense when inspecting the atomic arrangement at the interface of epitaxial NiGe(111) and Ge(001) substrate, the corresponding schematic diagram is shown in Figure 5.9. At the interface, the atoms in NiGe side nearly has no match with the atoms in Ge substrate, thus the density of the dangling bonds might have no difference from that of the polycrystalline NiGe/Ge interface, in other words, the interface of epitaxial NiGe(111) and Ge(001) substrate is equivalent to that of polycrystalline NiGe and Ge substrate, hence, the FLP could not be alleviated like the other epitaxial case, and the SBH of epitaxial NiGe(111)/n-type Ge(001) contact is similar with that of polycrystalline NiGe/n-type Ge contact.

Last, we have to note that besides the interfacial crystalline structure, the orientation of epitaxial NiGe also has the possibility to affect the SBH, since NiGe has a strong dependence of work functions  $\phi_m$  on the crystalline orientation. It is reported that NiGe(100) surface has a work function of 4.37 eV [17], based on the classical Schottky-Mott theory, the expected SBH for this work function is 0.37 eV, which is close to the estimated value 0.42 eV. Unfortunately, the work functions of the NiGe(102) and (111) surface has not yet been investigated, it needs further study in future.

### **5.3.5 Capacitance-Voltage characteristics of NiGe/Ge contacts**

The SBHs for NiGe/n-type Ge contact were also estimated by capacitance-voltage ( $C$ - $V$ ) characteristics [18]. For a metal/n-type semiconductor with a uniformly impurity concentration in semiconductor, the relationship between capacitance  $C$  and applied voltage  $V$  is often given by

$$\frac{1}{C^2} = \frac{2(V_{bi} - V - \frac{k_B T}{q})}{q \epsilon_s N_D} \quad (5.5)$$

Where  $q$  is the electronic charge,  $\epsilon_s$  is the permittivity of semiconductor,  $N_D$  is the net donor concentration,  $V_{bi}$  is the built-in potential,  $k_B$  is Boltzmann's constant, and  $T$  is the measuring temperature.

Based on this equation, the built-in potential  $V_{bi}$  could be extrapolated from the intercept on the voltage axis in a plot of  $1/C^2$  versus the applied voltage  $V$ , moreover, the impurity concentration  $N_D$  could be calculated by the slope of  $1/C^2$  as a function of applied voltage  $V$ , the detail is as follows

$$N_D = \frac{2}{q \epsilon_s} \frac{dV}{d\left(\frac{1}{C^2}\right)} \quad (5.6)$$

On the other hand, according to the energy band diagram of metal/semiconductor, the SBH is expressed by the sum of  $V_{bi}$  and  $V_n$ ,

$$\Phi_B = V_n + V_{bi} \quad (5.7)$$

where  $V_n$  is the energy difference between  $E_c$  and  $E_F$  of semiconductor, this parameter is a function of the impurity concentration  $N_D$

$$V_n = \frac{kT}{q} \ln\left(\frac{N_C}{N_D}\right) \quad (5.8)$$

where  $N_C$  is the effective density of states for free electron in the conduction band. Therefore, combining Equations (5.6), (5.7), and (5.8), the Schottky barrier height could be obtained.

Figures 5.10 – 5.13 show the  $C$ - $V$  characteristics of NiGe/n-type Ge contacts with various crystalline structures. All of those  $C$ - $V$  characteristics exhibit a good linear relationship of  $1/C^2$  and reverse bias  $V$ , which means that the ionized donor concentration  $N_D$  is uniformly distributed in the depletion region. And the donor concentrations  $N_D$  (NiGe/n-type Ge(110) system if not specified) are estimated to be approximately  $2 \times 10^{16} \text{ cm}^{-3}$  regardless of the crystalline structures of NiGe layers. Moreover, those estimated donor concentrations  $N_D$  in the depletion region have no difference with the specific donor concentration of the bulk Ge(110) substrate ( $3.5 \sim 6 \times 10^{16} \text{ cm}^{-3}$ ) as mentioned in the experiment section. Those results indicate that the germanidation hardly causes the segregation of the donor impurities, and the donor concentrations keep the uniform distribution even after annealing for the germanidation.

Besides the donor concentration  $N_D$ , the SBH,  $V_{bi}$ , and  $V_n$  were also estimated. As expressed in Equation (5.8),  $V_n$  has a linear function with the

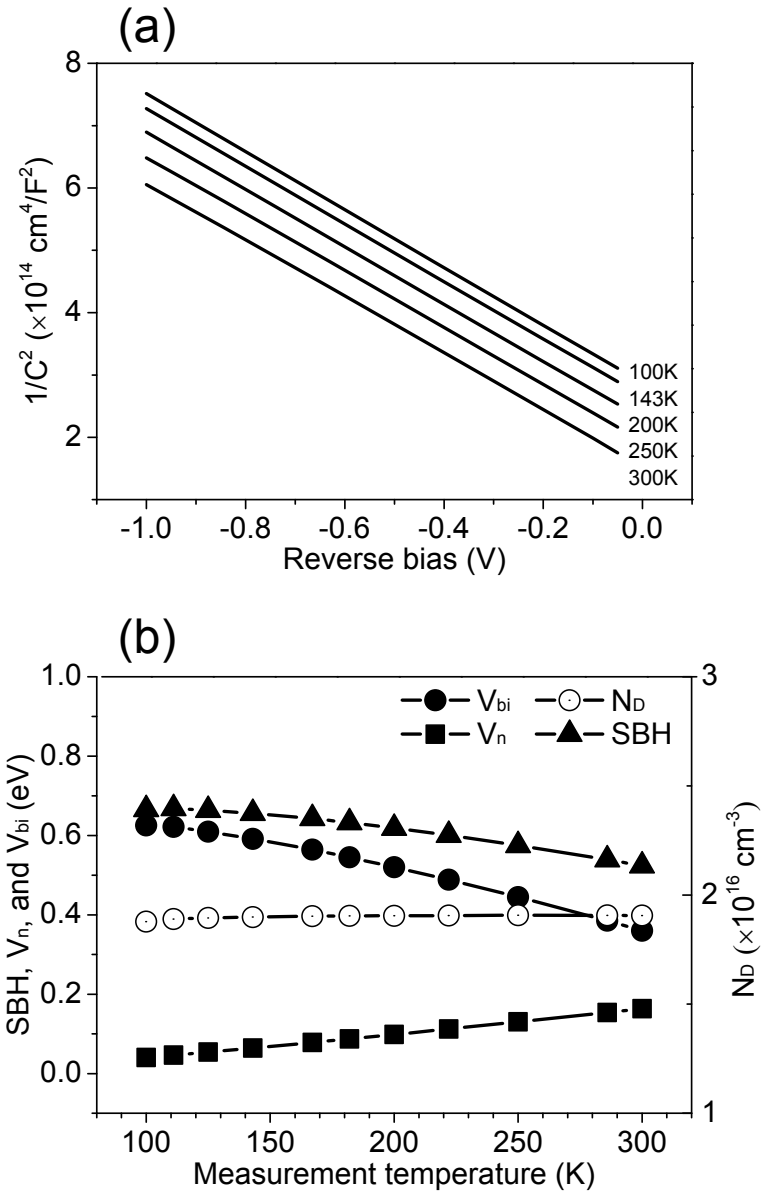


Figure 5.10 (a) The capacitance-voltage characteristics of epitaxial NiGe(100)/n-type Ge(110) contact, (b) The estimated parameters SBH,  $V_n$ ,  $V_{bi}$ , and  $N_D$  as a function of measurement temperature.

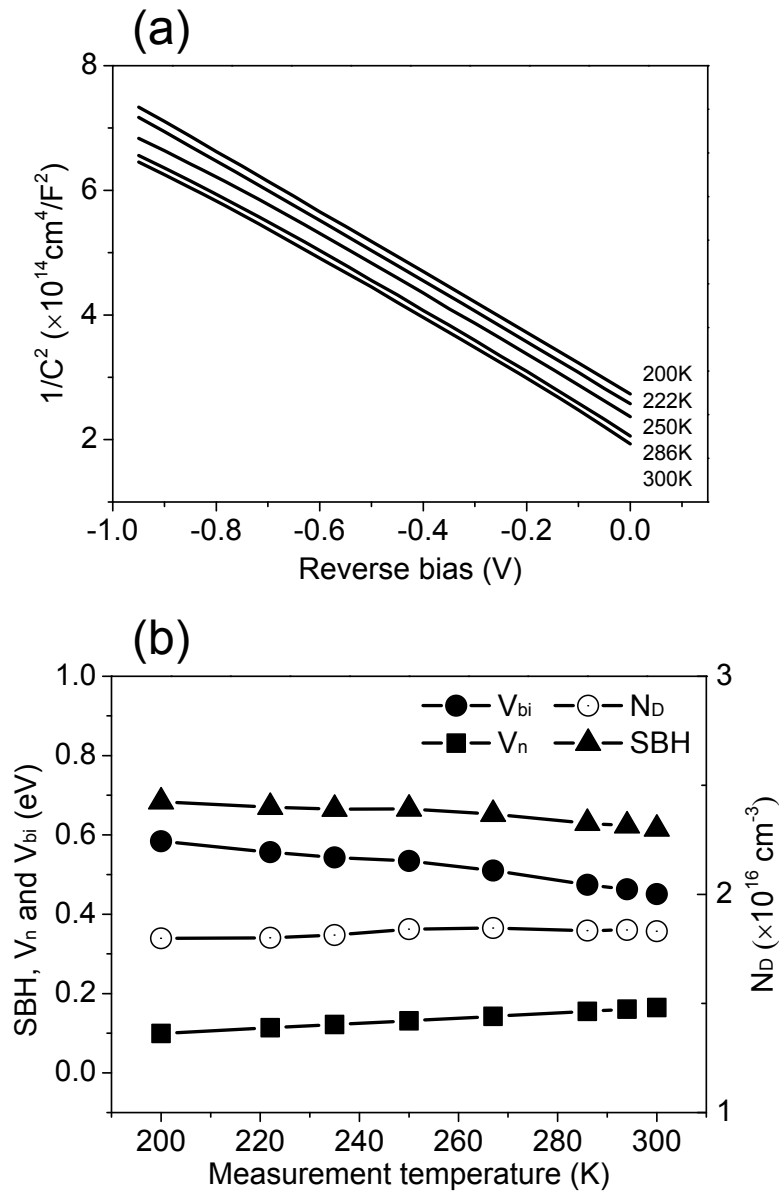


Figure 5.11 (a) The capacitance-voltage characteristics of epitaxial NiGe(102)/n-type Ge(110) contact, (b) The estimated parameters SBH,  $V_n$ ,  $V_{bi}$ , and  $N_D$  as a function of measurement temperature.

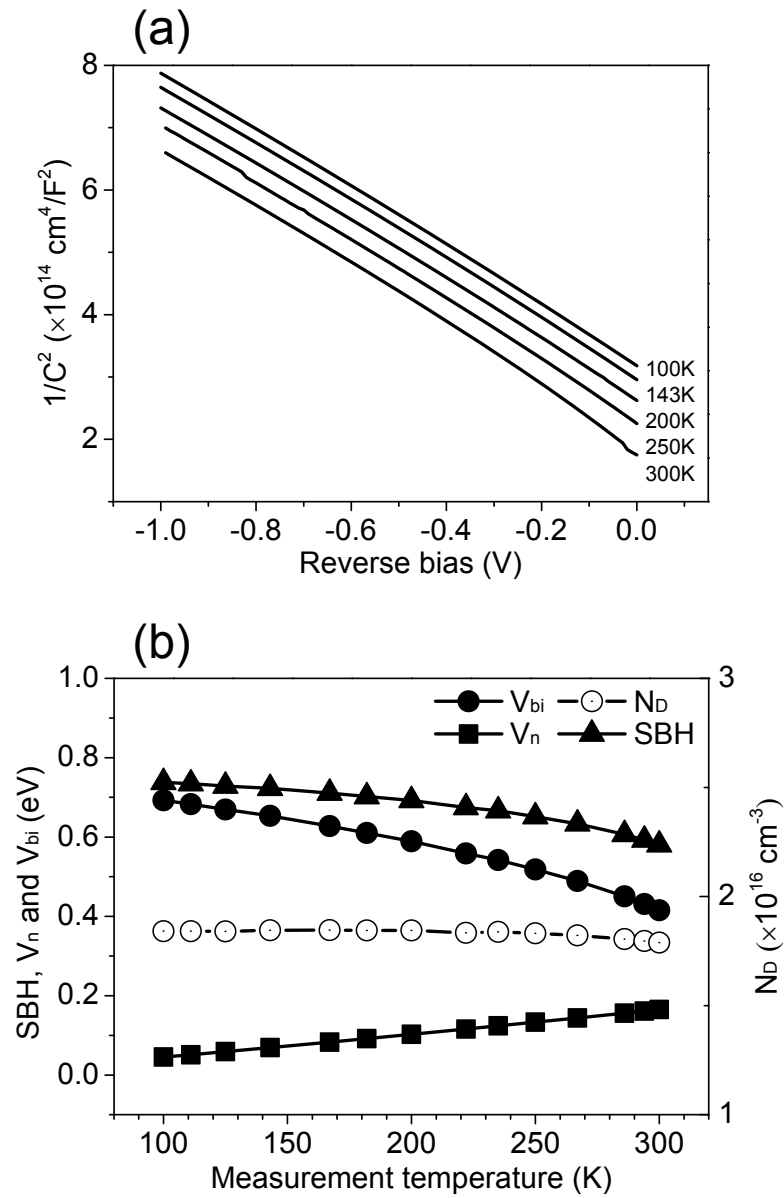


Figure 5.12 (a) The capacitance-voltage characteristics of polycrystalline NiGe/n-type Ge(110) contact, (b) The estimated parameters SBH,  $V_n$ ,  $V_{bi}$ , and  $N_D$  as a function of measurement temperature.

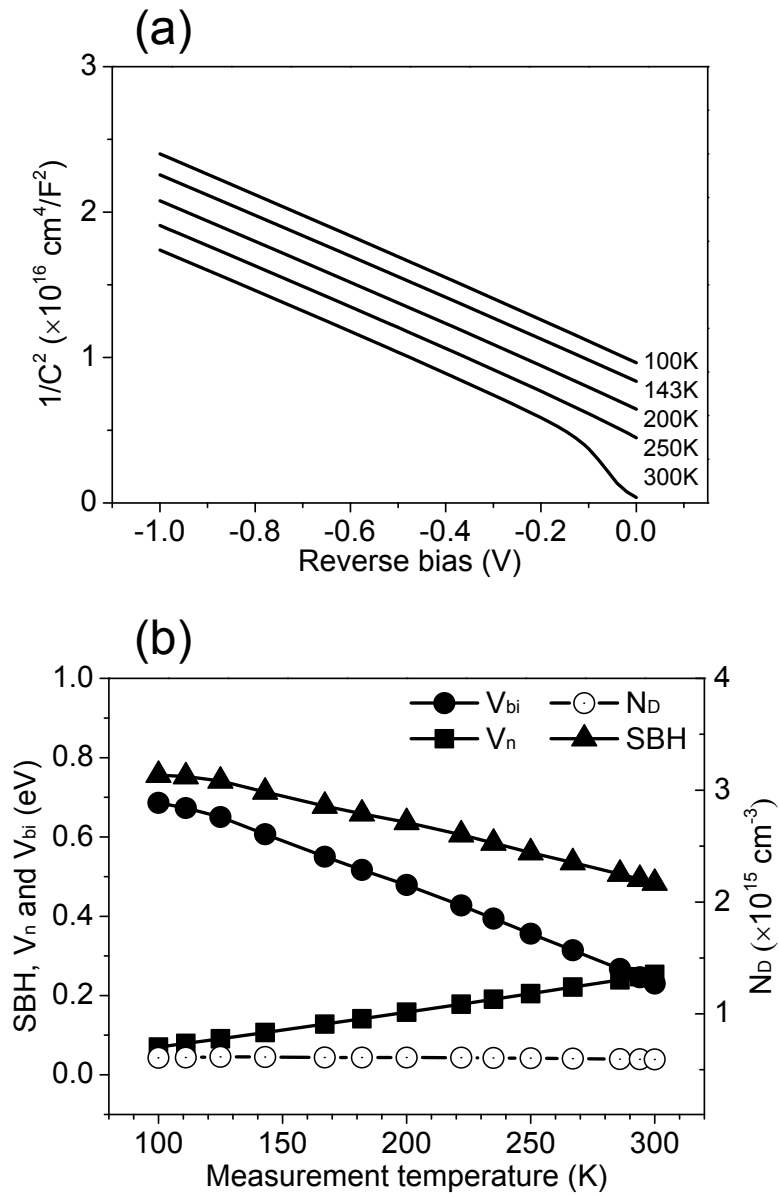


Figure 5.13 (a) The capacitance-voltage characteristics of epitaxial NiGe(111)/n-type Ge(001) contact, (b) The estimated parameters SBH,  $V_n$ ,  $V_{bi}$ , and  $N_D$  as a function of measurement temperature.

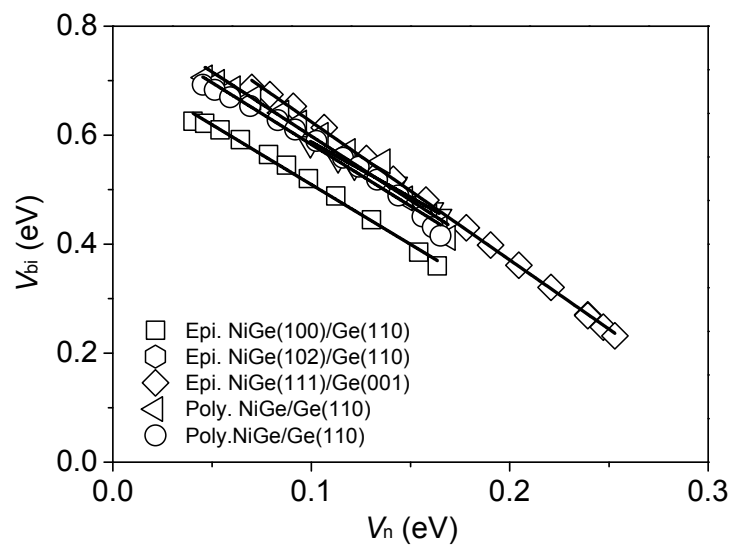


Figure 5.14 The plot of built-in potential  $V_{bi}$  versus  $V_n$ .

measurement temperature  $T$ , this temperature dependence of  $V_n$  is clearly shown in Figures 5.10(b) – 5.13(b). On the other hand, theoretically, the SBH is independent on the measuring temperature, and equals to the sum of  $V_n$  and  $V_{bi}$ . Thus,  $V_n$  has a linear relationship with  $V_{bi}$ , and the slope of the  $V_{bi}$  versus  $V_n$  equals to -1. However, in this study, the slope is approximately -2, even though a good linear relationship is obtained, as shown in Figure 5.14. At present, the reason of this deviation from the theory has not yet been clarified, we need further investigation.

## 5.4 Conclusions

We have investigated the electrical properties of various NiGe/n-type Ge contacts with different crystalline structures. The edge leakage current and contact area current were evaluated. We found that the edge leakage current is nearly two orders smaller than the contact area current, thus the edge leakage effect could be neglected when estimating the SBH by  $J$ - $V$  method. We also found that the SBHs are hardly influenced by the dimensions of the contact pattern, namely, the SBH is uniformly distributed in the whole contact area. We have successfully demonstrated the modulation of FLP by controlling the crystalline structures of NiGe layers. Compared with the polycrystalline NiGe/n-type Ge contacts, the SBH is reduced by as large as 0.15 eV for the epitaxial NiGe(100)/n-type Ge(110) contact. However, for an epitaxial NiGe(111)/n-type Ge(001) contact, the estimated SBH has no difference from that of polycrystalline NiGe/n-type Ge contact, even though the epitaxial NiGe layer with atomically smooth interface. This distinctive modulation of SBH could not only be explained by MIGS model, we consider that this modulation of SBHs is a consequence of the variation of the density of the interface states induced by the extrinsic factors, such as the dangling bonds and defects. And our results give us a hint that the modulation of the SBH by controlling the crystalline structures is possible. To realize further low SBH, a completely atomic matching at the metal/semiconductor interface is required.

## References

- [1] Y.J. Yang, W. Ho, C.-F. Huang, S. Chang, C. Liu, *Applied Physics Letters* **91/10** (2007) 102103.
- [2] T. Krishnamohan, D. Kim, T.V. Dinh, A.-T. Pham, B. Meinerzhagen, C. Jungemann, K. Saraswat, *Electron Devices Meeting, 2008. IEDM 2008. IEEE International, IEEE, 2008*, p. 1.
- [3] A.M. Noori, M. Balseanu, P. Boelen, A. Cockburn, S. Demuyneck, S. Felch, S. Gandikota, A.J. Gelatos, A. Khandelwal, J.A. Kittl, *Electron Devices, IEEE Transactions on* **55/5** (2008) 1259.
- [4] S.D. Kim, S. Narasimha, K. Rim, *Electron Devices Meeting, 2005. IEDM Technical Digest. IEEE International, IEEE, 2005*, p. 149.
- [5] S.D. Kim, C.-M. Park, J.C. Woo, *Electron Devices, IEEE Transactions on* **49/3** (2002) 467.
- [6] S.D. Kim, C.-M. Park, J.C. Woo, *Electron Devices, IEEE Transactions on* **49/3** (2002) 457.
- [7] F. Flores, C. Tejedor, *Journal of Physics C: Solid State Physics* **20/2** (1987) 145.
- [8] A. Suzuki, S. Asaba, J. Yokoi, K. Kato, M. Kurosawa, M. Sakashita, N. Taoka, O. Nakatsuka, S. Zaima, *Japanese Journal of Applied Physics* **53/4S** (2014) 04EA06.
- [9] T. Nishimura, K. Kita, A. Toriumi, *Applied Physics Letters* **91/12** (2007) 123123.
- [10] Y. Zhou, M. Ogawa, X. Han, K.L. Wang, *Applied Physics Letters* **93/20** (2008) 202105.
- [11] R.R. Lieten, S. Degroote, M. Kuijk, G. Borghs, *Applied Physics Letters* **92/2** (2008) 022106.
- [12] M. Kobayashi, A. Kinoshita, K. Saraswat, H.-S.P. Wong, Y. Nishi, *Journal of Applied Physics* **105/2** (2009) 023702.
- [13] T. Nishimura, O. Nakatsuka, S. Akimoto, W. Takeuchi, S. Zaima, *Microelectronic Engineering* **88/5** (2011) 605.
- [14] K. Yamane, K. Hamaya, Y. Ando, Y. Enomoto, K. Yamamoto, T. Sadoh, M. Miyao, *Applied Physics Letters* **96/16** (2010) 162104.
- [15] Y. Deng, O. Nakatsuka, J. Yokoi, N. Taoka, S. Zaima, *Thin Solid Films* **557** (2014) 84.
- [16] H.A. Bethe, *Theory of the boundary layer of crystal rectifiers*, Radiation Laboratory, Massachusetts Institute of Technology, 1942.
- [17] M. Niranjana, L. Kleinman, A. Demkov, *Physical Review B* **75/8** (2007) 085326.
- [18] C. Crowell, J. Sarace, S. Sze, *TRANSACTIONS OF THE METALLURGICAL SOCIETY OF AIME* **233/3** (1965) 478.

## 6 Conclusion and future work

We have investigated the epitaxial formation and electrical properties of Ni germanide/Ge contacts for the application of future highly scaled Ge-based MOSFET. Epitaxial NiGe layers with atomically flat and uniform interface have been explored not only on Ge(001) substrate but also on Ge(110) substrate. Those epitaxial NiGe layers exhibit a potential application in the highly scaled Ge-based MOSFET because of their promising thermal stability and morphological stability. On the other hand, we have successfully demonstrated the alleviation of FLP by controlling the crystalline structures of NiGe layers. Those works give rise to a new hint that controlling the crystalline structure of metal layers enables one to control the SBH of metal/Ge contacts, and the origin of FLP is not due to an intrinsic factor, e.g. MIGS, but extrinsic factors such as dangling bonds and disorders at the metal/Ge interfaces.

At first, we summarize the epitaxial formation of NiGe layer on Ge(001) substrate. An epitaxial NiGe layer with an atomically flat and uniform interface is achieved by a 2-steps deposition method (reactive deposition + subsequent room temperature deposition), assisted with solid phase reaction method. And the orientation relationship between the epitaxial NiGe layer and Ge(001) substrate is NiGe(111) // Ge(001) and NiGe[0 $\bar{1}$ 1] // Ge[110].

We also discussed this epitaxial formation in detail. With the reactive deposition method only, an epitaxial NiGe layer could be formed, but the thickness of the epitaxial layer is limited to below 22 nm. Once over this critical thickness, the polycrystalline NiGe formation occurs. Moreover, the interface between the epitaxial NiGe layer and Ge(001) substrate is a little rough. Those issues have been solved by the 2-steps deposition plus solid phase reaction as mentioned in the last paragraph.

Here, we demonstrate the promotion of epitaxial formation by the 2-steps deposition in detail. At first, a thin epitaxial NiGe layer is formed by reactive deposition. Then, an additional Ni layer is deposited on the initially formed epitaxial NiGe layer at room temperature. Subsequently, the complete germanidation is performed by the post annealing, during the germanidation, the initially formed epitaxial NiGe layer plays a role of single crystal seed to enhance

the epitaxial formation.

The reason why the polycrystalline formation is suppressed by the 2-steps deposition is also clarified. At first, we describe the polycrystalline formation when the thickness of reactive deposited NiGe is over the limitation of epitaxial formation. Ge atoms are found to be the dominant diffusion species during the reactive deposition, it means that the crystallization front is on the surface of the formed NiGe layer, rather than the interface between the formed NiGe layer and Ge(001) substrate. On the other hand, the 2-D growth would transform to 3-D growth with increase in the thickness of the reactively deposited NiGe layer, and the surface would become rough. Relying on this rough surface, the heterogeneous nucleation is easy to happen, thus the polycrystalline formation is induced.

However, for the 2-steps deposition sample, during the subsequent germanidation process, the dominant diffusion species are changed to be Ni atoms, and the crystallization front is also changed to the interface of NiGe/Ge. In this situation, the heterogeneous nucleation does not happen, and the initially formed epitaxial NiGe plays a role of single crystal seeds to induce the epitaxial formation, thus an epitaxial NiGe layer with high crystalline quality is achieved.

On the other hand, a partially epitaxial formation of NiGe layer on Ge(110) substrate is also achieved by solid phase reaction. Of interesting, the orientation relationship of the epitaxial NiGe domain with Ge(110) substrate could be modulated by the surface condition of Ge substrate before Ni deposition. For the samples with a clean surface, the Ni deposition is conducted on a clean Ge substrate without any contaminations or native oxide layer, the orientation relationships are NiGe(100) // Ge(110) and NiGe[001] // Ge[001], while those are NiGe(102) // Ge(110) and NiGe[010] // Ge[001] for the samples with an ultra-thin native oxide interlayer between the as-deposited Ni layer and Ge(110) substrate.

We also found that the growths of epitaxial and polycrystalline NiGe domains depend on the annealing temperature. For the samples with clean surface, the growth of the epitaxial domain is coincident with that of the polycrystalline domain. The growths of polycrystalline and epitaxial domains are restrained at an annealing temperature lower than 250 °C, and they grow together at an annealing temperature higher than 300 °C. For the samples with an ultra-thin native oxide

interlayer, a low annealing temperature of 200 °C favors the epitaxial growth, which is replaced by polycrystalline growth at a high annealing temperature of above 275 °C.

Next, we summarize the electrical properties of various NiGe/n-type Ge contacts with different crystalline structures. We found that the SBH of NiGe/Ge contact could be modulated by controlling the crystalline structures of NiGe layer. Compared with the polycrystalline NiGe/n-type Ge contacts, the SBH is reduced by as large as 0.15 eV for the epitaxial NiGe(100)/n-type Ge(110) contact. However, for an epitaxial NiGe(111)/n-type Ge(001) contact, the estimated SBH is not so low compared to that of the polycrystalline NiGe/n-type Ge contact with the FLP case, even though the epitaxial NiGe layer with good crystalline quality is formed. This distinctive modulation of SBH could not only be explained by MIGS model. We consider that this modulation of SBHs is a consequence of the variation of the density of the interface states induced by the extrinsic factors, such as the dangling bonds and defects. And our results give us a hint that the modulation of the SBH by controlling the crystalline structures is possible. To realize further low SBH, a completely atomic matching is required.

In the future, a further study is needed to clarify the origin of the FLP and to develop an Ohmic contact for the application of future highly scaled Ge-based MOSFET. As for clarifying the origin of the FLP, we have to find a way to quantify the defects or dangling bonds at the interface of NiGe/Ge, and further discussion about the relationship between the SBH and the amount of the defects or dangling bonds is also needed. In terms of developing an Ohmic contact, a new material with a low work function, such as ytterbium germanide or hafnium germanide, will be chosen at first. A co-deposition method might be performed to promote the epitaxial formation.

## **Acknowledgement**

This dissertation entitled “Control of Crystalline Structures and Electrical Properties of Metal Germanide/Ge Contact” is the author’s research achievements in Ph. D program in Department of Crystalline Materials Science, Graduate School of Engineering, Nagoya University, Japan.

First and foremost, I would like to express my sincere gratitude to my supervisor Prof. Shigeaki Zaima and Prof. Osamu Nakatsuka for offering a great research environment and their constructive guidance. Here, I have my utmost respect for their vast knowledge, experience, and patience.

I appreciate Prof. Seiichi Miyazaki and Prof. Tsukasa Torimoto for providing valuable comments on my PhD dissertation. I would like to thank Associate Prof. Noriyuki Taoka, Assistant Prof. Mitsuo Sakashita, Assistant Prof. Wakana Takeuchi, and Dr. Masashi Kurosawa for beneficial discussions and experimental supports.

My gratitude also goes to all of members in Zaima laboratory not only for their help in my research, but also for growth together in Zaima laboratory for three years. Especially, I would like to thank Mr. Jun Yokoi, Mr. Akihiro Suzuki, Mr. Shigehisa Shibayama, Mr. Takanori Asano, Mr. Takashi Yamaha, and Mr. Shinich Ike for their research cooperation and communication. Also, I gratefully acknowledge Mrs. Naoko Matsunaga and Ms. Mayumi Iwata for their behind-the-scenes supports in my research life.

Finally, I would like to thank my parents and my brother for their love, support and encouragement in all of my life.

*July 2014, Yunsheng DENG*

## List of Publications (Oct. 2011 - )

### 1. Journal papers

- [1] **Yunsheng Deng**, Osamu Nakatsuka, Jun Yokoi, Noriyuki Taoka, and Shigeaki Zaima. "Epitaxial formation and electrical properties of Ni germanide/Ge (110) contacts", Thin Solid Films, **557** (2014) 84.
- [2] **Yunsheng Deng**, Osamu Nakatsuka, Noriyuki Taoka and Shigeaki Zaima. "Effect of thermal cleaning on formation of epitaxial Ni germanide layer on Ge (110) substrate", Japanese Journal of Applied Physics, **53** (2014) 05GA06.
- [3] **Yunsheng Deng**, Osamu Nakatsuka, Akihiro Suzuki, Mitsuo Sakashita, and Shigeaki Zaima. "Epitaxial Formation of Ni Germanide on Ge(001) Substrate by Reactive Deposition", Solid-State Electronics. [*Submitted*]

### 2. Related paper

- [1] Osamu Nakatsuka, Tsuyoshi Nishimura, Akihiro Suzuki, Kimihiko Kato, **Deng Yunsheng**, Masashi Kurosawa, Wakana Takeuchi, Mitsuo Sakashita, Noriyuki Taoka, and Shigeaki Zaim. "Formation and Electrical Properties of Metal/Ge<sub>1-x</sub>Sn<sub>x</sub> Contacts", The 14th International Workshop on Junction Technology (IWJT2014), Shanghai, China, May 18-20, 2014.

### 3. Other paper and patent

- [4] **Y.S. Deng**, X.S. Fang, F. Ye, Y. Qiao, J.P. Lin, and G.L. Chen. "Magnetic and mechanical properties of directionally solidified Fe-6.5 wt.% Si alloy", Materials Science Forum. **687** (2011) 122.
- [5] Chinese Patent: ZL 201010588872.6. 林均品, 房现石, **邓云生**, 梁永锋, 叶丰, 陈国良.

### 4. International conferences

- [1] **Yunsheng Deng**, Jun Yokoi, Osamu Nakatsuka, and Shigeaki Zaima. "Formation and Stress Characterization of NiGe/Ge(110) and Ge(001) Contacts", Advanced Metallization Conference 2012 22rd Asian Session (ADMETA Plus 2012), Tokyo, Japan, Oct. 2012.
- [2] **Yunsheng Deng**, Osamu Nakatsuka, Jun Yokoi, Noriyuki Taoka, and Shigeaki Zaima. "Epitaxial formation and electrical properties of Ni germanide/Ge(110) contacts", The 8th International Conference on Silicon Epitaxy and Heterostructures (ICSI-8), Fukuoka, Japan, June 2-6, 2013.
- [3] **Yunsheng Deng**, Osamu Nakatsuka, Noriyuki Taoka, and Shigeaki Zaima. "Thermal Stability of Epitaxial NiGe Layers Formed on Ge(110) Substrate", Advanced Metallization Conference 2012 23rd Asian Session (ADMETA Plus 2013), Tokyo, Japan, Oct. 2013.
- [4] **Yunsheng Deng**, Osamu Nakatsuka, Noriyuki Taoka, and Shigeaki Zaima. "Formation and Electrical Property of Epitaxial NiGe/Ge(110) Schottky Contacts", 7th International WorkShop on New Group IV Semiconductor

Nanoelectronics and JSPS Core-to-Core Program Joint Seminar "Atomically Controlled Processing for Ultralarge Scale Integration", Sendai, Japan, Jan. 2014.

- [5] **Yunsheng Deng**, Osamu Nakatsuka, Noriyuki Taoka, and Shigeaki Zaima. "Impact of Crystalline Structure on Electrical Property of NiGe/Ge Contact", 7th International Silicon-Germanium Technology and Device Meeting (2014 ISTDM), Singapore, June, 2014.

## 5. Domestic conferences

- [1] **Yusheng Deng**, Jun Yokoi, Osamu Nakatsuka, Noriyuki Taoka, and Shigeaki Zaima. "Epitaxial formation and electrical property of Ni Germanide/Ge(110) contact", 第 13 回日本表面科学会中部支部研究会, 名古屋, 2013 年 12 月.
- [2] **Yunsheng Deng**, Osamu Nakatsuka, Noriyuki Taoka, and Shigeaki Zaima. "NiGe/Ge コンタクトの結晶構造および界面電気伝導特性の制御", グリーン・ナノエレクトロニクスのコア技術開発 最終成果報告会, 東京, 2013 年 12 月.
- [3] **鄧云生**, 中塚 理, 財満 鎮明. "Epitaxial formation and electrical property of Ni Germanide/Ge contact", 第 75 回応用物理学会学術講演回, 北海道, 2014 年 9 月. [Submitted]

## 6. Other Conference (co-author)

- [1] Shunsuke Asaba, Jun Yokoi, Hiroki Matsushita, **Deng Yunsheng**, Noriyuki Taoka, Osamu Nakatsuka, and Shigeaki Zaima. "Electrical Properties of Epitaxially Grown  $p^+$ -Ge<sub>1-x</sub>Sn<sub>x</sub>/n-Ge Diodes", IUMRS-International Conference on Electronic Materials (IUMRS-ICEM 2012), Yokohama, Japan, Sep. 2012.
- [2] Osamu Nakatsuka, Jun Yokoi, **Yunsheng Deng**, Noriyuki Taoka, and Shigeaki Zaima. "Crystalline and electrical properties of Ni Germanide/Ge(110) contacts", 6th International WorkShop on New Group IV Semiconductor Nanoelectronics, Sendai, Japan, 2013.
- [3] Osamu Nakatsuka, Tsuyoshi Nishimura, Akihiro Suzuki, Kimihiko Kato, **Deng Yunsheng**, Masashi Kurosawa, Wakana Takeuchi, Mitsuo Sakashita, Noriyuki Taoka, and Shigeaki Zaim. "Formation and Electrical Properties of Metal/Ge<sub>1-x</sub>Sn<sub>x</sub> Contacts", The 14th International Workshop on Junction Technology (IWJT2014), Shanghai, China, May 18-20, 2014.
- [4] 鈴木陽洋, **鄧云生**, 黒澤昌志, 坂下満男, 中塚理, 財満鎮明. "Sn/Ge コンタクトにおけるショットキー障壁高さの Ge 面方位依存性", 第 75 回応用物理学会学術講演回, 北海道, 2014 年 9 月. [Submitted]

## 7. Award

- [1] **Yunsheng Deng**, 研究会講演奨励賞, Epitaxial formation and electrical property of Ni Germanide/Ge(110) contact, 第 13 回日本表面科学会中部支部研究会, 名古屋, 2013 年 12 月.